

UCSF

UC San Francisco Electronic Theses and Dissertations

Title

New Technology Developments for Metabolic Imaging of the Human Abdomen using Hyperpolarized [1-13C]pyruvate

Permalink

<https://escholarship.org/uc/item/9kh5t4gv>

Author

Lee, Philip Meng-en

Publication Date

2022

Peer reviewed|Thesis/dissertation

New Technology Developments for Metabolic Imaging of the Human Abdomen using Hyperpolarized [1-13C]pyruvate

by
Philip Lee

DISSERTATION

Submitted in partial satisfaction of the requirements for degree of
DOCTOR OF PHILOSOPHY

in

Bioengineering

in the

GRADUATE DIVISION

of the

UNIVERSITY OF CALIFORNIA, SAN FRANCISCO
AND
UNIVERSITY OF CALIFORNIA, BERKELEY

Approved:

DocuSigned by:



DA5485F9C42341E...

Daniel Vigneron

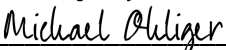
Chair

DocuSigned by:



DocuSigned by:

Peder Larson



EB514B0EC25145F...

Michael Ohliger

Committee Members

Copyright 2022

by

Philip Lee

Dedicated to my grandparents—
Ye-ye, Nai-nai, Po-po, and A-gong

Acknowledgements

Many people have been instrumental factors to my time in this program. An adequate acknowledgement of every person and their contribution and influence upon me would fill far too many pages. I hope that if you are reading this, you feel included in the vast yet incredibly warm community of biomedical imaging. This field is one I entered into without any prior background and I was so genuinely surprised by its hospitality to newcomers.

The first person to demonstrate this to me was my advisor, Professor Dan Vigneron. Due to independent factors, none of my three rotations had openings for me. Desperate for a lab to call home, I asked Dan, my then-graduate advisor, if he had open spots. Even though he knew I had zero background in biomedical imaging—which meant that I would have to learn everything from scratch—Dan, you welcomed me with open arms and brought me into the warmest, most collaborative, and the most supportive research group I have ever been a part of. So, thank you. I would not be here today if it was not for your belief in me and your unshaking resolve to train young graduate students and to bring them to their full potential.

This research group includes so many, past and present, that I would like to thank here. Again, I have many words for each one. That is my excuse—not due to a laziness to write, but because writing all of my words would truly take far too much space. You all mean so much to me. So while the following list may read casually, it is written with great feeling and gratitude for every soul that has enabled me to succeed. My first mentor, Dr. Zihan Zhu. My second mentor, Dr. Hsin-Yu Chen. My

resource for all things science, Dr. Jeremy Gordon, and who has never failed to enlighten and inspire. My close collaborator and researcher, day and night, weekday and weekend, Dr. Michael Ohliger. My teachers, instructors, and mentors Drs. Peder Larson, John Kurhanewicz, and Renuka Sriram. My cubicle labmate and comrade in science, Mrs. Jasmine Hu. My other cubicle labmate, who was like an older brother to me when I first joined, Dr. Brian Chung. My more recent labmates, Mr. Tanner Nickles and Mr. Danny Gebrezgiabhier; keep going, keep discovering, and keep building! An inspiration to me, Dr. Yaewon Kim; the fruitfulness of your work is astounding. My brilliant and inspiring peer, Dr. Jessica Scholey; grinding away on Peder's homework assignments while everyone else was having fun at Asilomar will always be a fond memory. My additional mentors who have taught me and supported me every time I reached out, Drs. Nick Dwork (thank you so much, Nick), Shuyu Tang, Hecong Qin, Xiaoxi Liu, Dave Korenchan, Natalie Korn, Cornelius von Morze, Robert Bok, Zhen Jane Wang, Rahul Aggarwal, Steve Conolly, Moriel Vandsburger, Michel Maharbiz, Dave Schaffer, and Niren Murthy. The incomparable engineers, Mr. Lucas Carvajal (thank you for committing hours to thoroughly address every question I had) and Mr. Mark van Crieking. The absolutely admirable pharmacy team, led by Drs. Jim Slater and Andrew Riselli (I'm so glad you chose to come to UCSF) with Ms. Evelyn Escobar and Ms. Jennifer Chow; what unparalleled skill it takes to do what you all do! The MRI technologists who demonstrated such expertise in their craft, Mrs. Mary Frost (thank you for all those initial rounds of training), Ms. Hope Williams, and Ms. Heather Daniel. The nurse whom I can always rely on and who demonstrated such a caring humanity to her patients, Ms. Kimberly Okamoto. The fantastic administrative staff, Ms. Ana Maria Deluca, Mrs. Jenny Che, Ms. Kim Semien, Dr. Jenna Bernard, and Ms. Cresini Tabaranza-David who managed everything so well, that it is only when they are on their well-deserved vacations that you realize how much they are the foundation of the lab. The clinical research coordinators that always had what I needed, Mr. Christopher Sotto, Mr. Justin Delos Santos, Ms. Priscilla Chan, Ms. Kiersten Cheung, Mrs. Francesca

Leung, and Ms. Louise Magat. The program administrators, Ms. SarahJane Taylor, Ms. Kristin Olson, Ms. Rocío Sanchez, and Mrs. Victoria Starrett. I hope it is sufficiently obvious that room only allows for such distilled acknowledgements. I wish I could spend an afternoon with you all individually.

Now I move on to those outside of the laboratory who have been core to my life. Of course, my very first acknowledgement is to my family, my baba Edward, my mama Shew-reng (Christiana), and my older brother whom I have always affectionately called “Jay-Ga” since childhood (his actual name is Jacob). My grandparents, Ye-ye, Nai-nai, Po-po, and A-gong, to whom this dissertation is dedicated. No others have sacrificed so much as much as you all have.

Thank you to my undergraduate mentors, Dr. Paul Yager and all those in his research lab, especially Drs. Koji Abe and Shichu Huang, and my close friends, teachers, and mentors from Transition School—soon-to-be Drs. Joanne Kim, Abby Bratt, and Carmen Ursachi, Drs. Curtis Hisayasu, Tom Cramer, Therese Mar, Oscar Vilches, Jeramy Gee, Maren Halvorsen, Nancy Hertzog, and the late Dr. Ernest Henley—and from the Department of Bioengineering at the University of Washington and beyond—Drs. Dianne Hendricks, Alyssa Taylor, Alan Leong, King-Fai Li, and Ms. Katy DeRosier among countless others. Thank you also to those who have taught me at UC Berkeley and UC San Francisco.

Finally, I thank my brothers and sisters at the church in Berkeley. Each one knows who he or she is. It would take an eternity to enumerate your impact upon me during these five years, and I am glad that we will have eternity to do so.

Philip Lee

May 2022

Abstract

New Technology Developments for Metabolic Imaging of the Human Abdomen using
Hyperpolarized [1-¹³C]pyruvate

Philip Lee

Hyperpolarized (HP) ¹³C magnetic resonance imaging (MRI) is a novel imaging modality that is powerful in its ability to elucidate *in vivo* human metabolism in a safe, non-invasive manner without ionizing radiation. This can be carried out by using molecular probes such as [1-¹³C]pyruvate, a molecule of much clinical interest because of its crucial metabolic position. Pyruvate is used in both oxidative phosphorylation and aerobic glycolysis, with the latter pathway being upregulated in cancers due to metabolic reprogramming. Thus, investigating how pyruvate is metabolized in a given tissue can provide researchers and clinicians with a window into the tissue's metabolic characteristics, such as whether or not it is metabolically behaving in a cancerous manner after chemotherapy. High signal-to-noise ratios (SNR) is achieved through dissolution dynamic nuclear polarization. Upon injection of a solution of hyperpolarized [1-¹³C]pyruvate, one can acquire dynamic metabolic images and spectroscopic data in the human body with remarkable resolution.

HP ¹³C MRI has found much success for research imaging studies of the brain, prostate, and other organs. This dissertation focuses on new technology developments that I developed to enable the translation of this technology into human abdominal organs, both in cancerous and healthy states. These developments aim to address several challenges including main magnetic field (B_0) and transmit magnetic field (B_1^+) inhomogeneities, low SNR, broad spatial coverage, and fast acquisition

techniques. A clinical feasibility study using HP ^{13}C MRI for metastatic prostate cancer tumors demonstrates the promise and feasibility of this imaging modality in quantitating *in vivo* metabolism. Additionally, a whole-abdomen metabolic imaging approach enabled the characterization of healthy metabolism in the human liver, kidneys, pancreas, and spleen, laying the foundation for designing future investigations of cancer and metabolic diseases in the abdomen.

Table of Contents

Chapter 1: Introduction	1
Chapter 2: Scientific & Technical Background	3
2.1 Fundamentals of Magnetic Resonance Imaging	3
2.1.1 Spin, Magnetization, & Polarization	3
2.1.2 Radiofrequency Excitation & Signal Detection	5
2.1.3 Spatial Encoding, Slice Selection, & k -space	7
2.1.4 Relaxation	9
2.1.5 Bloch Equation	12
2.1.6 Chemical Shift	13
2.1.7 Creation of Images from Magnetic Resonance Acquisitions	15
2.2 Introduction to Hyperpolarized ^{13}C Magnetic Resonance Imaging	19
2.2.1 Dissolution Dynamic Nuclear Polarization	20
2.2.2 Challenges in Hyperpolarized ^{13}C MRI Acquisition	23
2.2.3 Hyperpolarized ^{13}C Magnetic Resonance Imaging with $[1-^{13}\text{C}]\text{pyruvate}$	24

2.3	MRI—A Testament to the Ingenuity of the Human Mind	25
2.4	References	27

Chapter 3: Hyperpolarized ^{13}C -pyruvate MRI Detects Real-Time Metabolic Flux in

Prostate Cancer Metastases to Bone & Liver: A Clinical Feasibility Study 30

3.1	Abstract	31
3.1.1	Background	31
3.1.2	Methods	31
3.1.3	Results	31
3.1.4	Conclusions	32
3.2	Introduction	32
3.3	Methods	34
3.3.1	Patient Selection	34
3.3.2	HP ^{13}C Patient MRI Studies	34
3.3.3	Data Acquisition & Analysis	35
3.3.4	Metastatic Tumor Biopsy Acquisition & Analysis	35
3.4	Results	36
3.4.1	Patient Characteristics	36
3.4.2	HP ^{13}C -pyruvate MRI Detects High k_{PL} in Bone & Liver Metastases	36
3.4.3	HP ^{13}C MRI Detected a Metabolic Rate Decrease in a Metastasis Following Chemotherapy	39
3.5	Discussion	39
3.6	Conclusions	43
3.7	Acknowledgements	44

3.8	Supporting Information	44
3.9	References	47

Chapter 4: Specialized Computational Methods for Denoising, B_1 Correction, &

Kinetic Modeling in Hyperpolarized ^{13}C MR EPSI Studies of Liver Tumors 53

4.1	Abstract	54
4.1.1	Purpose	54
4.1.2	Methods	54
4.1.3	Results	54
4.1.4	Conclusions	54
4.2	Introduction	55
4.3	Methods	56
4.3.1	Patients	56
4.3.2	HP ^{13}C Patient MRI Scans	56
4.3.3	Data Acquisition	59
4.3.4	Denoising	59
4.3.5	B_1^+ Transmit Field Inhomogeneity Correction	60
4.4	Results	61
4.4.1	Patient Scans	61
4.4.2	Denoising & B_1^+ Transmit Field Inhomogeneity Correction	61
4.5	Discussion	66
4.6	Conclusions	69
4.7	Acknowledgements	69
4.8	Supporting Information	70

4.9	References	71
-----	----------------------	----

Chapter 5: Hyperpolarized Carbon-13 MRI in Liver Diseases: Recent Advances &

Future Opportunities	77
---------------------------------------	-----------

5.1	Abstract	78
-----	--------------------	----

5.2	Introduction	78
-----	------------------------	----

5.3	Hepatic Metabolism & Pyruvate	80
-----	-----------------------------------------	----

5.4	Workflow of Hyperpolarized Carbon-13 MRI	82
-----	----------------------------------------------------	----

5.5	Recent Advances	83
-----	---------------------------	----

5.5.1	Diffuse Liver Diseases	85
-------	----------------------------------	----

5.5.2	Liver Malignancy	89
-------	----------------------------	----

5.6	Future Opportunities	94
-----	--------------------------------	----

5.7	Conclusions	97
-----	-----------------------	----

5.8	References	98
-----	----------------------	----

Chapter 6: Whole-Abdomen Metabolic Imaging of Healthy Volunteers Using

Hyperpolarized [1-¹³C]pyruvate MRI	108
----------------------------------------------------------------	------------

6.1	Abstract	109
-----	--------------------	-----

6.1.1	Background	109
-------	----------------------	-----

6.1.2	Purpose	109
-------	-------------------	-----

6.1.3	Study Type	109
-------	----------------------	-----

6.1.4	Subjects	109
-------	--------------------	-----

6.1.5	Field Strength/Sequence	109
-------	-----------------------------------	-----

6.1.6	Assessment	110
-------	----------------------	-----

6.1.7	Statistical Tests110
6.1.8	Results110
6.1.9	Data Conclusion110
6.2	Introduction111
6.3	Methods113
6.3.1	Radiofrequency Coil Array113
6.3.2	B_1^+ Mapping113
6.3.3	Study Eligibility115
6.3.4	^1H MRI Scans115
6.3.5	Hyperpolarized ^{13}C MRI Scans117
6.3.6	Data Processing & Kinetic Modeling121
6.3.7	Statistical Analysis123
6.4	Results124
6.4.1	B_1^+ Characterization of QTAR124
6.4.2	Healthy Volunteer Scans124
6.4.3	^1H vs. ^{13}C ΔB_0 Maps using Pyruvate's Frequency Offsets125
6.4.4	B_0 Inhomogeneity Corrections125
6.4.5	Patch-Based Denoising127
6.4.6	Metabolite Dynamics in Each Organ129
6.4.7	Summed Metabolite Signals & Metabolite Kinetics in Each Organ129
6.5	Discussion133
6.5.1	Limitations138
6.6	Conclusions139
6.7	Acknowledgements139

6.8 Supporting Information140

6.9 References142

List of Figures

2.1	The effect of an external magnetic field on a population of nuclear spins.	5
2.2	Radiofrequency (RF) excitation of the net magnetization in both a laboratory frame of reference and a rotating frame of reference.	7
2.3	Longitudinal and transverse components of magnetization and their corresponding relaxation curves.	9
2.4	The chemical shifts resulting from the presence of common organic moieties.	14
2.5	A carbon-13 (^{13}C) spectrum obtained from endogenous signal in the human leg using a surface coil.	14
2.6	A generic spin-echo pulse sequence diagram with a 90° pulse followed by a 180° pulse.	15
2.7	Excitation waveform and profile of the echo-planar imaging metabolite-specific, spectral-spatial pulse.	16
2.8	An echo-planar imaging (EPI) pulse sequence with a spectral-spatial RF pulse followed by a symmetric readout gradient.	17
2.9	An echo-planar spectroscopic imaging (EPSI) pulse sequence with a spectral-spatial RF pulse followed by a phase-encoding gradient and a symmetric readout gradient.	18

2.10	Comparison of polarization for electrons, ^1H nuclei (protons), and ^{13}C nuclei over a range of temperatures.	20
2.11	T_1 relaxation for a system at thermal equilibrium with a magnetization beginning from zero and reaching M_0 compared to T_1 relaxation for a system in a hyperpolarized state with a magnetization decaying from a magnitude several fold larger than M_0	21
2.12	Comparison of ^{13}C urea spectra from a thermally polarized state versus from a hyperpolarized state.	21
2.13	Summary of necessary components for hyperpolarized (HP) ^{13}C magnetic resonance clinical research.	22
2.14	Metabolic pathways for $[1-^{13}\text{C}]$ pyruvate.	24
3.1	An illustration of lactate dehydrogenase (LDH)-mediated aerobic glycolysis and relevant metabolic pathways.	33
3.2	Regions of high k_{PL} were consistent with computed tomography (CT) and magnetic resonance imaging (MRI) radiographic findings of metastatic disease presence.	37
3.3	Metabolic rate decrease was detected in a metastasis following chemotherapy.	40
S3.1	k_{PL} map and metabolic dynamics for an 83-year-old prostate cancer patient.	44
S3.2	k_{PL} map and metabolic dynamics for a 73-year-old prostate cancer patient.	45
S3.3	k_{PL} map and metabolic dynamics for a 70-year-old prostate cancer patient.	46
S3.4	k_{PL} map for an 83-year-old prostate cancer patient.	46
4.1	Internal circuitry of the figure-8 transmit/receive surface coil, its B_1^+ profile, and photos of coil placement for a patient scan.	58
4.2	The acquired HP ^{13}C EPSI spectra and metabolite dynamics before and after denoising for tumor and normal-appearing voxels.	62

4.3	Metabolite time courses for pyruvate, lactate, and alanine from a representative patient scan.	63
4.4	k_{PL} maps before and after transmit field (B_1^+) correction from a representative patient scan.	65
S4.1	Monte Carlo simulations of the two-site inputless model demonstrated an inverse relationship between the relative B_1^+ error and the fractional k_{PL} error.	70
5.1	The histological changes, representative conventional images and typical metabolic pathways of different liver diseases.	81
5.2	The workflow of hyperpolarized ^{13}C MRI in liver diseases. QC, quality control.	83
6.1	Internal circuitry of the volumetric transmitter and 4-channel array ^{13}C coil, photos of the coil setup, and its B_1^+ profile.	114
6.2	Correlation plot of the 1H and ^{13}C ΔB_0 maps.	120
6.3	Improvements in frequency variation within abdominal organs with and without local shimming.	126
6.4	Improvements in signal-to-noise ratio (SNR) after patch-based higher-order singular value decomposition denoising.	128
6.5	Metabolite dynamics for pyruvate, lactate, and alanine from selected voxels of abdominal organs.	130
6.6	Pyruvate, lactate, and alanine maps summed through time from a representative subject.	131
6.7	k_{PL} and k_{PA} maps from a representative subject.	132
6.8	k_{PL} and k_{PA} values for each organ averaged across all seven subjects with EPI scans.	133
S6.1	The percent of voxels which passed the SNR thresholds for each metabolite before and after denoising excluding data points from one subject.	141

List of Tables

2.1	The natural abundance, gyromagnetic ratios, and Larmor frequencies at 3 T for the nuclei of several common nuclear magnetic resonance (NMR)-visible isotopes.	6
3.1	A summary of clinically relevant information from each patient.	36
3.2	Findings from HP ^{13}C MRI including k_{PL} and RNA expression of key genes.	37
4.1	Selected voxels from seven patient scans showing the optimized tensor ranks, improvements in SNR after denoising, the flip correction scaling factor, the k_{PL} values before and after B_1^+ correction, and the percent difference.	57
5.1	Summary of HP ^{13}C MRI in diffuse liver diseases.	84
5.2	Summary of HP ^{13}C MRI in liver malignancies.	84
6.1	Scan parameters for all proton and ^{13}C human scans.	116
6.2	Summary of averaged k_{PL} and k_{PA} values across successful EPI scans.	134
S6.1	Summary of all hyperpolarized ^{13}C acquisitions in healthy volunteers.	140

Chapter 1

Introduction

Pyruvate, a key molecule in cellular bioenergetics, can be metabolized by cells through two major pathways. Typically, healthy cells use pyruvate to produce acetyl-CoA, ultimately for oxidative phosphorylation and ATP production through the citric acid cycle. However, in cancerous cells, metabolic reprogramming known as the Warburg effect causes the upregulated conversion of pyruvate to lactate. Thus, there is the need for safe, non-invasive methods that can quantify the rate at which a given tissue (perhaps a suspicious lesion) metabolizes pyruvate through this second pathway. Such a method would allow researchers and clinicians to non-invasively assess response to drug therapies (whether a tissue still exhibits high levels of lactate production characteristic of cancer metabolism after treatment).

This unmet clinical need may be addressed by hyperpolarized (HP) [1-¹³C]pyruvate magnetic resonance imaging (MRI), a molecular imaging modality that enables quantitative imaging and characterization of *in vivo* metabolism. Applications are not limited to cancer but can be extended to other metabolic diseases, such as non-alcoholic fatty liver disease (NAFLD).

This dissertation will begin with introducing principles of magnetic resonance imaging in chapter 2, and based upon these principles, continue by presenting a novel imaging modality,

hyperpolarized ^{13}C MRI, and how it enables dynamic, *in vivo* imaging of ^{13}C nuclei for quantification of human metabolism.

Chapter 3 describes an application of this technology to metastatic prostate cancer in bone and viscera. Upregulated pyruvate to lactate conversion (k_{PL}) was observed in aggressive metastases. Decrease in k_{PL} was also observed in one patient who received chemotherapy, agreeing with conventional clinical biomarkers. The results demonstrate the safety and feasibility of HP ^{13}C MRI and its promise for use in monitoring response to therapy in metastatic prostate cancer.

Chapter 4 presents a novel post-processing pipeline for HP ^{13}C spectroscopic data in which I integrated a denoising algorithm with a B_1^+ correction algorithm. The processed data had signal-to-noise ratio (SNR) increases of at least 20-fold for pyruvate, lactate, and alanine signals as well as improved dynamics and k_{PL} estimations, which agreed with Monte Carlo simulations.

Chapter 5 details recent advancements of HP ^{13}C MRI in diffuse liver diseases and liver malignancies, both in pre-clinical and clinical studies. As HP ^{13}C MRI has seen success in other organs, such as the prostate and brain, this technology is translatable to other organs and metabolic diseases besides cancer.

This sets the stage for chapter 6. In order to study the metabolism of these abdominal organs in humans, a robust imaging protocol must first be established, one that overcomes major challenges including broad spatial coverage, breathing motion, magnetic field B_0 inhomogeneities, and low SNR in the liver. This chapter presents an imaging protocol addressing these challenges, which also enabled the metabolic characterization of the healthy human liver, kidneys, pancreas, and spleen. This normative data will be valuable for designing future investigations of cancer and metabolic liver diseases, such as NAFLD.

Chapter 2

Scientific & Technical Background

This chapter presents the relevant scientific background of magnetic resonance imaging (MRI) and hyperpolarized (HP) carbon-13 (^{13}C) MRI.

2.1 Fundamentals of Magnetic Resonance Imaging

Magnetic resonance imaging (MRI) is a medical imaging modality that acquires images of anatomy and physiological processes. It uses a strong magnetic field, magnetic field gradients, and radio waves. However, it does not use ionizing radiation, such as X-rays, thereby making it a generally safe imaging technique. This first section will introduce the fundamentals of MRI, describing nuclear spins, their behavior in magnetic fields, and how these physical phenomena enable image acquisition.

2.1.1 Spin, Magnetization, & Polarization

Nuclear spin is an intrinsic form of angular momentum of subatomic particles (electrons, protons, and neutrons). Consequently, the nucleus of an atom exhibits an overall spin depending on the number of protons and neutrons of which it is comprised. Spins can be paired against each other; therefore, if the number of neutrons and protons are both even, the nucleus overall has no spin. Such is the case

with ^{12}C with 6 neutrons and 6 protons. If the number of neutrons plus the number of protons is odd, then the nucleus has a half-integer spin (e.g. $1/2$, $3/2$, $5/2$). The most abundant atom with a half-integer spin is ^1H , with 1 proton and 0 neutrons, resulting in a spin of $1/2$. If the number of neutrons and the number of protons are both odd, then the nucleus has an integer spin, which is the case for ^2H (deuterium) among others.

A non-zero nuclear spin is the basis to nuclear magnetic resonance (NMR), a phenomenon in which the nuclear spins of a given molecule (whether alone, in solution, or even in a complex cellular environment), predictably give rise to a signal with a unique frequency, a molecular signature of sorts, that can be observed and quantified however the scientist sees fit.

For a single nucleus, the spin vector \mathbf{S} , with directionality aligned along its axis of rotation, is related to its magnetic dipole moment $\boldsymbol{\mu}$ by way of the nuclei's gyromagnetic ratio (γ), a constant unique to each nucleus:¹

$$\boldsymbol{\mu} = \gamma\mathbf{S} \quad (2.1)$$

In the presence of an external magnetic field, these magnetic dipoles orient themselves parallel (n^+) or anti-parallel (n^-) to the field, a process called polarization. The n^+ population is of lower energy, resulting in a slight population difference (Figure 2.1) and the ratio of the two populations following a Boltzmann equilibrium:²

$$\frac{n^+}{n^-} = e^{\frac{-\gamma\hbar B_0}{k_B T}} \quad (2.2)$$

where \hbar is the reduced Planck's constant (in J·s), B_0 is the magnetic field strength (in T), k_B is the Boltzmann constant (in J·K⁻¹), and T is the temperature (in K). At body temperature and a field strength of 3.0 T, the ratio of spins for ^1H nuclei is approximately 0.999997, which equates to a difference of 3 spins per 1 million.

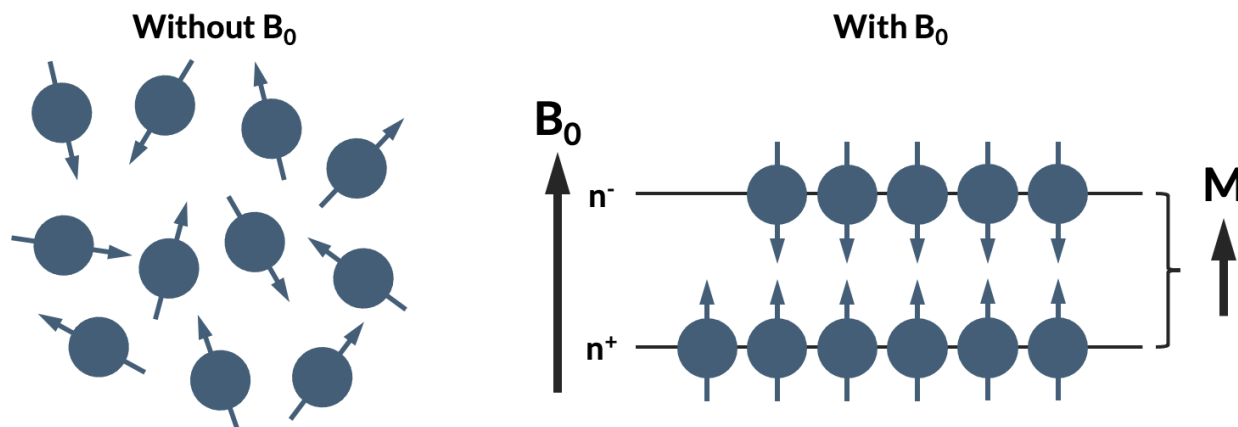


Figure 2.1. The effect of an external magnetic field (\mathbf{B}_0) on a population of nuclear spins (with arrows indicating magnetic dipole). Without an external magnetic field, dipoles are randomly oriented resulting in a net zero magnetization (\mathbf{M}). With an external magnetic field, dipoles are aligned parallel (n^+) or anti-parallel (n^-) to the field and the net difference between the two populations gives rise to a non-zero \mathbf{M} .

At thermal equilibrium, the difference in population, although small, gives rise to a net magnetization vector \mathbf{M} , which is observed macroscopically in NMR. Normalized to the total number of spins present gives the overall polarization of the system at thermal equilibrium, P_{th} :³

$$P_{th} = \frac{n^+ - n^-}{n^+ + n^-} = \tanh\left(\frac{\gamma\hbar B_0}{2k_B T}\right) \quad (2.3)$$

It is apparent from Eqn. 2.3 that P_{th} is a function of γ , B_0 , and T . The observable magnetization signal for a given nuclei and its γ is maximized with stronger magnetic fields and lower temperatures (though modulating this latter parameter is not always feasible when working with living samples).

2.1.2 Radiofrequency Excitation & Signal Detection

When perturbed by another external magnetic field, \mathbf{B}_1 , the net magnetization \mathbf{M} precesses about the \mathbf{B}_0 vector described by the following equation:²

$$\frac{d\mathbf{M}}{dt} = \mathbf{M} \times \gamma\mathbf{B}_0 \quad (2.4)$$

Furthermore, the precession occurs at its Larmor frequency, ω , unique to the nucleus and proportional to the strength of the external magnetic field, \mathbf{B}_0 , defined as:

$$\omega = \gamma B_0 \quad (2.5)$$

The gyromagnetic ratio γ and Larmor frequencies ω at 3 Tesla (T) for the nuclei of several common NMR-visible isotopes are given below in Table 2.1.²

Table 2.1. The natural abundance, gyromagnetic ratios (γ), and Larmor frequencies (ω) at 3 T for the nuclei of several common NMR-visible isotopes.

Isotope	Natural abundance	γ (MHz/T)	ω (MHz at B_0 of 3 T)
^1H	99.99%	42.58	127.7
^{13}C	1.1%	10.71	32.13
^{19}F	$\approx 100\%$	40.05	120.2
^{23}Na	$\approx 100\%$	11.26	33.78
^{31}P	$\approx 100\%$	17.24	51.72

The \mathbf{B}_1 field is generated by a radiofrequency (RF) coil and must be applied at the Larmor frequency in order to perturb the net magnetization from its equilibrium state. Viewing this system in the laboratory frame of reference (Figure 2.2a), the \mathbf{B}_1 field rotates at the Larmor frequency and induces a torque upon the net magnetization \mathbf{M} , which is rotating around the \mathbf{B}_0 vector, gradually bringing it towards the transverse plane. In a rotating frame of reference at the Larmor frequency, the \mathbf{B}_1 vector is static and the net magnetization \mathbf{M} rotates around \mathbf{B}_1 (Figure 2.2b).

The extent to which \mathbf{M} rotates around \mathbf{B}_1 , that is, the flip angle θ , depends on the duration of the RF pulse; it is given by the integral:^{2,3}

$$\theta = \int_0^T \gamma B_1(t) dt \quad (2.6)$$

where T is the duration of the RF pulse. The transverse component (equal to $\mathbf{M} \sin \theta$) of the net magnetization vector \mathbf{M} induces an electromotive force in an RF receiver coil, according to Faraday's law of induction, generating a signal called a free induction decay (FID) used to reconstruct the NMR signal (the signal then decays by relaxation processes described later). Given that it follows a sine

function, the transverse component reaches its maximum with a flip angle of 90° and positive flip angles less than 180° would result in a smaller transverse component. The magnetization is entirely inverted with a flip angle of 180° . The transverse component is then simply 0 and there is no detectable signal.

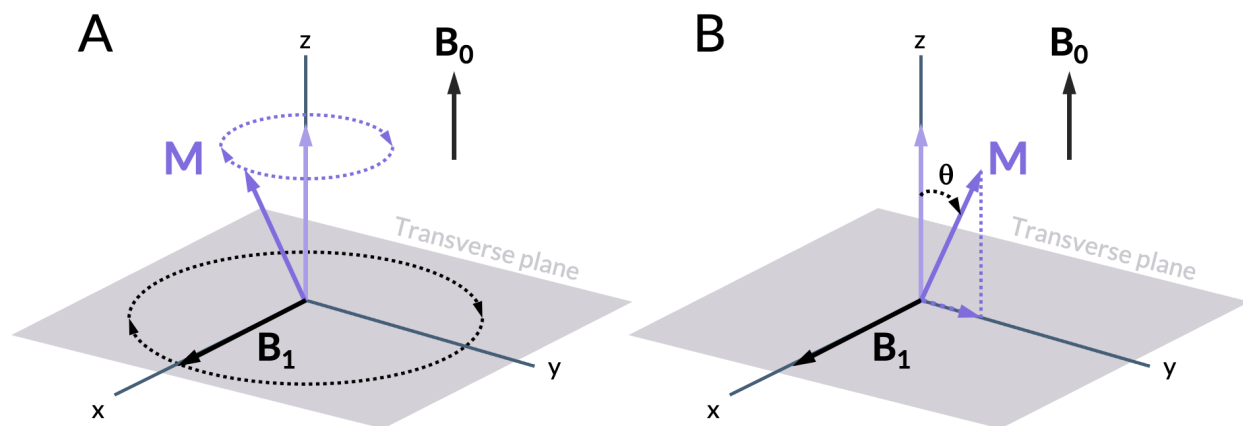


Figure 2.2. (a) Radiofrequency (RF) excitation of the net magnetization M in a laboratory frame of reference. M (previously at equilibrium, indicated by the light purple vector) now rotates around the external magnetic field B_0 and gradually tends toward the transverse plane due to the torque exerted upon it by the external magnetic field B_1 , which rotates at the same frequency as M . (b) The same scene but viewed in a rotating frame of reference at the Larmor frequency. B_1 is static and M rotates around B_1 by an angle θ , resulting in a transverse magnetization component along y .

2.1.3 Spatial Encoding, Slice Selection, & k -space

Adding linear magnetic field gradients in the x , y , and z directions imposes a linear variation of resonance frequencies in space. For instance, upon applying a gradient along z with a magnetic field strength G_z , the resulting frequencies would be a function of their position along z :²

$$f(z) = \frac{\gamma}{2\pi} (B_0 + G_z z) \quad (2.7)$$

Hence, the signals are spatially encoded; the offset from their original Larmor frequency provides their spatial location. And each slice of interest now has a specific center frequency. However, to then acquire an image at one of these slices, that is, to uniquely excite only one slice among others, the RF pulse must be tailored to excite a narrow band of frequencies, centered around the slice's center

frequency. This is accomplished by using a sinc-shaped $\mathbf{B}_1(t)$ pulse, which, being a square pulse in the frequency domain, cleanly delineates the frequencies that receive excitation (of course in practice, no square pulse is ever perfect). What results is the excitation of a single slice, and this procedure can be repeated to image the entire volume. Naturally, it follows that adjusting the bandwidth of the pulse and the amplitude of the slice-selective gradient modifies slice thickness and its profile.

To speak of this process from a signal processing perspective, the signal acquisition takes place not in the familiar image space but in k -space, $\mathbf{k}(t)$, the spatial frequency domain. With applied gradients $\mathbf{G}(t)$ and a single slice with two spatial dimensions x and y , the acquired signal is given by the following equation:²

$$s(t) = \iint m(x, y) e^{-i2\pi[\mathbf{k}_x(t)x + \mathbf{k}_y(t)y]} dx dy \quad (2.8)$$

$$\mathbf{k}(t) = \frac{\gamma}{2\pi} \int_0^t \mathbf{G}(\tau) d\tau \quad (2.9)$$

It can readily be recognized that the signal $s(t)$ is the 2D Fourier transform of the transverse magnetization $m(x, y)$ at spatial frequency $\mathbf{k}(t)$. Thus, the data acquired after RF excitation are the spatial frequencies in k -space, which are 2D Fourier transformed into an appreciable image.

Adequate coverage and sampling in k -space determines the overall quality and utility of MR images. Spacing of points in k -space (Δk) is inversely related to the field of view (FOV) in image space and correspondingly k -space coverage ($n\Delta k$ where n is the number of samples in one dimension) is inversely related to the spatial resolution in image space (δ):²

$$FOV = \frac{1}{\Delta k} \quad (2.10)$$

$$\delta = \frac{1}{n\Delta k} \quad (2.11)$$

Trajectories to traverse k -space for sampling magnetization can take different forms, such as cartesian, echo-planar imaging (EPI), and spiral trajectories to name a few.⁴ Each trajectory has its advantages and disadvantages in acquisition speed, signal-to-noise ratio (SNR) and robustness to motion sensitivity and off-resonance artifacts and are thus selected intentionally for different purposes.

In sum, acquired FIDs are stored in the form of decomposed spatial frequencies which are Fourier transformed into clear images of the object.

2.1.4 Relaxation

Neglected in discussion thus far are the effects of relaxation, which causes signal decay. Yet it is precisely because of its existence and how it is modulated by the local molecular environment that there can be tissue contrast in clinical applications, rendering fat looking very different from blood vessels and blood vessels from bone. When equilibrium polarization is disturbed, the magnetization returns to its equilibrium state through a process called relaxation consisting of longitudinal and transverse components (Figure 2.3).

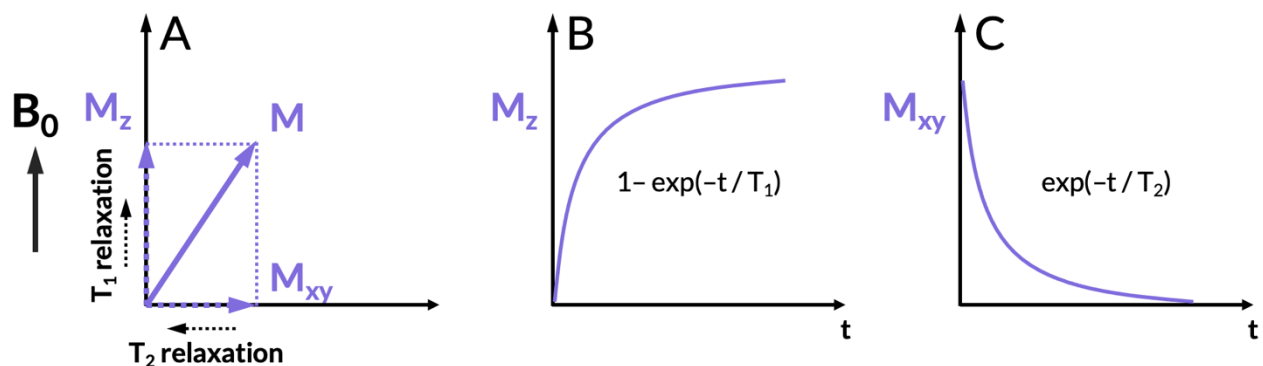


Figure 2.3. (a) Longitudinal relaxation of the M_z component of magnetization, which is governed by the T_1 time constant and transverse relaxation of the M_{xy} component of magnetization, which is governed by the T_2 time constant. (b) Longitudinal relaxation restores the magnetization to its thermal equilibrium value. (c) Transverse relaxation occurs as the magnetization in the transverse plane exponentially decays due to dephasing. In this figure, simplified forms of the exponential curves are given.

Longitudinal relaxation, also called spin-lattice or T_1 relaxation, results in the restoration of the magnetization parallel to the external \mathbf{B}_0 field and is characterized, as it is so aptly named, by a time constant T_1 . This process occurs because of an energy flow between spins and their external environment (the “lattice”), ultimately seeking to restore Boltzmann equilibrium. In the presence of constant \mathbf{B}_0 , when spins have just been perturbed by an RF excitation for instance, energy leaves the spin system and is transferred to nearby particles through random tumbling, collisions, and electromagnetic interactions, and spins return to their thermal equilibrium state, parallel and anti-parallel to \mathbf{B}_0 , with more favoring the lower energy parallel orientation. This recovery is modeled as an exponential process and thus, the time constant T_1 is defined as the time required for the longitudinal component of \mathbf{M} to reach $\left(1 - \frac{1}{e}\right)$, approximately 63%, of its maximum value. The longitudinal component of the net magnetization, $M_z(t)$, can thus be calculated as:²

$$M_z(t) = M_0 + (M_z(0) - M_0)e^{\frac{-t}{T_1}} \quad (2.12)$$

where M_0 is the maximum value of \mathbf{M} and $M_z(0)$ is the initial value of $M_z(t)$. This simplifies to:²

$$M_z(t) = M_0 \left(1 - e^{\frac{-t}{T_1}}\right) \quad (2.13)$$

if $M_z(0) = 0$, which is the case after a flip angle θ of 90° .

Transverse relaxation, also called spin-spin or T_2 relaxation, describes the decay of magnetization in the transverse plane after the net magnetization is tipped from equilibrium. Immediately after RF excitation, while there transiently exists a rotated net magnetization vector \mathbf{M} , this vector is merely the asymmetric statistical representation of millions of individual magnetic dipoles, of which only 1 of every million actually contributes to its overall magnitude and direction. Any random process that disrupts the positions of these dipoles that contribute to \mathbf{M} will only disrupt phase coherence, and thus decrease \mathbf{M} . T_2 relaxation can occur when spins exchange energy with its

external environment (factors that induce T_1 relaxation likewise induce T_2 relaxation), resulting in spins that lose phase relations with the other spins. T_2 relaxation can also occur due to local magnetic field disturbances (such as the dipoles of adjacent nuclei) which in turn can add or subtract from the \mathbf{B}_0 experienced by a spin, correspondingly affecting its Larmor frequency ω (see Eqn. 2.5). As this spin continues precessing at a different frequency, a phase difference between it and its neighbors accumulates and the overall transverse magnetization diminishes. T_2 relaxation is more pronounced in solid or bound phases (e.g. in a macromolecule) because spins cannot freely move as in liquid phases, and thus, are subject to dipole-dipole interactions which dephase magnetization. This component of relaxation is also modeled as an exponential process and so, the time constant T_2 is defined as the time required for the transverse component of \mathbf{M} to fall to $\left(\frac{1}{e}\right)$, approximately 37%, of its initial value. The transverse component of the net magnetization, $M_{xy}(t)$, can thus be calculated as:²

$$M_{xy}(t) = M_{xy}(0) \left(e^{-\frac{t}{T_2}} \right) \quad (2.14)$$

where $M_{xy}(0)$ is the initial value of $M_{xy}(t)$ and would only equal M_0 if thermal equilibrium was reached followed by a flip angle θ of 90° .

In practice, additional factors contribute to a more rapid T_2 relaxation, such as non-uniformity in the \mathbf{B}_0 field and susceptibility effects. Thus, T_2^* is defined and is the more readily observable value in practice:⁵

$$\frac{1}{T_2^*} = \frac{1}{T_2} + \frac{1}{T_2'} \approx \frac{1}{T_2} + \gamma \Delta B_0 \quad (2.15)$$

with T_2' encompassing all imperfections in the system that result in deviations in the nominal \mathbf{B}_0 field strength (ΔB_0).

One can observe that as factors that induce T_1 relaxation also induce T_2 relaxation, T_2 is always smaller than T_1 . One can also immediately observe that both components of relaxation are intimately related to the local environment of the molecule harboring the spinning nucleus. Thus, each tissue in the human body has specific T_1 and T_2 values which cause them to appear dark or bright in T_1 - and T_2 -weighted MR images and can be altered due to pathologies. The mathematical relationships between magnetization signal and relaxation are summarized by the Bloch Equation, presented in the following section.

2.1.5 Bloch Equation

Magnetization in an external magnetic field with relaxation considered is given by the Bloch equation:²

$$\frac{d\mathbf{M}}{dt} = \mathbf{M} \times \gamma \mathbf{B} - \frac{M_x \mathbf{i} + M_y \mathbf{j}}{T_2} - \frac{(M_z - M_0) \mathbf{k}}{T_1} \quad (2.16)$$

where $\mathbf{M} = [M_x, M_y, M_z]^T$ is the magnetization vector, t is time, γ is the gyromagnetic ratio of the nucleus, \mathbf{B} is the magnetic field vector, \mathbf{i} , \mathbf{j} , and \mathbf{k} are unit vectors in x , y , and z , respectively, M_0 is the equilibrium magnetization, and T_1 and T_2 are the longitudinal and transverse relaxation time constants described previously. The cross-product relationship describes the precession of \mathbf{M} about \mathbf{B} . The magnetic field \mathbf{B} itself is comprised of three types of magnetic fields: main static fields \mathbf{B}_0 , radiofrequency fields \mathbf{B}_1 transmitted by coils for excitation, and linear gradient fields \mathbf{G} for spatial encoding. The latter two are 1,000 times smaller in amplitude compared to \mathbf{B}_0 ; thus, the magnitude of \mathbf{B}_0 is predominant in affecting \mathbf{M} , M_0 , T_1 , and T_2 . \mathbf{B}_0 is constant on an MRI scanner, and so also are M_0 , T_1 , and T_2 .

2.1.6 Chemical Shift

The Larmor frequency is only an approximation of a nucleus's true resonance frequency because the molecular electronic environment around the nuclei induces small changes in the magnetic field. In a fat molecule, a triglyceride for example, the proton nuclei reside in electron clouds that shield them from the full effect of the external \mathbf{B}_0 . In contrast, the proton nuclei of water molecule experience far less shielding as the highly electronegative oxygen atom pulls electrons away. Besides the effects of nearby electronegative atoms, the motion of electrons in π systems induces a magnetic field that can also shield and deshield nuclei. Taken collectively, differential shielding causes slight differences in resonance frequency. This shift in frequency is called chemical shift; nuclei of distinct molecules are shifted along the spectral axis. As resonance frequency is integral to spatial encoding (as described in Section 2.1.3), the consequences of chemical shift can be readily seen in spatial mismapping. In this example, if water and fat are both present in a given voxel, an imaging sequence set to the Larmor frequency of water protons will produce an image in which fat protons, being at a lower frequency, appear a few voxels shifted in the frequency encoding direction.

This chemical shift phenomenon essentially provides each molecule with a unique spectral signature that can induce imaging artifacts but can also be utilized for additional biomedical information. Turning from imaging to spectroscopy, a chemical shift spectrum can be acquired to quantify the presence of several molecules in a given volume (Figure 2.4). The actual methodology of acquiring chemical shift spectra is described later. Suffice to say, the chemical shift dimension (in Hz or ppm) can be acquired in addition to three or fewer spatial dimensions and time, enabling the simultaneous analysis of several molecules—how their concentrations increase, decrease, or remain constant—through time. If the species are reactants and products of each other, then the progress and rate of the reaction can also be quantified.

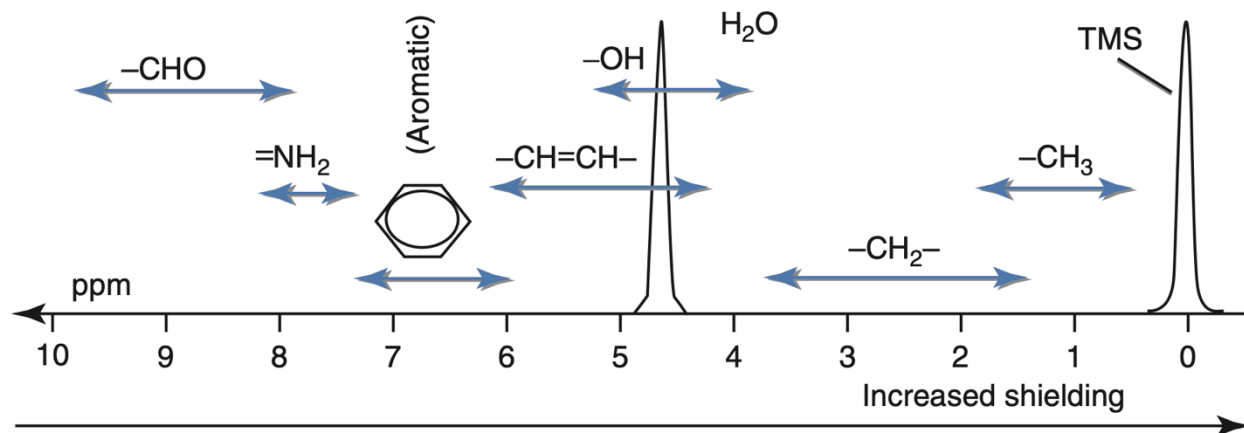


Figure 2.4. The chemical shifts resulting from the presence of common organic moieties. Polar moieties result in decreased shielding while nonpolar moieties result in increased shielding, with resonance frequencies closer to 0 parts per million (ppm). Tetramethylsilane (TMS) serves as an internal standard for calibrating chemical shift. Adapted from Bottomley PA.⁶

As hinted upon earlier, the same MR physics apply to other nuclei, such as that of ^{13}C . This enables imaging and spectroscopy of other nuclei, and the molecules they find themselves in. Despite challenges of lower natural abundance and a gyromagnetic ratio that results in less polarization, ^{13}C spectra can be acquired in like manner (Figure 2.5).⁷ Further discussion on hyperpolarization, a method that enables high-SNR, rapid ^{13}C imaging and spectroscopy *in vivo*, will be presented later.

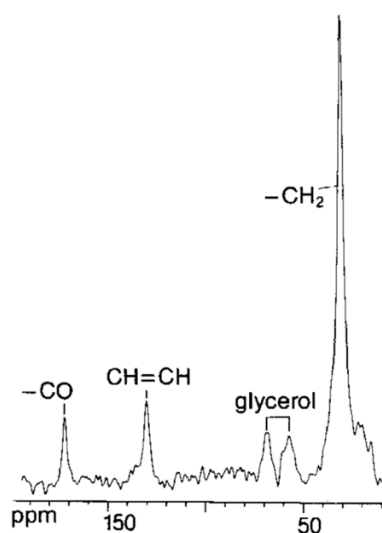


Figure 2.5. A ^{13}C spectrum obtained from endogenous signal in the human leg using a surface coil. Adapted from Bottomley PA *et al.*⁷

2.1.7 Creation of Images from Magnetic Resonance Acquisitions

Magnetic resonance imaging (MRI) translates NMR techniques into volumetric 2D and 3D imaging, with spatial resolutions of a few millimeters and excellent soft tissue contrast due to differential spin relaxation behaviors in each tissue type. As described previously, FIDs are acquired in k -space and Fourier transformed from spatial frequencies to images. Traversing k -space is achieved by gradients that spatially encode FIDs. A standard 2D imaging sequence can thus be represented by a pulse sequence composed of the amplitude and timing of the RF pulse, gradient waveforms, and data acquisition (Figure 2.6).

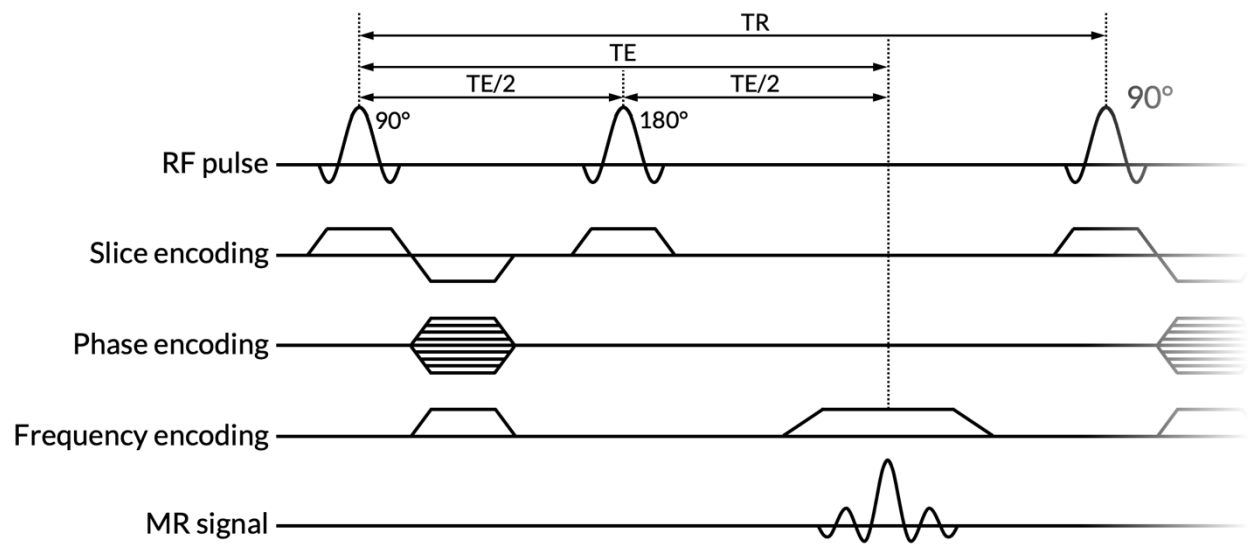


Figure 2.6. A generic spin-echo pulse sequence diagram with a 90° pulse followed by a 180° pulse. The lines beneath correspond to slice, phase, and frequency encoding gradients. The bottom line is the MR signal. The duration between the 90° pulse and the MR signal is the echo time (TE). This is such because the 180° pulse refocuses the dephasing spins. Consequently, the spins rephase and peak an equivalent TE/2 period after the 180° pulse. The duration between the first 90° pulse and the subsequent 90° pulse is the repetition time (TR). This pulse sequence repeats until all the data is acquired.

Repetition time (TR) is the time duration between consecutive RF excitations and thus affects the amount of T_1 relaxation that can occur before the next pulse. Modulating the TR thus affects T_1 contrast in the image. Echo time (TE) is the duration from the peak of the RF pulse to the moment

when gradients traverse the center of k -space. Spins can be refocused using gradients and thus, the timing of these gradients as governed by TE affects T_2 contrast in the image.

Echo-planar imaging (EPI) is one pulse sequence of interest because it enables rapid multi-slice acquisition. It uses a spectral-spatial pulse that is selective in both frequency and space. The duration of its sub-lobes (τ_1) determines the width of the spectral stop-band while the net duration of the pulse (τ_2) determines the full-width at half-maximum (FWHM) of the spectral pass-band (Figure 2.7).⁸ A Gaussian envelope allows it to achieve the narrowest spectral selectivity. Such pulses can be used to selectively excite molecules of interest depending on the choice of center frequency.

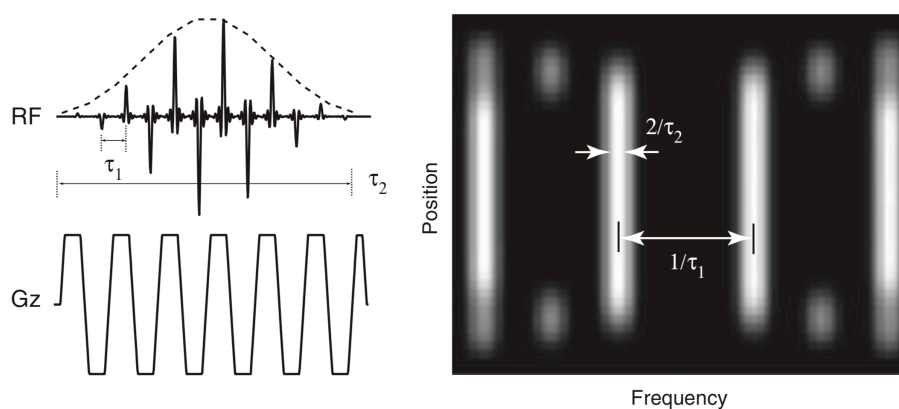


Figure 2.7. Left: the RF and gradient waveforms with the important timing considerations indicated by τ_1 (the duration between sub-lobes) and τ_2 (the net duration of the pulse). The broken line shows the envelope of the RF pulse, which determines the shape of the spectral pass-bands. Right: the excitation profile of the pulse (white indicates 45° excitation; black indicates 0° excitation) as a function of frequency. Adapted from Lau et al.⁸

Signal readout in an EPI sequence uses oscillating gradients for efficient sampling and relative robustness to off-resonance artifacts (Figure 2.8). Gradients can be “symmetric” or “flyback,” each with their set of advantages and disadvantages.⁹ Flyback gradients have reduced SNR due to a lack of encoding during the flyback phases but as readout occurs only on a single lobe, the sequence is more insensitive to timing errors and spatial distortions in the images. Conversely, symmetric gradients acquire even and odd lines of k -space (first left-to-right and then right-to-left) for faster imaging but mismatches can result in shifts and distortions in the phase-encoding direction.

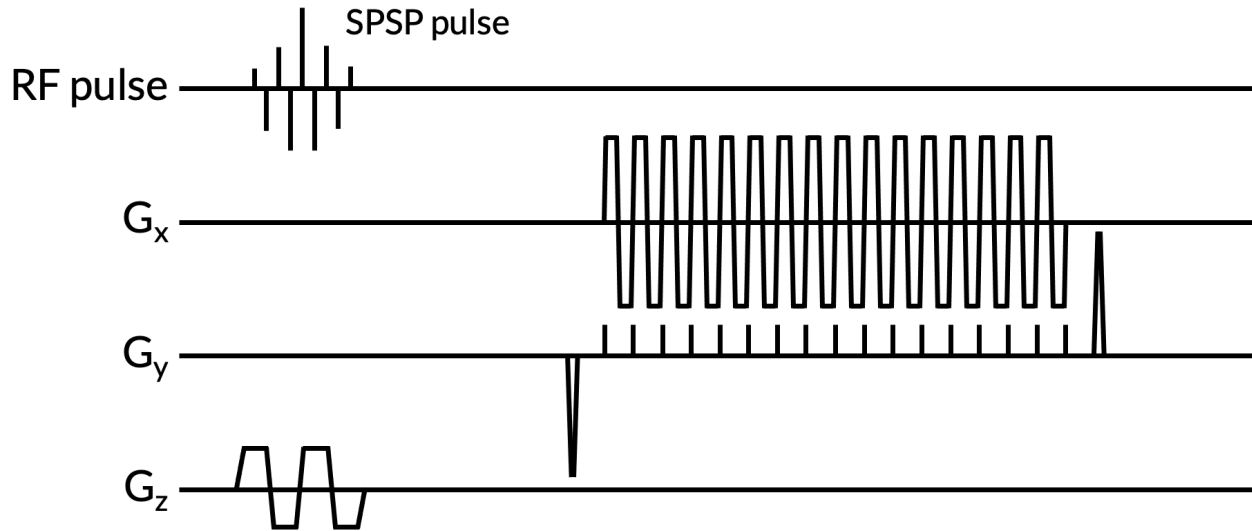


Figure 2.8. An echo-planar imaging (EPI) pulse sequence with a spectral-spatial (SPSP) RF pulse followed by a symmetric readout gradient.

MR signal acquisition is not limited to only three spatial dimensions. Acquisition can also be extended into a fourth spectral dimension using spectroscopic imaging techniques. The simplest approach is magnetic resonance spectroscopic imaging (MRSI) in which spectroscopic or chemical shift information is treated as a complete, separate dimension in addition to the three spatial dimensions, which entails additional scan time.¹⁰ Spectroscopic readout follows with no gradients applied. This process is then repeated for all phase encoding steps in all three spatial dimensions. Scan time quickly accumulates which is difficult for imaging compounds with decaying signals (e.g. hyperpolarized ^{13}C MRI described later).

Echo-planar spectroscopic imaging (EPSI) enables spectroscopic imaging for ^{13}C compounds with realistic scan times. In this pulse sequence, readouts are performed during a rapidly switching frequency encoding gradient, allowing for acquisition in one spatial dimension and a spectroscopic dimension in the same single readout (Figure 2.9).¹⁰ The number of echoes acquired determines the number of spectral points. Correspondingly, the spacing between echoes, ΔTE , determines the spectral bandwidth; if one desires to increase the spectral bandwidth (and thus acquire signal at more

disparate frequencies), one must sacrifice acquisition of more spatial points. The result is a 4D data matrix with each voxel in 3D space containing the full acquired spectrum.

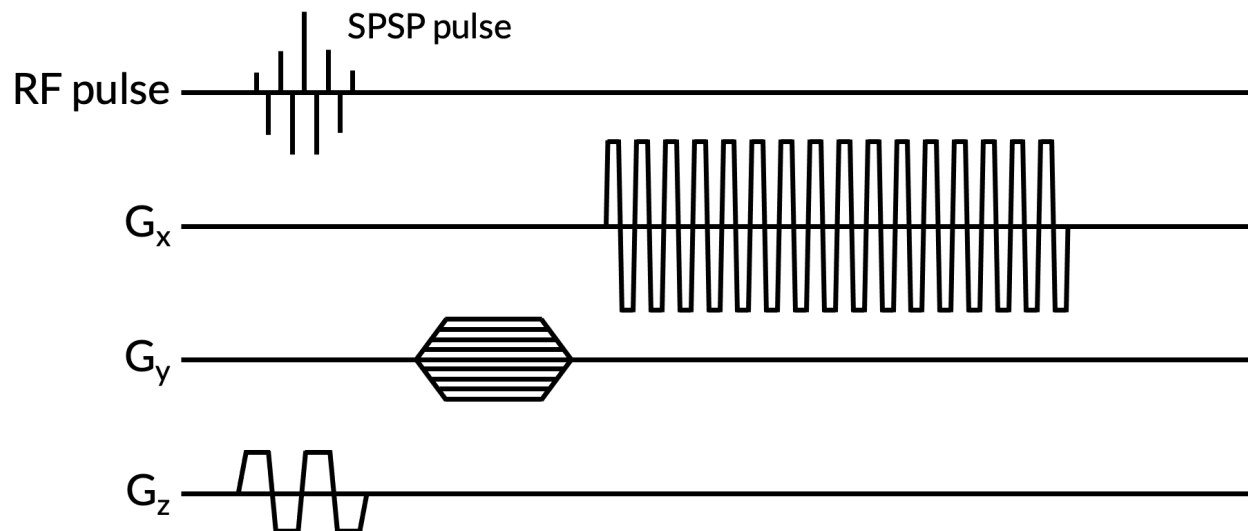


Figure 2.9. An echo-planar spectroscopic imaging (EPI) pulse sequence with a spectral-spatial (SPSP) RF pulse followed by a phase-encoding gradient and a symmetric readout gradient.

Because of its spectroscopic nature, EPI is more robust to B_0 inhomogeneities; frequency shifts manifest in a shift in the spectral dimension but with a sufficiently large bandwidth, there are little artifacts. Moreover, spectroscopic approaches reduce the need for prior knowledge about spectral resonances of the molecules of interest, with the spectrum itself informing the researcher of relative abundance through time. However, if the resonance frequencies of molecules of interest are known *a priori* and the spectrum is sparse, EPI and similar acquisitions, in which the excitation is metabolite-specific, are faster.

An important consideration in implementing pulse sequences is the signal-to-noise ratio (SNR). SNR is proportional to the sequence, its inherent contrast, voxel size (given by the spatial resolution in each dimension, Δx , Δy , and Δz), and the square root of the measurement time, T_{meas} (Eqn. 2.17):

$$SNR \propto f(M_0, T_1, T_2) \Delta x \Delta y \Delta z \sqrt{T_{meas}} \quad (2.17)$$

The smaller the voxel, the lower the SNR assuming evenly spread metabolite signals; this makes intuitive sense as in a smaller given volume (the voxel), there are fewer magnetic dipoles that constitute a net magnetization vector. Measurement time is itself a product of the number of signal averages, phase encode, and the data acquisition time per TR. It can be quickly observed that SNR is a major limitation if one desires to have half the spatial resolution in each dimension because this entails an 8-fold increase in measurement time to maintain the same SNR. These parameters must be taken into consideration in order to gain the maximum benefit of the imaging sequence.

2.2 Introduction to Hyperpolarized ^{13}C Magnetic Resonance

Imaging

Extending the imaging capabilities of MRI to nuclei other than that of ^1H is of great scientific interest. Organic molecules are carbon-based. Methods to image carbon nuclei would greatly expand the suite of molecular frequencies one can probe. However, the dominant isotope of carbon is ^{12}C , invisible to MRI given its zero spin. The only other stable isotope is ^{13}C , which conveniently possess a non-zero spin. But its low natural abundance (1.1%) makes imaging ^{13}C challenging. Furthermore, its gyromagnetic ratio is four-fold lower than that of ^1H , which contributes to a low polarization at thermal equilibrium (Eqns. 2.2 and 2.3). With a mere 1.1% of all carbon nuclei in a given volume actually being MRI-visible, spin population differences are miniscule, resulting in hardly a net magnetization to be detected. Finally, carbonyl ^{13}C nuclei have a long T_1 ([$1\text{-}^{13}\text{C}$]pyruvate has a T_1 of 67 s at 3.0 T), meaning that recovery times to a maximum polarization after each excitation would be unrealistic.¹¹ Collectively, sensitivity to ^{13}C is too low for practical application.

Yet, in spite of these seeming enormous challenges, technological advances have been made to not only enable MR imaging of ^{13}C compounds, but to do so dynamically through time, for multiple

molecules simultaneously, with coverage in all three spatial dimensions and impressive spatial resolution, and, best of all, *in vivo*.

2.2.1 Dissolution Dynamic Nuclear Polarization

Dissolution dynamic nuclear polarization (dDNP) is a technique that overcomes many of the previously mentioned challenges by increasing ^{13}C nuclei polarization over 10,000-fold from thermal polarizations, enabling imaging of ^{13}C -labeled molecules.¹² This is carried out by bringing a homogeneous mixture of ^{13}C -labeled compounds and free radicals into a 5 T magnetic field at approximately 0.8 K. With a gyromagnetic ratio of 28,025 MHz/T (about 2,600-fold greater than that of ^{13}C), electrons experience near 100% polarization at this field and low temperature while ^1H and ^{13}C nuclei are polarized less (Figure 2.10). But in this solid state, electron polarization is transferred to ^{13}C nuclei by microwave irradiation, thus achieving around 40% polarization, greater than 10,000-fold enhancement of ^{13}C nuclear polarization.

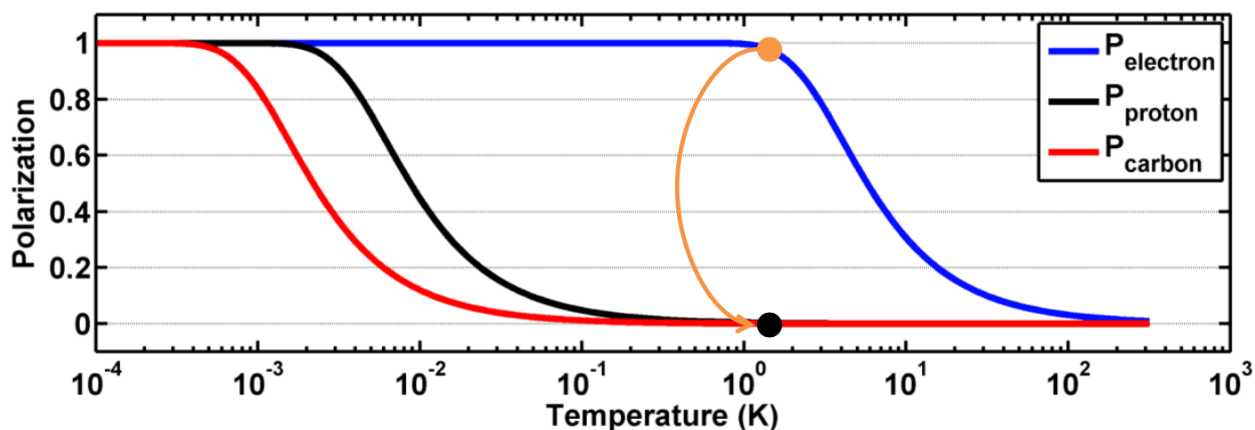


Figure 2.10. Comparison of polarization for electrons, ^1H nuclei (protons), and ^{13}C nuclei over a range of temperatures. Used with permission from Gordon JW.

The solid-state compound can then be dissolved using superheated water. The radical is filtered out, and the concentration of the ^{13}C -labeled compound is measured. Once in its liquid state, outside of its previous low temperature, high magnetic field environment, the signal begins to decay according to

its T_1 time constant, so signal acquisition must occur in the next minute for there to be useful data (Figure 2.11). Overall, dDNP enables dramatically improved SNR of ^{13}C signals with acquisition times mere fractions of what would otherwise be necessary (Figure 2.12).

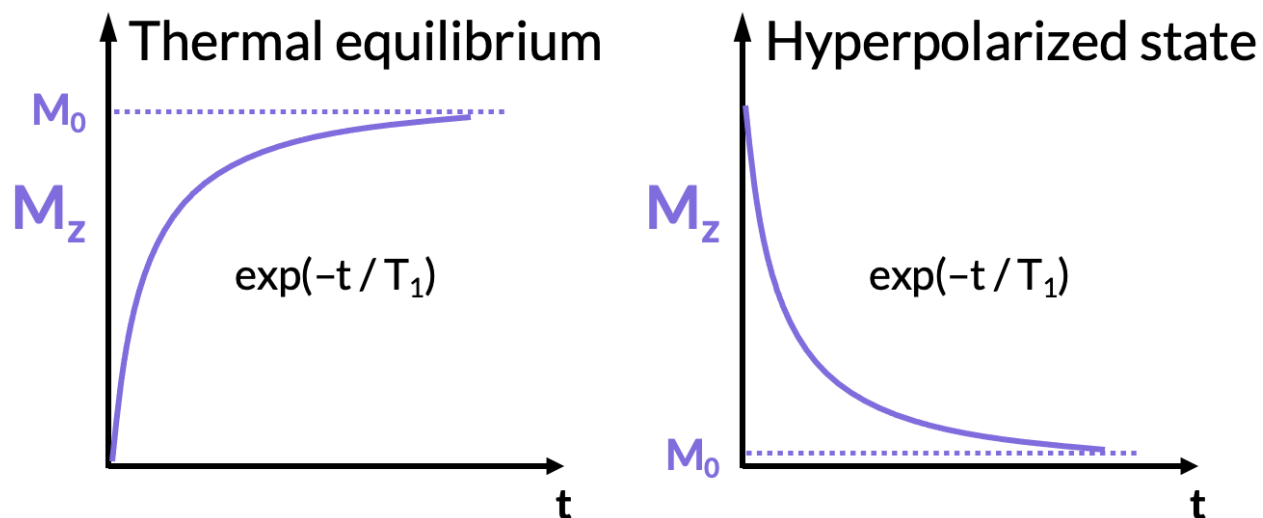


Figure 2.11. T_1 relaxation for a system at thermal equilibrium with a magnetization beginning from zero and reaching M_0 compared to T_1 relaxation for a system in a hyperpolarized state with a magnetization decaying from a magnitude several fold larger than M_0 . The magnetization reaches its equilibrium value of M_0 in both cases but from different directions.

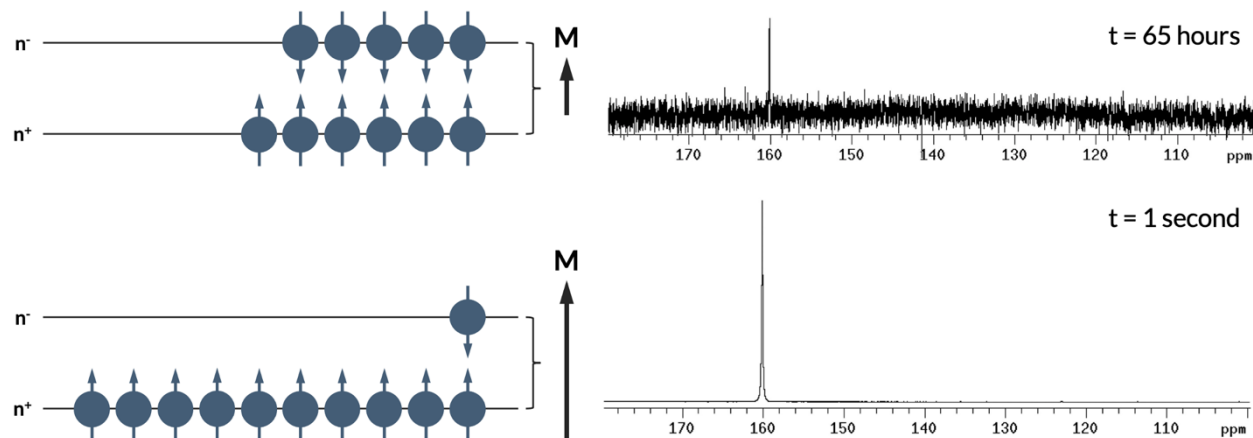


Figure 2.12. Comparison of ^{13}C urea spectra from a thermally polarized state (top) versus from a hyperpolarized state (bottom). The spectrum from the thermally polarized state was acquired under Ernst-angle conditions and averaged over 65 hours. The spectrum from the hyperpolarized state was acquired at 20% polarization and was acquired in less than a second. A visualization of the spin population differences for the two states are shown on the left side. Adapted from Ardenkjær-Larsen *et al.*¹²

While the gyromagnetic ratio is unchanged, using a ^{13}C -enriched sample addresses concerns of low natural abundance. Moreover, now that hyperpolarized signal decays, the long T_1 is to the researcher's advantage; instead of observing signal recovery, we observe decay over the course of a minute, more than sufficient time to extract information on dynamic metabolic processes.

Hyperpolarized ^{13}C MR clinical research thus begins with a clinical-grade sterile pharmaceutical preparation step of the ^{13}C -labeled compound, which is loaded into a polarizer (GE SPINlab) (Figure 2.13). Specialized ^{13}C detector hardware is integrated with the MR scanner. Using a fast ^{13}C pulse sequence, images or spectroscopic data are acquired which are post-processed into dynamic parameter images.

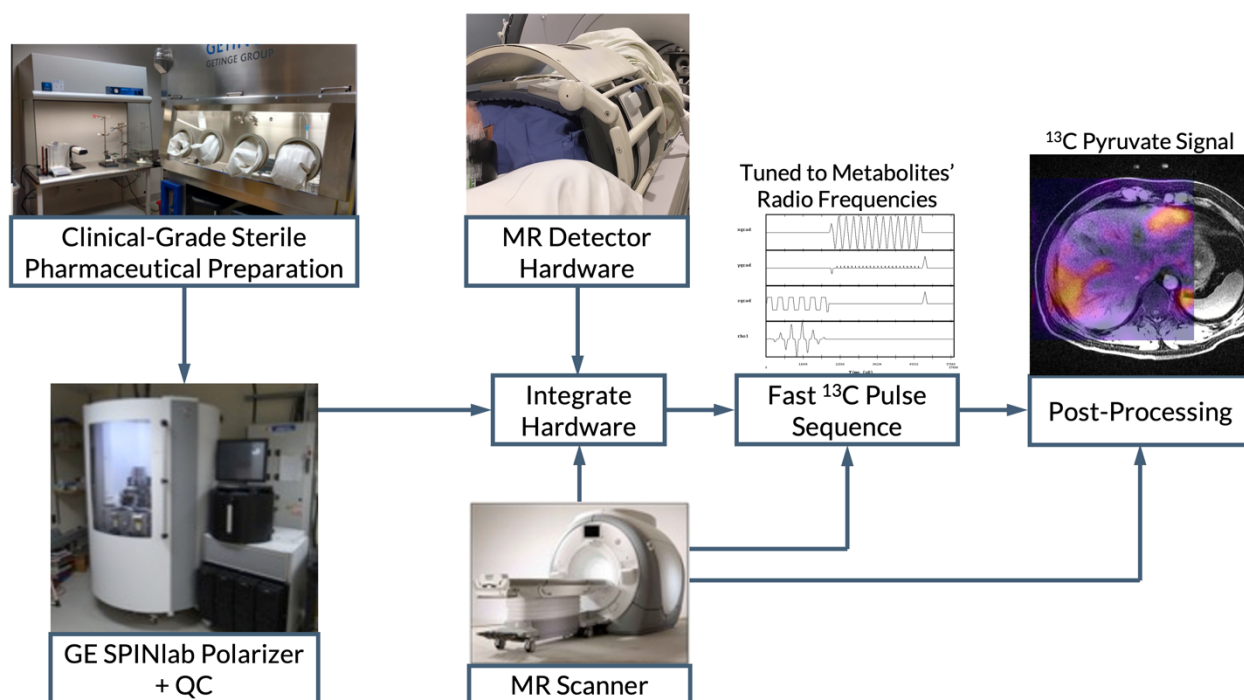


Figure 2.13. Summary of necessary components for hyperpolarized ^{13}C MR clinical research.

2.2.2 Challenges in Hyperpolarized ^{13}C MRI Acquisition

The longitudinal magnetization $M_z(t)$ now decays to thermal equilibrium. Eqn. 2.12 can be re-written in the context of hyperpolarized signals:

$$M_z(t) = M_0 + (M_{z,HP} - M_0) \exp\left(\frac{-t}{T_1}\right) \cong M_{z,HP} \exp\left(\frac{-t}{T_1}\right) \quad (2.18)$$

$M_{z,HP}$ is the initial hyperpolarized longitudinal magnetization which decays to thermal equilibrium, M_0 .¹³ This approximation holds true if $M_{z,HP} \gg M_0$, which dDNP enables. But now that signal decays, each RF excitation pulse consume the non-renewable, finite hyperpolarized magnetization. For n RF excitations at the same flip angle θ , the longitudinal and transverse magnetizations at time t are:¹³

$$M_z(t) = M_{z,HP} \exp\left(\frac{-t}{T_1}\right) \cos^{n-1} \theta \quad (2.19)$$

$$M_{xy}(t) = M_{z,HP} \exp\left(\frac{-t}{T_1}\right) \cos^{n-1} \theta \sin \theta \quad (2.20)$$

Signal averaging or experiments requiring 90° flip angles are therefore mostly incompatible with hyperpolarized experiments.

This necessitates proper calibration of RF power prior to injection and scanning. Because there is little endogenous ^{13}C signal in the human body, phantoms containing carbon-based compounds, such as ethylene glycol and dimethyl silicone, can be used as an approximation. Transmit field B_1^+ corrections may thus be required to resolve errors.

Another challenge is the development of fast imaging sequences. This is particularly important for imaging organs in the abdomen because blurring in the phase-encode direction can occur with respiratory motion. \mathbf{B}_0 and \mathbf{B}_1 inhomogeneities further complicate uniform excitation of spins. Finally, although dDNP allows for the practicality of HP ^{13}C MRI, noise is nevertheless always present

and robust denoising methods are required. Addressing these challenges are an ongoing effort and subsequent chapters will detail recent advancements made.

2.2.3 Hyperpolarized ^{13}C Magnetic Resonance Imaging with $[1-^{13}\text{C}]$ pyruvate

Many ^{13}C -labeled compounds exist but one of widespread study is $[1-^{13}\text{C}]$ pyruvate. Pyruvate sits at the intersection of prominent metabolic pathways: glycolysis (and subsequently oxidative phosphorylation) and aerobic glycolysis. The former is the primary pathway of metabolism in mammalian cells while the latter is upregulated in tumors, a phenomenon known as the Warburg effect.^{14–16} The conversion of pyruvate to either acetyl CoA (for oxidative phosphorylation) or lactate (for aerobic glycolysis) is of much clinical interest.^{17–21} By quantifying the rate at which pyruvate is exchanged into these downstream metabolites, we can quantitatively characterize healthy and diseased states. Therefore, adding a ^{13}C isotope at the carbon 1 position allows us to probe pyruvate's conversion into alanine, lactate, carbon dioxide, and bicarbonate (Figure 2.14).

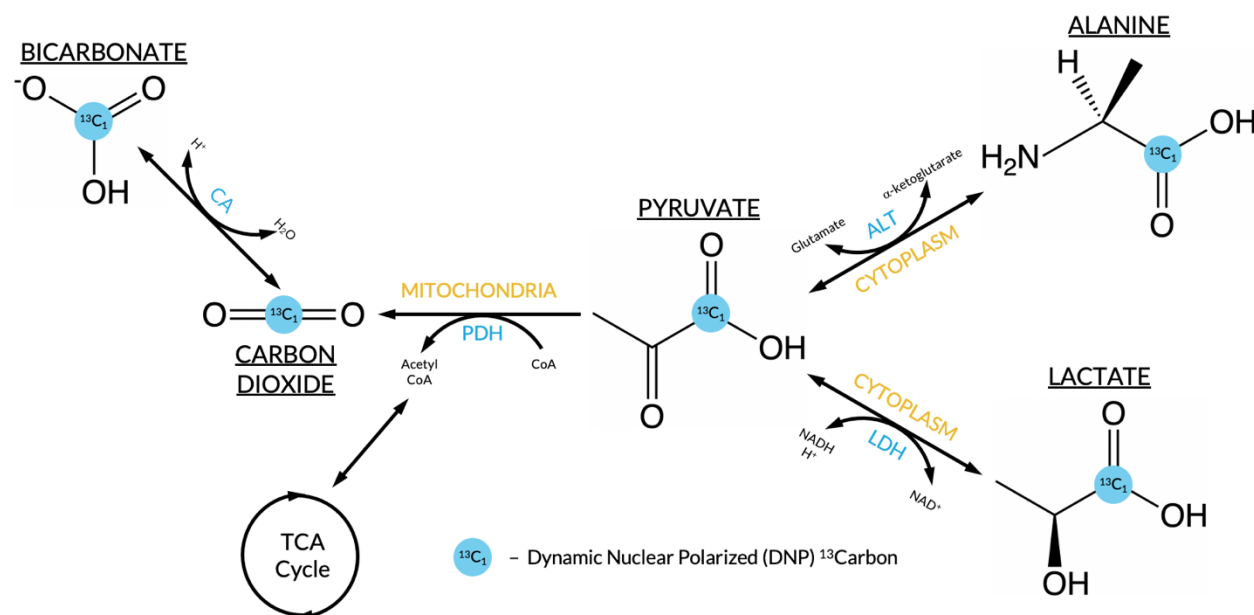


Figure 2.14. Metabolic pathways for $[1-^{13}\text{C}]$ pyruvate. The carbon 1 position is conserved in pyruvate's conversion to alanine, lactate, carbon dioxide, and bicarbonate.

Metabolite data can be kinetically modeled to extract apparent first-order reaction rates. That of the conversion of pyruvate to lactate, k_{PL} , is a potential biomarker elevated in cancer and reflects treatment response in animal models and humans. Among a variety of methods for reaction rate estimation, a two-site inputless kinetic model provides the most robustness to differences in acquisition timing, injection volumes, and polarization levels between scans.²² This particular model, used in the works to be presented later, assumes negligible reverse conversion from lactate to pyruvate and fixed T_1 values. But its versatility makes it a reliable model for quantifying kinetic rate constants.

[1-¹³C]pyruvate has been used to study metabolic processes of healthy and diseased states in a variety of human organs. As of the writing of this dissertation, there are 50+ ongoing hyperpolarized [1-¹³C]pyruvate human studies being carried out worldwide, with explorations in cancer, fatty liver disease, brain disorders, kidney disease, and cardiac disease.

2.3 MRI—A Testament to the Ingenuity of the Human Mind

Before presenting some work using HP ¹³C MRI, which allows us to perceive into the dynamic metabolic processes within human organs, I would like to briefly remark on my awe and utmost respect for the scientists who brought forth this very technology. When I first began in this field of MRI, I learned of its equations, its physics, and of all the hardware and software that had to work together optimally to transform a bunch of randomly spinning nuclei into remarkable images.

Many times, I could not believe that the technology at my fingertips actually existed, defying all of the factors against its viability. For one, thermal polarization provides only a minute percentage of polarization; even with this alone, MRI would not appear as a promising technology. As a result, to acquire any useful signal, you need a *lot*—truly an absurdly large amount—of spins. Then you have factor in relaxation processes that begin instantaneously and finish within tens of milliseconds—

electronics that could detect such fleeting signal variations would have to be so very precise. Finally, consider chemical shifts and magnetic fields inhomogeneities and imperfections, and now nuclei are spinning at wildly different frequencies from those initially predicted. It would seem that even if you could detect any signal, it would only be shrouded by an abundance of spurious artifacts.

Yet brilliant minds pursued undaunted and not only made this technology feasible—and now indispensable to patient care—but also translated it to even more challenging nuclei like ^{13}C . So I find myself awestruck at the ingenuity of the human mind, which never shies away from possibility even when the laws of physics are unreasonably stingy. I stand upon the shoulders of giants, only able to do what I did because of their insatiable curiosity and unbridled brashness. It is a privilege to have contributed to this field. As one who has inherited much from the work of these scientific pioneers, I follow in their footsteps and, in the small way that I can, present the following chapters to my fellow researchers of today and tomorrow, for their minds to consider.

2.4 References

1. Levitt MH. *Spin Dynamics: Basics of Nuclear Magnetic Resonance*. 2nd ed. John Wiley & Sons, Inc.; 2013.
2. Nishimura DG. *Principles of Magnetic Resonance Imaging*. Stanford University; 2010.
3. Bottomley PA, Griffiths JR. *Handbook of Magnetic Resonance Spectroscopy In Vivo: MRS Theory, Practice and Applications*. (Bottomley PA, Griffiths JR, eds.). John Wiley & Sons, Inc.; 2016.
4. Bernstein M, King K, Xiaohong J. *Handbook of MRI Pulse Sequences*. Elsevier; 2004.
doi:10.1016/B978-0-12-092861-3.X5000-6
5. Hashemi RH, Lisanti CJ, Bradley WGJ. *MRI: The Basics*. Wolters Kluwer; 2018.
6. Bottomley PA. The Basics. In: *EMagRes*. John Wiley & Sons, Ltd; 2015:505-524.
doi:10.1002/9780470034590.emrstm1485
7. Bottomley PA, Hardy CJ, Roemer PB, Mueller OM. Proton-decoupled, overhauser-enhanced, spatially localized carbon-13 spectroscopy in humans. *Magn Reson Med*. 1989;12(3):348-363.
doi:10.1002/mrm.1910120307
8. Lau AZ, Chen AP, Hurd RE, Cunningham CH. Spectral-spatial excitation for rapid imaging of DNP compounds. *NMR Biomed*. 2011;24(8):988-996. doi:10.1002/nbm.1743
9. Cunningham CH, Vigneron DB, Chen AP, et al. Design of flyback echo-planar readout gradients for magnetic resonance spectroscopic imaging. *Magn Reson Med*. 2005;54(5):1286-1289. doi:10.1002/mrm.20663
10. Mulkern R V., Panych LP. Echo Planar Spectroscopic Imaging. *Magn Reson*. 2001;13(4):213-237.
11. Wang ZJ, Ohliger MA, Larson PEZ, et al. Hyperpolarized 13C MRI: State of the art and future directions. *Radiology*. 2019;291(2):273-284. doi:10.1148/radiol.2019182391
12. Ardenkjær-Larsen JH, Golman K, Gram A, et al. Increase of signal-to-noise of more than

- 10,000 times in liquid state NMR. *Discov Med.* 2003;100(18):10158-10163.
13. Gordon JW, Larson PEZ. Pulse sequences for hyperpolarized MRS. *eMagRes.* 2016;5(2):1229-1246. doi:10.1002/9780470034590.emrstm1451
 14. Warburg O. On the origin of cancer cells. *Science (80-).* 1956;123(3191):309-314. doi:10.1126/science.123.3191.309
 15. Hu S, Balakrishnan A, Bok RA, et al. ¹³C-pyruvate imaging reveals alterations in glycolysis that precede c-Myc-induced tumor formation and regression. *Cell Metab.* 2011;14(1):131-142. doi:10.1016/j.cmet.2011.04.012
 16. Keshari KR, Sriram R, Van Criekinge M, et al. Metabolic reprogramming and validation of hyperpolarized ¹³C lactate as a prostate cancer biomarker using a human prostate tissue slice culture bioreactor. *Prostate.* 2013;73(11):1171-1181. doi:10.1002/pros.22665
 17. Aggarwal R, Vigneron DB, Kurhanewicz J. Hyperpolarized 1-[¹³C]-Pyruvate Magnetic Resonance Imaging Detects an Early Metabolic Response to Androgen Ablation Therapy in Prostate Cancer. *Eur Urol.* 2017;72(6):1028-1029. doi:10.1016/j.eururo.2017.07.022
 18. Chen HY, Aggarwal R, Bok RA, et al. Hyperpolarized ¹³C-pyruvate MRI detects real-time metabolic flux in prostate cancer metastases to bone and liver: a clinical feasibility study. *Prostate Cancer Prostatic Dis.* 2020;23(2):269-276. doi:10.1038/s41391-019-0180-z
 19. Park I, Larson PEZ, Gordon JW, et al. Development of methods and feasibility of using hyperpolarized carbon-13 imaging data for evaluating brain metabolism in patient studies. *Magn Reson Med.* 2018;80(3):864-873. doi:10.1002/mrm.27077
 20. Cunningham CH, Lau JYC, Chen AP, et al. Hyperpolarized ¹³C Metabolic MRI of the Human Heart: Initial Experience. *Circ Res.* 2016;119(11):1177-1182. doi:10.1161/CIRCRESAHA.116.309769
 21. Abeyakoon O, Latifoltojar A, Gong F, et al. Hyperpolarised ¹³C MRI: a new horizon for

non-invasive diagnosis of aggressive breast cancer. *BJR Case Rep.* 2019;5(3):20190026.

doi:10.1259/bjrcr.20190026

22. Larson PEZ, Chen HY, Gordon JW, et al. Investigation of analysis methods for hyperpolarized ¹³C-pyruvate metabolic MRI in prostate cancer patients. *NMR Biomed.* 2018;31(11):e3997. doi:10.1002/nbm.3997

Chapter 3

Hyperpolarized ^{13}C -pyruvate MRI Detects Real-Time Metabolic Flux in Prostate Cancer Metastases to Bone & Liver: A Clinical Feasibility Study

Chen HY, Aggarwal R, Bok RA, Ohliger MA, Zhu Z, Lee P, Gordon JW, van Criekinge M, Carvajal L, Slater JB, Larson PEZ, Small EJ, Kurhanewicz J, and Vigneron DB. Hyperpolarized ^{13}C -pyruvate MRI detects real-time metabolic flux in prostate cancer metastases to bone and liver: a clinical feasibility study. *Prostate Cancer and Prostatic Diseases*. November 2019. DOI: 10.1038/s41391-019-0180-z.

3.1 Abstract

3.1.1 Background

Hyperpolarized (HP) ^{13}C -pyruvate MRI is a stable-isotope molecular imaging modality that provides real-time assessment of the rate of metabolism through glycolytic pathways in human prostate cancer. Heretofore this imaging modality has been successfully utilized in prostate cancer only in localized disease. This pilot clinical study investigated the feasibility and imaging performance of HP ^{13}C -pyruvate MR metabolic imaging in prostate cancer patients with metastases to the bone and/or viscera.

3.1.2 Methods

Six patients who had metastatic castration-resistant prostate cancer were recruited. Carbon-13 MR examination were conducted on a clinical 3T MRI following injection of 250 mM hyperpolarized ^{13}C -pyruvate, where pyruvate-to-lactate conversion rate (k_{PL}) was calculated. Paired metastatic tumor biopsy was performed with histopathological and RNA-seq analyses.

3.1.3 Results

We observed a high rate of glycolytic metabolism in prostate cancer metastases, with a mean k_{PL} value of $0.020 \pm 0.006 \text{ s}^{-1}$ and $0.026 \pm 0.000 \text{ s}^{-1}$ in bone ($N = 4$) and liver ($N = 2$) metastases, respectively. Overall, high k_{PL} showed concordance with biopsy-confirmed high-grade prostate cancer including neuroendocrine differentiation in one case. Interval decrease of k_{PL} from 0.026 at baseline to 0.015 s^{-1} was observed in a liver metastasis 2 months after the initiation of taxane plus platinum chemotherapy. RNA-seq found higher levels of the lactate dehydrogenase isoform A (Ldha , 15.7 ± 0.7) expression relative to the dominant isoform of pyruvate dehydrogenase (Pdha1 , 12.8 ± 0.9).

3.1.4 Conclusions

HP ^{13}C -pyruvate MRI can detect real-time glycolytic metabolism within prostate cancer metastases, and can measure changes in quantitative k_{PL} values following treatment response at early time points. This first feasibility study supports future clinical studies of HP ^{13}C -pyruvate MRI in the setting of advanced prostate cancer.

3.2 Introduction

Metastatic castration-resistant prostate cancer (mCRPC) is the most lethal form of the disease, accounting for 31,000 deaths/year in the United States.¹ More than 90% of patients with mCRPC develop osseous metastases and nearly half have bone as the only site of the disease.^{2,3} Visceral metastases occur in 10–15% of mCRPC patients and are associated with high disease burden and poor prognosis.^{4,5} Despite the emergence of multiple therapies that have been shown to prolong overall survival, including androgen pathway inhibitors, immunotherapy, radiopharmaceuticals, and chemotherapeutics, there is an unmet need for novel therapies to further improve treatment outcomes.^{3,6,7}

A limitation to the development of novel systemic therapies in mCRPC, especially with bone predominance without measurable disease by conventional imaging criteria, is the lack of validated imaging biomarkers to provide real-time response monitoring. Automated bone indices of radionuclide bone scans have not been sufficiently prospectively validated, and provide minimal information with respect to direct tumor metabolic activity. Also, changes in bone scintigraphy with response to therapy can be slow to occur and are complicated by flare phenomena and differences in uptake between sclerotic versus lytic lesions.⁸ Newer PET analogs, including agents targeting prostate-

specific membrane antigen, have shown promise as a diagnostic tool, but have limited and conflicting data to support their use to monitor therapeutic response and resistance.^{9,10}

Hyperpolarized ^{13}C MRI (HP ^{13}C MRI) is a stable-isotope molecular imaging approach that probes pyruvate-to-lactate metabolism mediated by the upregulation of LDH enzymatic activity in cancer due to the Warburg effect (Figure 3.1).¹¹⁻¹⁴ High glycolytic activity and rapid pyruvate-to-lactate conversion are signatures of aggressive cancer.^{13,15,16} There is also a broad consensus that the pharmacologic action of chemotherapy is tightly coupled with metabolic pathways, and responses to chemotherapy might be reflected as modulations of cancer metabolism.¹⁷⁻¹⁹ Heretofore HP ^{13}C -pyruvate MRI has been successfully utilized in prostate cancer only in localized disease. This imaging modality has been used to detect metabolic responses to chemohormonal therapy in primary prostate cancer,²⁰ at earlier time points than conventional multiparametric MRI.

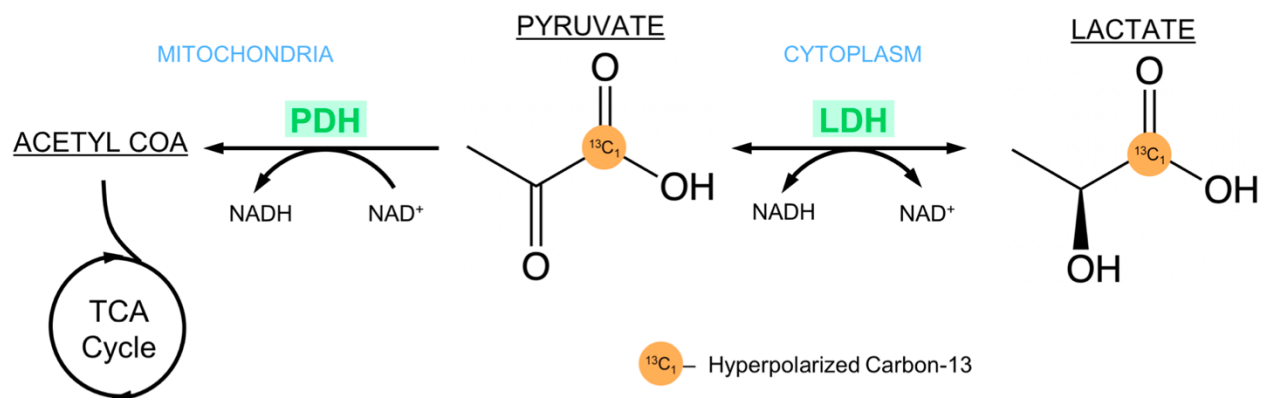


Figure 3.1. An illustration of LDH-mediated aerobic glycolysis and relevant metabolic pathways.

In the current pilot imaging study, we aimed to broaden the scope of HP ^{13}C -pyruvate MRI to the metastatic CRPC setting, with direct visualization of skeletal and visceral metastases, in order to provide real-time assessment of tumor metabolism and metabolic response to therapy.

3.3 Methods

3.3.1 Patient Selection

Key eligibility criteria included histologic evidence of prostate cancer, progressive mCRPC by PCWG2 criteria,⁷ ECOG performance status of 0 or 1, and adequate end organ function. All patients underwent restaging CT and bone scans prior to enrollment, and had at least one identified lesion amenable to HP ¹³C MRI. Patient recruitment and HP ¹³C-pyruvate studies were conducted in compliance with an IRB-approved protocol (NCT02911467), and all patients provided written informed consent.

3.3.2 HP ¹³C Patient MRI Studies

GMP [1-¹³C]pyruvic acid (Sigma-Aldrich Isotec, Miamisburg OH) was prepared and loaded in pharmacy kits in accordance with the IRB- and FDA IND-approved stable-isotope manufacturing process. The pyruvic acid was polarized in a 5T SPINLab (GE Healthcare, Chicago IL) clinical trial polarizer for 2.5–3h. Dissolutions yielded 237±10 mM sterile pyruvate with 37.1±3.2% polarization, 0.6±0.4 μM residual radical and 31.0±0.6 °C temperature, 7.5±0.3 pH, 63±4 s dissolution-to-injection time. A pharmacist oversaw the automatic quality control and integrity of the sterilization filter, and released the dose for injection once sterility and safety criteria were met.^{21,22}

All studies were conducted on a clinical 3T MRI (MR750, GE Healthcare) equipped with multinuclear spectroscopy capabilities. A custom surface coil with figure-eight configuration was applied for both ¹³C transmit and receive. A 16-channel abdominal array (GE Healthcare) was used for proton imaging.

Follow-up ¹³C-pyruvate MRI was optional after the initiation of systemic therapy for the treatment of mCRPC.

3.3.3 Data Acquisition & Analysis

The HP-¹³C acquisition was conducted using a 2D dynamic MR spectroscopic imaging pulse sequence with a slice-selective spectral-spatial excitation, followed by phase-encode and echo-planar spectroscopic imaging readout.¹¹ Pulse sequence parameters were as follows: 130 ms/3.5 ms TR/TE, 2–3 cm slice thickness, 1.2–1.5 cm in plane spatial and 3 s temporal resolutions, 60 s acquisition window, 545 Hz bandwidth, constant flip angle through time with pyruvate 10°, and lactate 20°. Scan started 5 s following the end of the injection. Patients were asked to hold their breath as long as possible, after which they were instructed to breathe gently and resume breath holding as tolerated. Conventional proton T₁-weighted spoiled gradient-echo (TR/TE=4.3 ms/1.9 ms) images were acquired for anatomic reference. Dynamic HP ¹³C MRI datasets were processed by applying even–odd lobe phasing, B₀-shift correction, tensor-low-rank signal enhancement,²³ spectral baseline correction,²⁴ followed by a phase-sensitive peak quantification. The pyruvate-to-lactate conversion rate, k_{PL} , was evaluated using an inputless single-compartment two-site exchange model,²⁵ and the value reported was the maximum over ROI of the lesion identified on proton MRI. Total carbon signal-to-noise ratio (SNR) was reported as summed SNR of ¹³C-labeled tracers averaged over time. The image processing tools are located under—SIVIC Image Processing/Display: <https://sourceforge.net/projects/sivic>, Hyperpolarized MRI Toolbox: <https://github.com/LarsonLab/hyperpolarized-mri-toolbox>.

3.3.4 Metastatic Tumor Biopsy Acquisition & Analysis

CT-guided metastatic tumor biopsies following HP MRI acquisition were obtained in five out of the six patients enrolled in the study (Table 3.1). Tumor biopsies were obtained for both fresh frozen processing and formalin fixed paraffin embedded (FFPE) processing. FFPE tissues were used for histologic diagnosis, while frozen tissue underwent Laser Capture Microdissection for RNA-seq

profiling as previously described.⁶ Expression levels reported as $\log(1 + (\text{TPM} \times 10^6))$. Processed RNA-seq data are located in the Supplementary Materials.

Table 3.1. A summary of clinically relevant information from each patient.

Patient	Age ^a	Target metastatic site	Gleason score ^b	Serum PSA (ng/mL) ^a	Metastatic tumor biopsy pathology	Most recent prior systemic therapy
1	75	Left iliac wing	4 + 5	171.7	Adenocarcinoma + small cell neuroendocrine carcinoma (SCNC)	Enzalutamide + investigational agent
2	57	Liver	4 + 4	Baseline: 38 Follow-up: 13.4	High-grade adenocarcinoma	investigational agent
3	83	Rib	4 + 4	89.6	No biopsy performed	Enzalutamide
4	72	Right posterior ilium	4 + 5	89.2	High-grade adenocarcinoma	Docetaxel + ribociclib
5	70	Left posterior ilium	4 + 5	1482	High-grade adenocarcinoma	Docetaxel
6	82	Liver	4 + 3	1439	High-grade adenocarcinoma	Docetaxel + carboplatin

^aAt study entry. ^bAt initial diagnosis.

3.4 Results

3.4.1 Patient Characteristics

Six patients were enrolled in this pilot feasibility study. The baseline characteristics of the patients are shown in Table 3.1. All patients had progressive mCRPC at study entry. Five of the patients underwent CT-guided metastatic tumor biopsy of the target lesions following completion of baseline ¹³C-pyruvate MRI. No adverse events were reported throughout this study.

3.4.2 HP ¹³C-pyruvate MRI Detects High k_{PL} in Bone & Liver Metastases

The rate of conversion of pyruvate to lactate (k_{PL}) from target lesions in each patient is listed in Table 3.2. There was high k_{PL} in both bone and liver metastases, with mean k_{PL} of $(0.020 \pm 0.006 \text{ s}^{-1})$ and $(0.026 \pm 0.000 \text{ s}^{-1})$, respectively.²⁶ Regions of high k_{PL} were consistent with CT and MRI radiographic findings of metastatic disease presence, as shown in the representative k_{PL} image overlays for the target lesions (Figure 3.2a, Supplementary Figures 3.1–4).

Table 3.2. Findings from HP ^{13}C MRI including k_{PL} and RNA expression of key genes.

Patient	k_{PL} of target lesion (s^{-1})	Ldha/Pdha1 expression (in log)	SNR tCarb
1	0.013	15.4/12.3	290.3 ± 248.5
2	Baseline: 0.026 Follow-up ^a : 0.015	16.2/13.8	Baseline: 89.7 ± 40.9 Follow-up ^a : 77.7
3	0.017	Not acquired	131.4 ± 10.2
4	0.026	14.7/11.6	27.4 ± 9.9
5	0.023	16.4/12.6	19.5 ± 3.6
6	0.025	15.6/13.7	88.2 ± 26.1

^aFollow-up was 2 months after initiation of carboplatin + docetaxel.

Abbreviations: SNR tcarb: summed SNR of ^{13}C -labeled tracers averaged over time.

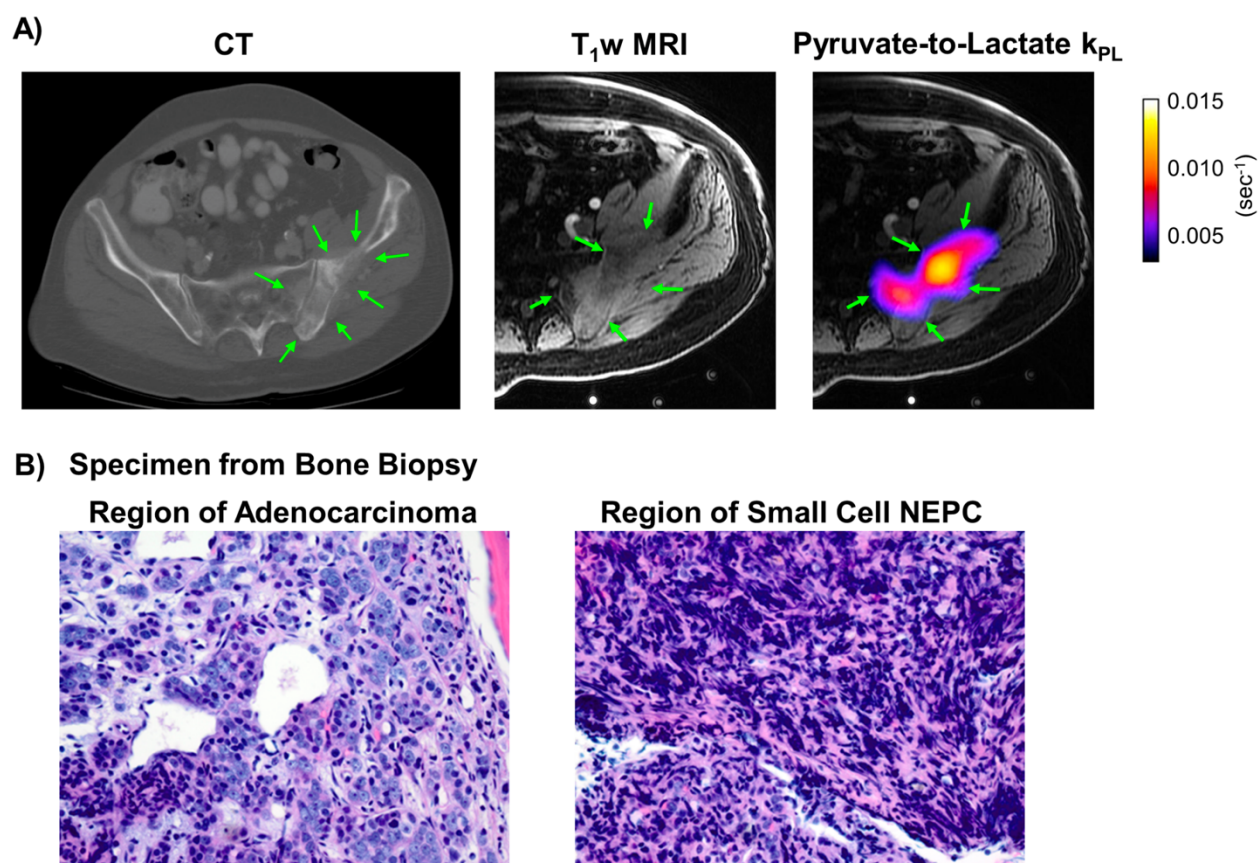


Figure 3.2. (A) Patient 1 (75 years old) was diagnosed with metastatic castration-resistant prostate cancer with several large osteoblastic lesions throughout the left hemipelvis and involving left femur. CT identified a relatively osteolytic lesion in left ilium (green arrows), measuring 9.9×4.1 cm. The lesion was infiltrative, causing destruction of the bone cortex and extension into the surrounding soft tissues. T₁-weighted (T₁w) spoiled gradient-echo MRI was used to target the same lesion observed on CT for the HP ^{13}C MR acquisition. Regions of high pyruvate-to-lactate conversion rate (k_{PL}) correlated with the osseous lesion on CT and hypointensity on T₁w MRI. k_{PL} was estimated 0.013 (s^{-1}). (B) The paired bone biopsy demonstrated discrete regions of adenocarcinoma and treatment-emergent small cell neuroendocrine differentiation.

The liver mass of patient six showed considerable intratumoral heterogeneity (Supplementary Figure 3.4b). Maximum $k_{PL} = 0.025 \text{ s}^{-1}$ was found in viable tumor, whereas $k_{PL} = 0.004 \text{ s}^{-1}$ was observed in a necrotic-appearing region identified both on CT and the delayed phase of contrast T_1 -weighted images.

Table 3.2 also summarizes the total carbon SNR for each study. The total carbon SNR was 117 ± 126 in bone metastases ($N = 4$), and 85 ± 7 between liver involvements ($N = 2$). In general, the SNR in all cases was adequate for reliable k_{PL} fitting (standard error metric $\sigma_{k_{PL}} = 0.005 \pm 0.003$).²⁷

In all five patients with paired ^{13}C -pyruvate MRI and CT-guided biopsy of the target lesions, the histological evidence of metastatic prostate cancer was detected. In four of the five cases, the histology demonstrated poorly differentiated adenocarcinoma. In one patient (Patient 1), the paired metastatic tumor biopsy demonstrated discrete regions of adenocarcinoma and treatment-emergent small cell neuroendocrine differentiation (Figure 3.2b).⁶

Higher levels of gene expression of the lactate dehydrogenase isoform A (Ldha, 15.7 ± 0.7) relative to the dominant isoform of pyruvate dehydrogenase (Pdha1, 12.8 ± 0.9) were detected on RNA-seq of the target metastatic biopsies (Table 3.2), consistent with enhanced aerobic glycolysis detected in the rate of conversion of pyruvate to lactate on HP ^{13}C MRI. No significant difference in Ldha or Pdha1 expression was observed in the patients imaged in this study compared with a previously published cohort of metastases from 200 men with mCRPC (Ldha: 15.1 ± 1.1 , $p > 0.17$; Pdha1: 12.0 ± 0.9 , $p > 0.06$, Wilcoxon ranked sum test).⁶

3.4.3 HP ¹³C MRI Detected a Metabolic Rate Decrease in a Metastasis Following Chemotherapy

Patient 2 had mCRPC with liver metastases and low serum PSA level. Carboplatin + docetaxel chemotherapy was started 24 days after the baseline HP ¹³C MRI study (Figure 3.3c). Follow-up HP MRI study 62 days after the initiation of treatment demonstrated a 42% decrease in pyruvate-to-lactate conversion rate k_{PL} , from 0.026 to 0.015 s⁻¹, in the target liver lesion (Figure 3.3a). This was accompanied by interval decrease of the lesion size (Figure 3.3b, 19.3–11.8 mm, 39%) based on RECIST 1.1 criteria, along with serum PSA decline of >50% from baseline (38–13.4 ng/ml), consistent with systemic treatment response.

3.5 Discussion

This work reports the results of the first-ever pilot imaging study of prostate cancer metastases using HP ¹³C-pyruvate MRI. This study demonstrates the feasibility of detecting real-time metabolic activity of metastases and capture therapeutic response with this emerging stable-isotope molecular imaging method. Correlation with paired metastatic biopsy demonstrated high-grade prostate adenocarcinoma, including in one case, evidence of neuroendocrine differentiation.

The high pyruvate-to-lactate conversion rate, k_{PL} , via upregulated LDH activity in cancer, known as Warburg effect, reflects cancer aggressiveness, and decrease in k_{PL} can reflect therapeutic response.^{14,20} Overall, the pyruvate-to-lactate conversion rate k_{PL} found in bone (0.020 ± 0.006 s⁻¹) and liver (0.026 ± 0.000 s⁻¹) lesions was either higher than or comparable with that of high-grade primary prostate cancer (0.013 ± 0.003 s⁻¹) in a cohort imaged prior to radical prostatectomy with whole mount section pathologic correlation.²⁶ These high k_{PL} values were correlated with the metastatic biopsy

findings of high-grade adenocarcinoma or mixed high-grade adenocarcinoma and small cell neuroendocrine phenotypes in the patients studied in this report.

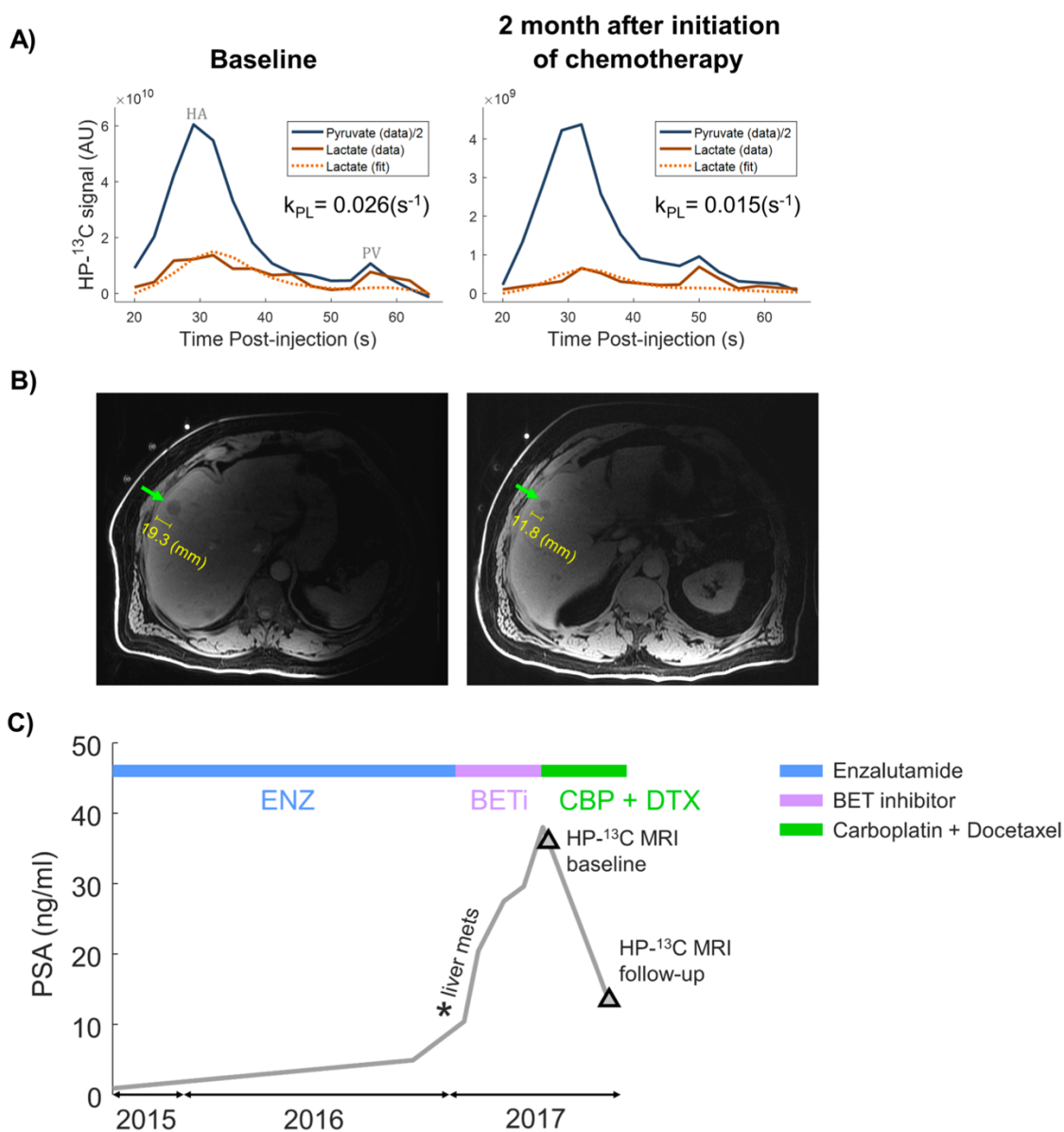


Figure 3.3. Patient 2 (57 years old) was diagnosed with CRPC that metastasized to liver. The patient was previously treated with enzalutamide and an investigational agent (BET inhibitor, phase I) with clinical progression. Chemotherapy of carboplatin and docetaxel started ~1 month post baseline HP ^{13}C scan, and follow-up was 2 months after initiation of therapy. **(A)** A decrease in pyruvate-to-lactate conversion rate k_{PL} was observed from 0.026 to 0.015 (s^{-1}) after 2 months of chemotherapy. Note the increase in pyruvate and lactate at 50–60 s post injection. Most likely this is predominately due to vascular contributions coming from intestines. **(B)** Follow-up 2 months after initiation of therapy found a decrease in lesion size (19.3–11.8 mm) indicating therapeutic response based on RECIST criteria. **(C)** In addition, serum PSA decreased from 38–13.4 ng/ml also indicating therapeutic response. HA arterial phase, PV portal venous phase.

Elevated *Ldha* expression in prostate cancer is known to be associated with aggressive phenotypes and resistant to therapy.²⁸⁻³⁰ The high *Ldha* expression relative to *Pdha1* in this study was consistent with a larger published mCRPC cohort,⁶ reflective of enhanced aerobic glycolysis, whereas in normal prostate epithelial cells the glucose metabolism favors oxidative phosphorylation, and *Pdha1* expression should predominate (Figure 3.1). This suggested that the metabolic features observed in this study using HP ¹³C-pyruvate MRI could potentially serve as a representative cross-section of a much larger patient population with different metastatic sites and types of cell morphology.

A previous study in primary prostate cancer indicated that k_{PL} reflected early response and resistance to androgen pathway inhibition.²⁰ In this communication we observed a correlation between decreased k_{PL} and clinical response to the combination of platinum plus taxane chemotherapy in a patient with mCRPC. Although preliminary, these findings suggest that imaging metabolic signatures using HP ¹³C-pyruvate MR could potentially report responses to a broader range of oncogenic pathway inhibition and drug targets, and may be less susceptible to the upregulation of membrane protein expression secondary to ADT.^{31,32} These data suggest that the prospective evaluation of HP ¹³C-pyruvate as a response biomarker in mCRPC patients treated with AR-targeting and cytotoxic chemotherapy is warranted.

Spatially, regions of high k_{PL} showed good alignment with radiographic findings of metastases using bone scan, CT, and proton MRI. Temporally, the time-to-peak of pyruvate bolus was 29 ± 3 s in pelvic bone cases, 23 s in the rib case, 34 ± 4 s among the liver cases. The bolus delivery timing was generally consistent with contrast CT/MRI,³³ and are deemed reasonable in light of hemodynamic variations between subjects, and also the vitals of individual subject at the time of the scan. The inputless k_{PL} model applied in this study is relatively immune to variations in bolus characteristics.²⁵

Differential k_{PL} was observed between viable and necrotic-appearing regions of Patient 6's liver lesion (Supplementary Figure 3.4b). These findings are consistent with other emerging reports of

intra- and inter-tumoral heterogeneity in mCRPC³⁴ and highlight the potential utility of this imaging tool to clarify tumor biology with real-time metabolic monitoring.³⁴⁻³⁷ The k_{PL} heterogeneity between metastatic sites/individual patients and its biological underpinning calls for future investigation.

This study also demonstrated that this technology can provide quantitative metrics of the delivery/uptake of the injected hyperpolarized carbon isotope by measuring the total carbon SNR summing the ^{13}C signal observed from the hyperpolarized pyruvate bolus and downstream metabolic products. Conceptually similar to SUV in PET, total carbon SNR is a metric of delivery and uptake. Of the pelvic bone involvements, patient 1, whose lesion appeared relatively more lytic on CT (Figure 3.2a), had higher mean total $\text{SNR}_{\text{Patient 1}} = 290$ versus the other two cases ($\text{SNR}_{\text{Patient 4}} = 27.4$, $\text{SNR}_{\text{Patient 5}} = 19.5$) with more sclerotic appearances (Supplementary Figures 3.1 and 3.3). This presents an intriguing concordance with PET literature in which osteolytic lesions have shown higher FDG uptake compared with osteoblastic ones³⁸⁻⁴⁰ and glucose metabolism is known to be differently regulated in sclerotic versus lytic diseases.⁴¹

Several key limitations should be identified for this pilot study. The correlation between metabolic biomarker k_{PL} and total carbon SNR is yet to be elucidated in the mCRPC setting. In addition, the test-retest repeatability data are also needed moving forward. While the total carbon SNR reports tracer pharmacokinetics at each metastatic site, its quantitative accuracy can be further enhanced using automatic B_1 calibration and correction for QC parameters. This study utilized a 2D single-slice imaging strategy. Future advancement in array receiver hardware⁴² and MR acquisition sequences^{21,43} will enable full 3D coverage of the abdomen/pelvis and seamless integration with standard-of-care restaging scans. Dissemination of this technology, in terms of infrastructure and instruments, requires a clinical ^{13}C polarizer and specialized MRI hardware. The on-site pharmaceutical manufacturing follows the same standard as PET, allowing for shared facility.¹⁴ These capabilities can readily be instated in high-volume tertiary centers who manages the majority of the advanced prostate

cancer cohort. Overall, future developments are warranted to address the technical needs including hardware, image acquisition and quantitative analyses, and the clinical inquiries deserve to be powered by a larger cohort study.

These preliminary results highlight the future need to metabolically characterize lymphadenopathy using HP ^{13}C -pyruvate MRI, as management of nodal disease could be essential in the realm of biochemically recurrent and oligometastatic PCa.⁴⁴⁻⁴⁷ For these cohorts of patients, opportunities for curative treatment are more available, and clinical outcomes are generally better than those with bone involvement and thus higher disease burden. Such future studies could be enabled by the aforementioned technical advancements to achieve higher resolution and sensitivity, and new pharmacy QC procedures that reduce HP ^{13}C -pyruvate time-to-injection and thereby improving SNR.¹⁴

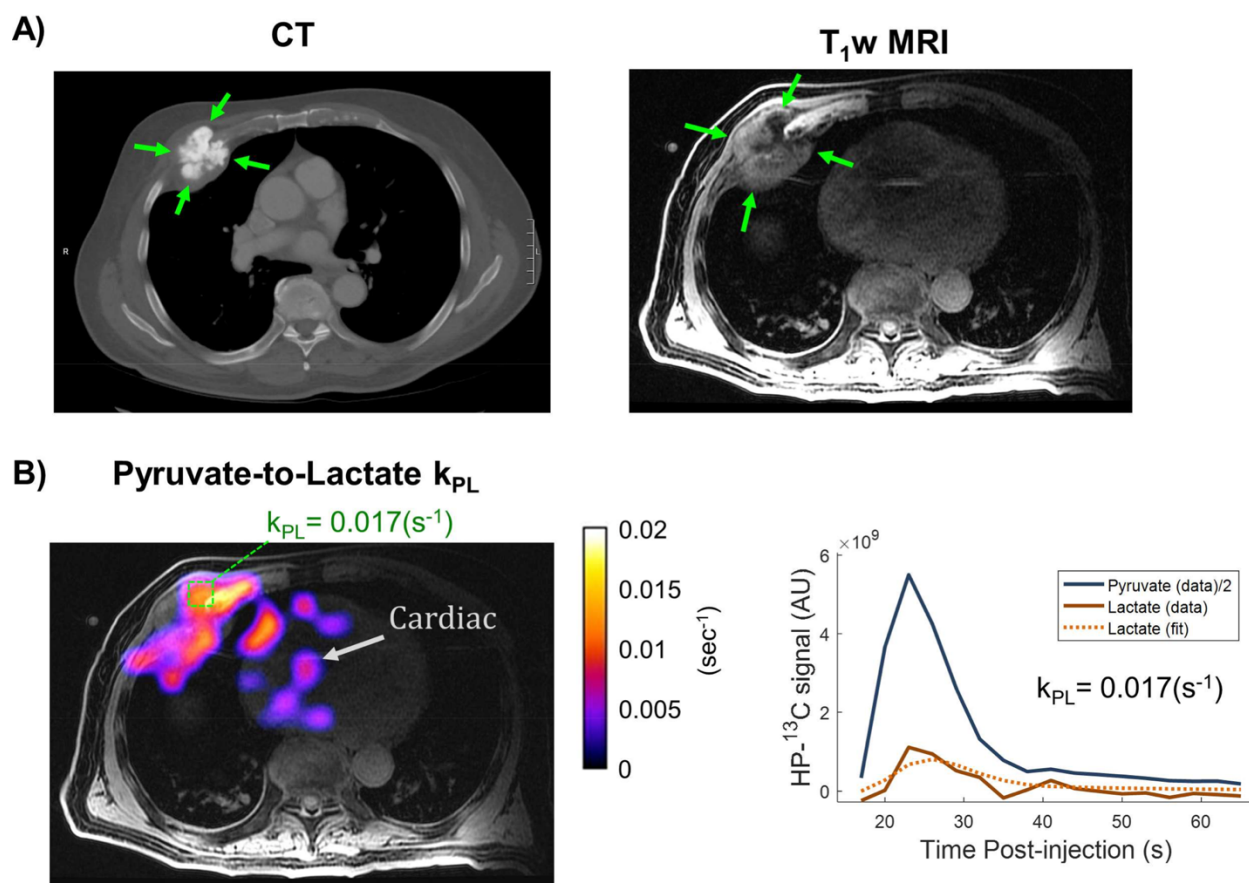
3.6 Conclusions

This pilot study evaluated the safety and feasibility to conduct HP ^{13}C MRI studies of patients with metastatic prostate cancer to the skeleton and viscera, which represents the most advanced and lethal form of the disease. Methods were examined and established for instrumentation setup, pharmacy manufacturing, image acquisition, and quantitative analysis. Safety was demonstrated and highly upregulated pyruvate-to-lactate conversion k_{PL} was observed on aggressive osseous and hepatic metastases. Interval decrease of k_{PL} was found for one patient receiving combination chemotherapy, in concordance with conventional clinical biochemical and imaging biomarkers. These findings warrant further development and investigation of HP ^{13}C -pyruvate MRI in a larger prospective group of men with metastatic CRPC.

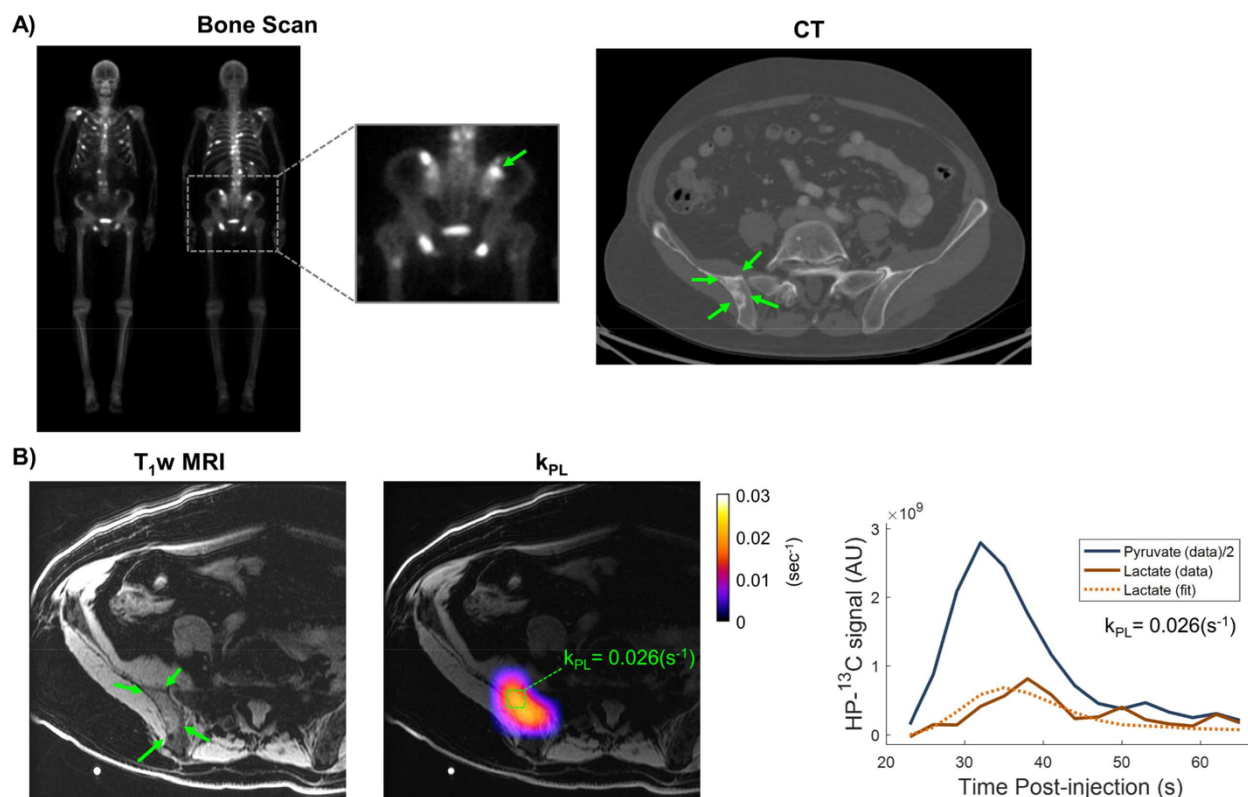
3.7 Acknowledgements

This work was supported by grants from the NIH (R01CA183071, U01EB026412, R01CA215694, R01CA166655, U01CA232320, and P41EB013598).

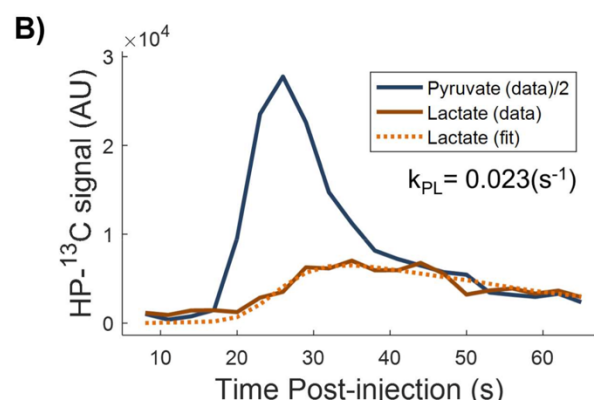
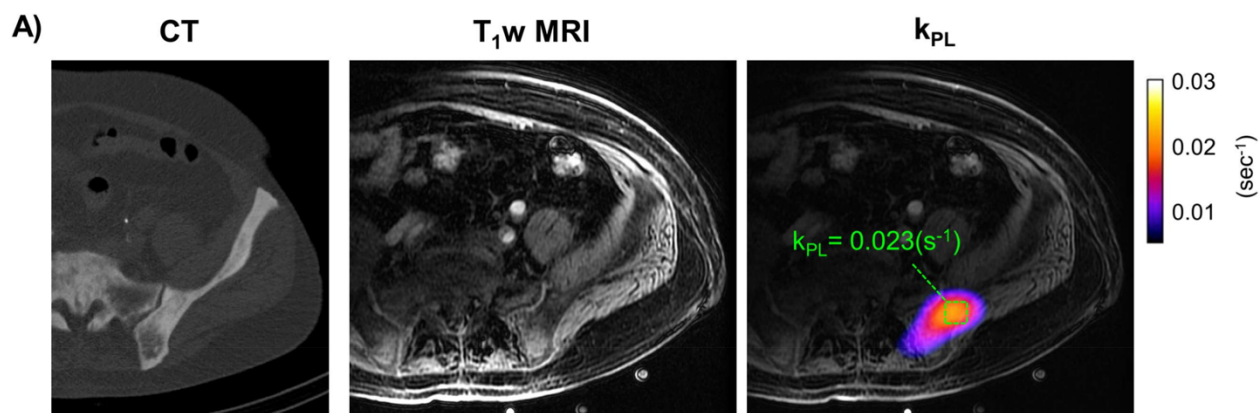
3.8 Supporting Information



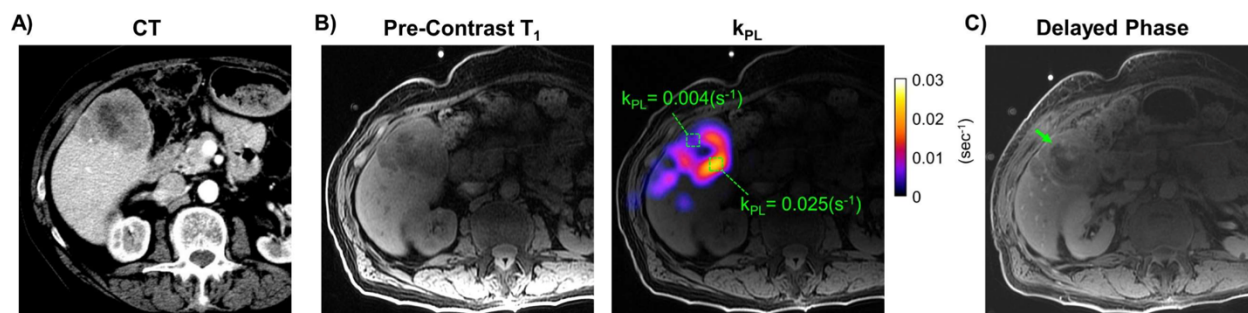
Supporting Information Figure S3.1. Patient 3 was 83-year-old who was diagnosed with Gleason 4+4 prostate cancer with progressive mCRPC status post multiple prior lines of therapy (Table 3.1). **(A)** CT images identified an osseous lesion on right lateral 4th rib, measuring $6.5 \times 4.8\text{cm}$, with soft tissue components. Center of the lesion appeared sclerotic on CT and hypoenhancing on T₁w MRI. **(B)** k_{PL} of 0.017 s^{-1} was measured in the rib lesion. The tumor mass extended posteriorly along the 4th rib, spatially agreeing with high k_{PL} regions.



Supporting Information Figure S3.2. Patient 4 was a 72-year-old individual with Gleason 4+5, cT1c prostate adenocarcinoma at diagnosis. **(A)** A bone scan revealed extensive disease in rib cage, spine and pelvis. CT identified an osteoblastic lesion at right iliac crest (2.3×1.4 cm) with some cortical erosion. **(B)** k_{PL} in the osseous lesion was calculated 0.026 s^{-1} . CT-guided bone biopsy confirmed adenocarcinoma consistent with mCRPC, and PSA was 89.2 ng/ml at the time of HP study.



Supporting Information Figure S3.3. Patient 5 was 70-year-old diagnosed with Gleason 4+5 prostate cancer. Bone metastases involving the ribs, spine and pelvis was found at the time of diagnosis. Restaging bone scan and CT identified extensive sclerotic metastases throughout axial into the appendicular skeleton, involving essentially all visualized bone in the chest, abdomen and pelvis. **(A)** HP ¹³C study targeted a diffuse sclerotic lesion adjoining the left iliac spine. Deep-bone biopsy found adenocarcinoma consistent with mCRPC. **(B)** k_{PL} was measured 0.023 s^{-1} at the lesion, and PSA was 1482 (ng/ml) at the time of the exam.



Supporting Information Figure S3.4. Patient 6 was an 83-year-old patient with mCRPC including large liver metastases. **(A)** CT identified a large lesion in segment 5 measuring $5.5 \times 5.1 \text{ cm}$, with centrally hypoenhancing/necrotic-appearing region measuring $2.8 \times 2.3 \text{ cm}$. The HP ¹³C study **(B)** estimated k_{PL} at 0.025 s^{-1} . Note region of low k_{PL} in HP MRI correlated with the necrotic-appearing region in the **(C)** delayed phase of contrast imaging. Fine needle aspiration to the lesion of interest found adenocarcinoma consistent with mCRPC.

3.9 References

1. American Cancer Society. Cancer Facts and Figures, 2019. Published online 2019.
2. Padhani AR, Lecouvet FE, Tunariu N, et al. Rationale for Modernising Imaging in Advanced Prostate Cancer. *Eur Urol Focus*. 2017;3(2-3):223-239. doi:10.1016/j.euf.2016.06.018
3. James ND, Spears MR, Clarke NW, et al. Survival with Newly Diagnosed Metastatic Prostate Cancer in the “Docetaxel Era”: Data from 917 Patients in the Control Arm of the STAMPEDE Trial (MRC PR08, CRUK/06/019). *Eur Urol*. 2015;67(6):1028-1038. doi:10.1016/j.eururo.2014.09.032
4. Goodman OB, Flaig TW, Molina A, et al. Exploratory analysis of the visceral disease subgroup in a phase III study of abiraterone acetate in metastatic castration-resistant prostate cancer. *Prostate Cancer Prostatic Dis*. 2014;17(1):34-39. doi:10.1038/pcan.2013.41
5. Pezaro CJ, Omlin A, Lorente D, et al. Visceral Disease in Castration-resistant Prostate Cancer. *Eur Urol*. 2014;65(2):270-273. doi:10.1016/j.eururo.2013.10.055
6. Aggarwal R, Huang J, Alumkal JJ, et al. Clinical and Genomic Characterization of Treatment-Emergent Small-Cell Neuroendocrine Prostate Cancer: A Multi-institutional Prospective Study. *J Clin Oncol*. 2018;36(24):2492-2503. doi:10.1200/JCO.2017.77.6880
7. Scher HI, Halabi S, Tannock I, et al. Design and End Points of Clinical Trials for Patients With Progressive Prostate Cancer and Castrate Levels of Testosterone: Recommendations of the Prostate Cancer Clinical Trials Working Group. *J Clin Oncol*. 2008;26(7):1148-1159. doi:10.1200/JCO.2007.12.4487
8. O’Sullivan GJ. Imaging of bone metastasis: An update. *World J Radiol*. 2015;7(8):202. doi:10.4329/wjr.v7.i8.202
9. Hope TA, Truillet C, Ehman EC, et al. 68 Ga-PSMA-11 PET Imaging of Response to Androgen Receptor Inhibition: First Human Experience. *J Nucl Med*. 2017;58(1):81-84.

doi:10.2967/jnumed.116.181800

10. Seitz AK, Rauscher I, Haller B, et al. Preliminary results on response assessment using ⁶⁸Ga-HBED-CC-PSMA PET/CT in patients with metastatic prostate cancer undergoing docetaxel chemotherapy. *Eur J Nucl Med Mol Imaging*. 2018;45(4):602-612. doi:10.1007/s00259-017-3887-x
11. Nelson SJ, Kurhanewicz J, Vigneron DB, et al. Metabolic Imaging of Patients with Prostate Cancer Using Hyperpolarized [1-¹³C]Pyruvate. *Sci Transl Med*. 2013;5(198):198ra108. doi:10.1126/scitranslmed.3006070
12. Ardenkjær-Larsen JH, Golman K, Gram A, et al. Increase of signal-to-noise of more than 10,000 times in liquid state NMR. *Discov Med*. 2003;100(18):10158-10163.
13. Albers MJ, Bok R, Chen AP, et al. Hyperpolarized ¹³C lactate, pyruvate, and alanine: Noninvasive biomarkers for prostate cancer detection and grading. *Cancer Res*. 2008;68(20):8607-8615. doi:10.1158/0008-5472.CAN-08-0749
14. Kurhanewicz J, Vigneron DB, Ardenkjaer-Larsen JH, et al. Hyperpolarized ¹³C MRI: Path to Clinical Translation in Oncology. *Neoplasia (United States)*. 2019;21(1):1-16. doi:10.1016/j.neo.2018.09.006
15. Hirschhaeuser F, Sattler UGA, Mueller-Klieser W. Lactate: A Metabolic Key Player in Cancer. *Cancer Res*. 2011;71(22):6921-6925. doi:10.1158/0008-5472.CAN-11-1457
16. Kim J, Dang C V. Cancer's Molecular Sweet Tooth and the Warburg Effect: Figure 1. *Cancer Res*. 2006;66(18):8927-8930. doi:10.1158/0008-5472.CAN-06-1501
17. Gonzalez PS, O'Prey J, Cardaci S, et al. Mannose impairs tumour growth and enhances chemotherapy. *Nature*. 2018;563(7733):719-723. doi:10.1038/s41586-018-0729-3
18. Zhou M, Zhao Y, Ding Y, et al. Warburg effect in chemosensitivity: Targeting lactate dehydrogenase-A re-sensitizes Taxol-resistant cancer cells to Taxol. *Mol Cancer*. 2010;9(1):33.

- doi:10.1186/1476-4598-9-33
19. Timm KN, Kennedy BWC, Brindle KM. Imaging Tumor Metabolism to Assess Disease Progression and Treatment Response. *Clin Cancer Res.* 2016;22(21):5196-5203.
doi:10.1158/1078-0432.CCR-16-0159
 20. Aggarwal R, Vigneron DB, Kurhanewicz J. Hyperpolarized 1-[13C]-Pyruvate Magnetic Resonance Imaging Detects an Early Metabolic Response to Androgen Ablation Therapy in Prostate Cancer. *Eur Urol.* 2017;72(6):1028-1029. doi:10.1016/j.eururo.2017.07.022
 21. Chen HY, Larson PEZ, Gordon JW, et al. Technique development of 3D dynamic CS-EPSI for hyperpolarized 13 C pyruvate MR molecular imaging of human prostate cancer. *Magn Reson Med.* 2018;80(5):2062-2072. doi:10.1002/mrm.27179
 22. Park I, Larson PEZ, Gordon JW, et al. Development of methods and feasibility of using hyperpolarized carbon-13 imaging data for evaluating brain metabolism in patient studies. *Magn Reson Med.* 2018;80(3):864-873. doi:10.1002/mrm.27077
 23. Brender JR, Kishimoto S, Merkle H, et al. PET by MRI: Glucose Imaging by 13C-MRS without Dynamic Nuclear Polarization by Noise Suppression through Tensor Decomposition Rank Reduction. *bioRxiv.* Published online 2018:265793.
 24. Nelson SJ, Brown TR. The accuracy of quantification from 1D NMR spectra using the PIQABLE algorithm. *J Magn Reson.* 1989;84(1):95-109. doi:10.1016/0022-2364(89)90008-5
 25. Larson PEZ, Chen HY, Gordon JW, et al. Investigation of analysis methods for hyperpolarized 13C-pyruvate metabolic MRI in prostate cancer patients. *NMR Biomed.* 2018;31(11):e3997. doi:10.1002/nbm.3997
 26. Korn N, Larson P, Chen H-Y, et al. The Rate of Hyperpolarized [1-13C] Pyruvate to [1-13C] Lactate Conversion Distinguishes High-Grade Prostate Cancer from Low-Grade Prostate Cancer and Normal Peripheral Zone Tissue in Patients. In: *Proceedings of the 26th Annual*

- Meeting of ISMRM 2018*. The International Society for Magnetic Resonance in Medicine; 2018.
27. Mammoli D, Carvajal L, Slater JB, et al. Kinetic Modeling of Hyperpolarized Carbon-13 Pyruvate Metabolism in the Human Brain. *IEEE Trans Med Imaging*. 2020;39(2):320-327. doi:10.1109/TMI.2019.2926437
 28. Bok R, Lee J, Sriram R, et al. The Role of Lactate Metabolism in Prostate Cancer Progression and Metastases Revealed by Dual-Agent Hyperpolarized ¹³C MRSI. *Cancers (Basel)*. 2019;11(2):257. doi:10.3390/cancers11020257
 29. Hiew K, Hart CA, Ali A, et al. Primary Mutational Landscape Linked with Pre-Docetaxel Lactate Dehydrogenase Levels Predicts Docetaxel Response in Metastatic Castrate-Resistant Prostate Cancer. *Eur Urol Focus*. 2019;5(5):831-841. doi:10.1016/j.euf.2018.04.006
 30. Koukourakis MI, Giatromanolaki A, Panteliadou M, et al. Lactate dehydrogenase 5 isoenzyme overexpression defines resistance of prostate cancer to radiotherapy. *Br J Cancer*. 2014;110(9):2217-2223. doi:10.1038/bjc.2014.158
 31. Aggarwal R, Wei X, Kim W, et al. Heterogeneous Flare in Prostate-specific Membrane Antigen Positron Emission Tomography Tracer Uptake with Initiation of Androgen Pathway Blockade in Metastatic Prostate Cancer. *Eur Urol Oncol*. 2018;1(1):78-82. doi:10.1016/j.euo.2018.03.010
 32. Schwarzenboeck SM, Rauscher I, Bluemel C, et al. PSMA Ligands for PET Imaging of Prostate Cancer. *J Nucl Med*. 2017;58(10):1545-1552. doi:10.2967/jnumed.117.191031
 33. Heiken JP, Bae KT. Contrast Medium Administration and Scan Timing for MDCT. In: *Multidetector-Row Computed Tomography*. Springer-Verlag; :13-20. doi:10.1007/88-470-0363-6_3
 34. Davnall F, Yip CSP, Ljungqvist G, et al. Assessment of tumor heterogeneity: an emerging imaging tool for clinical practice? *Insights Imaging*. 2012;3(6):573-589. doi:10.1007/s13244-012-0196-6

35. Hockel M, Vaupel P. Tumor Hypoxia: Definitions and Current Clinical, Biologic, and Molecular Aspects. *JNCI J Natl Cancer Inst.* 2001;93(4):266-276. doi:10.1093/jnci/93.4.266
36. Beltran H, Rickman DS, Park K, et al. Molecular Characterization of Neuroendocrine Prostate Cancer and Identification of New Drug Targets. *Cancer Discov.* 2011;1(6):487-495. doi:10.1158/2159-8290.CD-11-0130
37. Lalonde E, Ishkanian AS, Sykes J, et al. Tumour genomic and microenvironmental heterogeneity for integrated prediction of 5-year biochemical recurrence of prostate cancer: a retrospective cohort study. *Lancet Oncol.* 2014;15(13):1521-1532. doi:10.1016/S1470-2045(14)71021-6
38. Beheshti M, Vali R, Waldenberger P, et al. Detection of bone metastases in patients with prostate cancer by 18F fluorocholine and 18F fluoride PET–CT: a comparative study. *Eur J Nucl Med Mol Imaging.* 2008;35(10):1766-1774. doi:10.1007/s00259-008-0788-z
39. Nakai T, Okuyama C, Kubota T, et al. Pitfalls of FDG-PET for the diagnosis of osteoblastic bone metastases in patients with breast cancer. *Eur J Nucl Med Mol Imaging.* 2005;32(11):1253-1258. doi:10.1007/s00259-005-1842-8
40. Cook GJ, Houston S, Rubens R, Maisey MN, Fogelman I. Detection of bone metastases in breast cancer by 18FDG PET: differing metabolic activity in osteoblastic and osteolytic lesions. *J Clin Oncol.* 1998;16(10):3375-3379. doi:10.1200/JCO.1998.16.10.3375
41. Todenhöfer T, Stenzl A, Hofbauer LC, Rachner TD. Targeting Bone Metabolism in Patients with Advanced Prostate Cancer: Current Options and Controversies. *Int J Endocrinol.* 2015;2015:1-9. doi:10.1155/2015/838202
42. Autry AW, Gordon JW, Carvajal L, et al. Comparison between 8- and 32-channel phased-array receive coils for in vivo hyperpolarized ¹³C imaging of the human brain. *Magn Reson Med.* 2019;82(2):833-841. doi:10.1002/mrm.27743

43. Gordon JW, Chen HY, Autry A, et al. Translation of Carbon-13 EPI for hyperpolarized MR molecular imaging of prostate and brain cancer patients. *Magn Reson Med*. 2019;81(4):2702-2709. doi:10.1002/mrm.27549
44. Rigatti P, Suardi N, Briganti A, et al. Pelvic/Retroperitoneal Salvage Lymph Node Dissection for Patients Treated With Radical Prostatectomy With Biochemical Recurrence and Nodal Recurrence Detected by [11C]Choline Positron Emission Tomography/Computed Tomography. *Eur Urol*. 2011;60(5):935-943. doi:10.1016/j.eururo.2011.07.060
45. Ost P, Reynders D, Decaestecker K, et al. Surveillance or Metastasis-Directed Therapy for Oligometastatic Prostate Cancer Recurrence: A Prospective, Randomized, Multicenter Phase II Trial. *J Clin Oncol*. 2018;36(5):446-453. doi:10.1200/JCO.2017.75.4853
46. Foster CC, Weichselbaum RR, Pitroda SP. Oligometastatic prostate cancer: Reality or figment of imagination? *Cancer*. 2019;125(3):340-352. doi:10.1002/cncr.31860
47. Cornford P, Bellmunt J, Bolla M, et al. EAU-ESTRO-SIOG Guidelines on Prostate Cancer. Part II: Treatment of Relapsing, Metastatic, and Castration-Resistant Prostate Cancer. *Eur Urol*. 2017;71(4):630-642. doi:10.1016/j.eururo.2016.08.002

Chapter 4

Specialized Computational Methods for Denoising, B_1 Correction, & Kinetic Modeling in Hyperpolarized ^{13}C MR EPSI Studies of Liver Tumors

Lee PM, Chen HY, Gordon JW, Zhu Z, Larson PEZ, Dwork N, Van Criekinge M, Carvajal L, Ohliger MA, Wang ZJ, Xu D, Kurhanewicz J, Bok RA, Aggarwal R, Munster PN, and Vigneron DB. Specialized computational methods for denoising, B_1 correction, and kinetic modeling in hyperpolarized ^{13}C MR EPSI studies of liver tumors. *Magnetic Resonance in Medicine*. June 2021. DOI: 10.1002/mrm.28901.

4.1 Abstract

4.1.1 Purpose

To develop a novel post-processing pipeline for hyperpolarized (HP) ^{13}C MRSI that integrates tensor denoising and B_1^+ correction to measure pyruvate-to-lactate conversion rates (k_{PL}) in patients with liver tumors.

4.1.2 Methods

Seven HP ^{13}C MR scans of progressing liver tumors were acquired using a custom ^{13}C surface transmit/receive coil and the EPSI data analysis included B_0 correction, tensor rank truncation, and zero- and first-order phase corrections to recover metabolite signals that would otherwise be obscured by spectral noise as well as a correction for inhomogeneous transmit (B_1^+) using a B_1^+ map aligned to the coil position for each patient scan. Processed HP data and corrected flip angles were analyzed with an inputless two-site exchange model to calculate k_{PL} .

4.1.3 Results

Denoising averages SNR increases of pyruvate, lactate, and alanine were 37.4, 34.0, and 20.1-fold respectively, with lactate and alanine dynamics most noticeably recovered and better defined. In agreement with Monte Carlo simulations, over-flipped regions underestimated k_{PL} and under-flipped regions overestimated k_{PL} . B_1^+ correction addressed this issue.

4.1.4 Conclusions

The new HP ^{13}C EPSI post-processing pipeline integrated tensor denoising and B_1^+ correction to measure k_{PL} in patients with liver tumors. These technical developments not only recovered metabolite

signals in voxels that did not receive the prescribed flip angle, but also increased the extent and accuracy of k_{PL} estimations throughout the tumor and adjacent regions including normal-appearing tissue and additional lesions.

4.2 Introduction

Hyperpolarized (HP) ^{13}C MR spectroscopic imaging (MRSI) using dissolution dynamic nuclear polarization techniques¹ enables quantitative imaging of enzyme-catalyzed metabolism in humans and has been applied to study in vivo metabolism of cardiac diseases,^{2,3} breast cancer,^{4,5} brain cancer,⁶⁻⁹ and prostate cancer.¹⁰⁻¹² In this metabolic imaging approach HP ^{13}C -pyruvate can be safely injected into human subjects while retaining an observable signal that is 10,000+ fold higher than thermal values at clinical field strengths.¹³ Analysis and kinetic modeling can quantify enzymatic conversion rates in key metabolic pathways, most notably the pyruvate-to-lactate conversion through lactate dehydrogenase (LDH).¹³⁻¹⁵ The measured rate constant, k_{PL} , is a potential biomarker that is greatly increased in cancer^{13,16} and has been shown to reflect treatment response in animal models¹⁷⁻²⁰ and in humans.^{10,12}

Although prior studies demonstrated the ability to detect increased pyruvate-to-lactate conversion in high grade cancers and reduced conversion following successful therapy,^{5,7,10,12,17-20} current methods are often sub-optimal with several technical challenges yet to be fully overcome.¹³ Background noise in HP spectra can obscure downstream metabolite signals limiting the achievable spatial resolution and reducing the accuracy of k_{PL} estimations in these cases. Surface transmit/receive (T/R) coils can improve SNR limitations increasing the sensitivity in these experiments, but they produce an inhomogeneous transmit (B_1^+) profile. This results in spatially varying flip angles that could bias quantification.^{14,21}

The goal of this project was to develop a novel post-processing pipeline to improve spectral SNR using tensor rank truncation denoising and to correct k_{PL} data for B_1^+ variations in human studies of metastatic and primary cancers in the liver. This was designed to enable quantitative HP ^{13}C -pyruvate MR to address an important unmet clinical need for measuring cancer metabolism and response to therapy in liver tumors.

4.3 Methods

4.3.1 Patients

Seven MRI exams including a hyperpolarized ^{13}C MR acquisition were performed on a clinical 3 T MRI scanner with multi-nuclear capability from three patients enrolled in a hyperpolarized MRI study of metastatic cancer. These seven exams are tabulated in Table 4.1. The human studies were approved by an Institutional Review Board (IRB) requiring informed consent and followed Food and Drug Administration Investigational New Drug application (FDA IND)-approved protocols.

4.3.2 HP ^{13}C Patient MRI Scans

The studies were conducted on a clinical 3 T MRI (GE Healthcare, Milwaukee, WI) with a custom figure-8 surface coil (shown in Figure 4.1) for ^{13}C transmit and receive and either a commercial 32-channel torso array or a 16-channel flex array for ^1H receive. As seen in Figure 4.1A, the figure-8 coil measured 17 cm by 10 cm. Vitamin E capsules were embedded in the coil at its corners and along one central axis, and thus facilitated coil positioning as they were visible on T_1 -weighted images. A ^{13}C -enriched urea phantom was also visible on T_1 -weighted images and was used for transmit power calibration. As seen in Figure 4.1B, both vitamin E capsules and the urea phantom, highlighted by yellow dots, were used during the initial B_1^+ map acquisition and subsequent alignment. Details for

the B_1^+ map and correction are presented in section 4.3.5. Figure 4.1C-D show an example coil-placement for a patient scan, here with the figure-8 coil and a 32-channel ^1H torso array.

Table 4.1. Selected voxels from seven patient scans showing the optimized tensor ranks (with dimensions: frequency, x, y, and time), improvements in SNR after denoising, the flip correction scaling factor (over-flipped: > 1 , under-flipped: < 1), the k_{PL} values before and after B_1^+ correction, and the percent difference. There were variations between the SNR gains of the metabolite peaks, where larger SNR gains were shown in those with lower SNR dynamic spectra prior to denoising.

Scan #	Cancer Origin & Notes	Optimized Tensor Ranks [freq, x, y, t]	Denoising SNR Multiplicative Increases	Flip Angle Scaling	k_{PL} Before Correction (s^{-1})	k_{PL} After Correction (s^{-1})	% Difference
1	Rectal adenocarcinoma	[18, 9, 10, 5]	Pyr: 17.5 Lac: 9.4 Ala: 4.0	1.20	0.031	0.042	-27.96
				1.03	0.038	0.040	-4.60
				1.10	0.044	0.052	-15.24
2	Rectal adenocarcinoma	[12, 8, 11, 8]	Pyr: 15.9 Lac: 20.2 Ala: 9.1	0.97	0.044	0.042	+5.77
				1.03	0.037	0.039	-5.58
				1.13	0.033	0.042	-19.49
3	Intrahepatic cholangiocarcinoma	[7, 5, 11, 18]	Pyr: 26.5 Lac: 27.6 Ala: 35.1	1.13	0.051	0.063	-19.01
				0.87	0.080	0.066	+20.22
				0.97	0.051	0.048	+5.31
4	Intrahepatic cholangiocarcinoma	[5, 6, 8, 6]	Pyr: 82.4 Lac: 101.8 Ala: 17.7	1.37	0.030	0.053	-43.62
				1.27	0.048	0.073	-34.79
				1.17	0.043	0.057	-23.64
5	Recurrent grade 1 metastatic pancreatic neuroendocrine	[14, 8, 5, 7]	Pyr: 58.7 Lac: 26.2 Ala: 28.9	0.97	0.043	0.040	+5.64
				0.97	0.029	0.027	+5.60
				1.03	0.024	0.026	-5.38
6	Recurrent grade 1 metastatic pancreatic neuroendocrine	[10, 7, 14, 3]	Pyr: 47.9 Lac: 42.3 Ala: 37.5	1.27	0.043	0.069	-37.65
				0.87	0.059	0.047	+26.96
				0.97	0.049	0.046	+6.21
7	Recurrent grade 1 metastatic pancreatic neuroendocrine	[20, 7, 12, 7]	Pyr: 12.6 Lac: 10.4 Ala: 8.7	1.27	0.041	0.066	-37.86
				0.97	0.038	0.036	+5.90
				0.97	0.032	0.031	+5.84

Good Manufacturing Practice (GMP) grade [$1\text{-}^{13}\text{C}$]pyruvic acid (ISOTEC Stable Isotope Division, MilliporeSigma, Miamisburg, OH) with trityl radical (GE Healthcare, Milwaukee, WI) was prepared and loaded in pharmacy kits (GE Healthcare, Milwaukee, WI) according to IRB- and FDA IND-approved stable-isotope manufacturing processes. Following polarization in a 5 T SPINLab clinical-research polarizer (GE Healthcare, Milwaukee, WI) and dissolution, 240 ± 5.2 mM sterile pyruvate with 7.8 ± 0.2 pH, at 33.9 ± 1.6 °C, and a polarization of $37.7 \pm 1.7\%$, was injected following pharmacist approval at 60.1 ± 9.8 s after dissolution at a rate of 5 mL/s followed by a 20 mL saline

flush. The injection volume was determined using the weight-based dose of 0.43 mL/kg (total body weight) with a maximum of 40 mL.

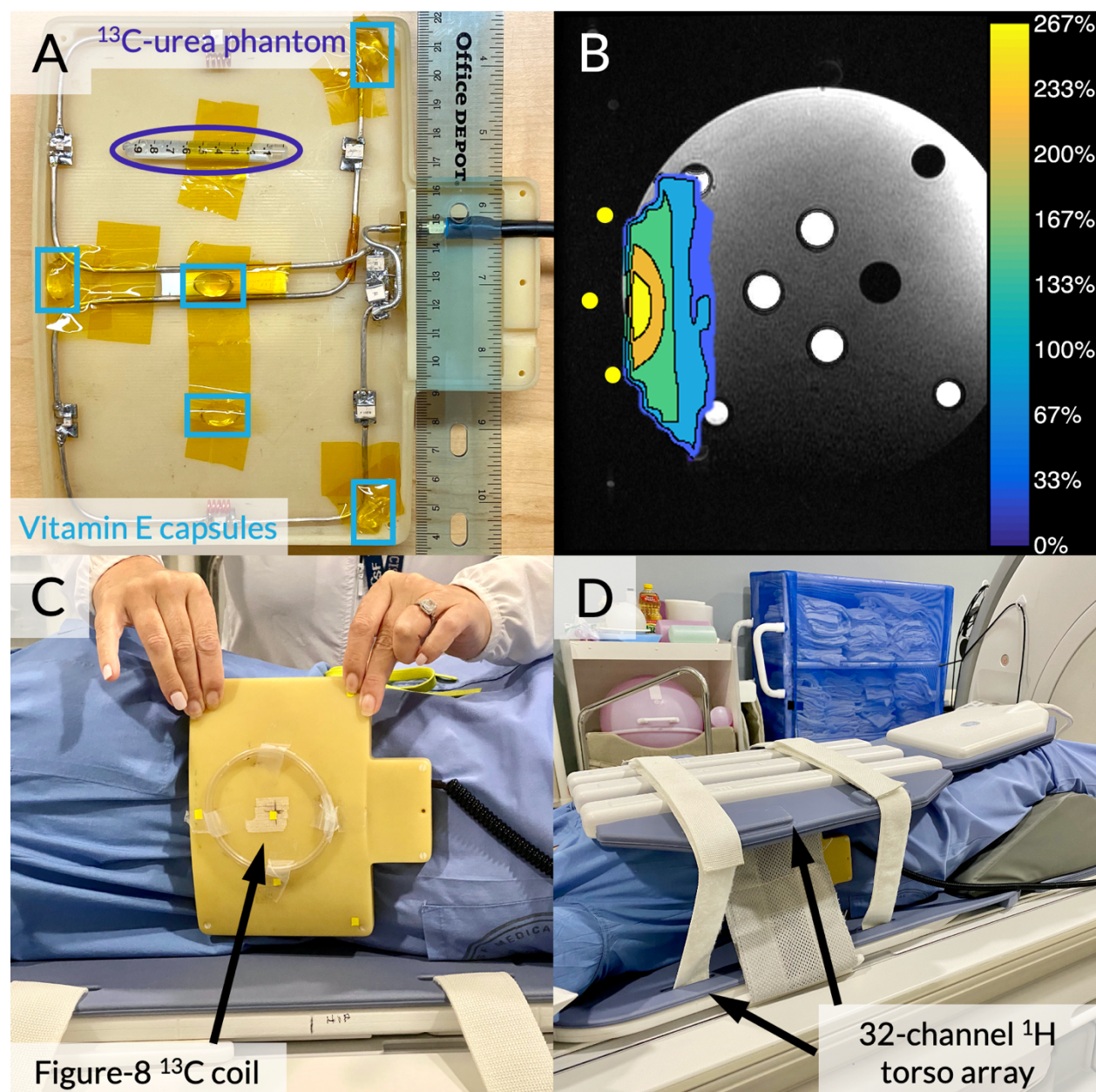


Figure 4.1. (A) The figure-8 T/R coil opened with a ^{13}C -enriched urea phantom used for power calibration highlighted by a purple circle and vitamin E capsule fiducial markers highlighted by light blue rectangles. (B) The coil's B_1^+ profile acquired using the double angle method. The contour map indicates the actual flip angle delivered relative to the prescribed flip angle. (C-D) Photos of an example coil-placement for a patient scan. Exterior markers were used for verifying coil placement following localizer scans but were not used for B_1^+ correction.

4.3.3 Data Acquisition

HP ^{13}C data were acquired using a 2D dynamic MR echo-planar spectroscopic imaging (EPSI) pulse sequence consisting of a slice-selective spectral-spatial pulse followed by phase-encode and echo-planar spectroscopic imaging readout similar to prior prostate cancer studies.^{12,22,23} The scan parameters were as follows: 130 ms/3.5-5.2 ms TR/TE, 1.2-3 cm slice thickness, 1.2 by 1.2 cm in-plane spatial resolution and 3 s temporal resolution, 60 s acquisition window, 545 Hz spectral bandwidth, constant flip angles of 10° for pyruvate, 20° for lactate, and 15° for alanine. Acquisition was started 5 s after the injection completed. Each patient was asked to breath hold for as long as comfortable once the acquisition began. T_1 -weighted spoiled gradient-echo ^1H images (with 4.0 ms/1.8 ms TR/TE) and T_2 -weighted single-shot fast spin echo ^1H images (with 545.24 ms/81.662 TR/TE) images were acquired for anatomic references.

4.3.4 Denoising

The analysis pipeline began with a B_0 inhomogeneity correction that shifted peaks in the spectral dimension.^{15,24} For each voxel, the cross correlation between a standard spectrum and the voxel's spectrum was computed and the index of the maximum value was used to obtain the new pyruvate peak index. The pipeline continued with tensor rank truncation for denoising the HP data.^{25,26} The spectral, spatial, and temporal dimensions of HP ^{13}C MRSI data were broken down into principal component fibers using high-order singular value decomposition. As the chemical shift spectrum, geometric space, and metabolic dynamics were inherently low rank, the dimensions of the HP ^{13}C MRSI data could be represented by a truncated number of fibers. The optimal number of tensor ranks to preserve in each dimension was computed using a bias-variance tradeoff that balances between spurious artifacts and noise removal.²⁶ Finally, tensor rank truncation was followed by zero-order and first-order phase corrections and a baseline correction. Metabolite signals were calculated by

integrating each peak without any overlap due to the sparsity of the HP ^{13}C spectra. Images were sinc interpolated to a matrix size of 1024 by 1024. Pyruvate and lactate SNR thresholds (defined as the mean of the metabolite's signal divided by the standard deviation of the spectral noise) were implemented to mask out noise. Voxels outside of the coil's sensitive region, determined by the acquired B_1^+ map described below, were removed.

4.3.5 B_1^+ Transmit Field Inhomogeneity Correction

Prior to the patient studies, a transmit inhomogeneity B_1^+ field map was acquired from a phantom (Figure 4.1B) using the double angle method (DAM).²⁷⁻²⁹ This method calculates a flip-angle map as an indirect measurement of the B_1 excitation field. Two images are acquired, I_1 with the prescribed flip angle α_1 and I_2 with the prescribed flip angle $\alpha_2 = 2\alpha_1$. Other acquisition parameters were kept constant. Using a TR of 3 s, T_1 effects were negligible and the equation below was used to compute the B_1^+ map, $\alpha(r)$:

$$\alpha(r) = \arccos\left(\frac{I_2(r)}{2I_1(r)}\right) \quad (4.1)$$

The surface coil was strapped to a 25 cm diameter cylindrical ethylene glycol phantom.³⁰ The ^{13}C center frequency was placed on the central ethylene glycol resonance. The B_1^+ data was acquired using a metabolite-selective sequence with a single-shot echoplanar readout, with $\alpha_1 = 30^\circ$ and $\alpha_2 = 60^\circ$, a 20×20 matrix zero-filled to 32×32 , with voxel sizes of $0.875 \times 0.875 \times 4.0$ cm. With two flip angles, a NEX of 100, and a TR of 3 s, the total scan time was 600 s. The B_1^+ map was computed using Equation 4.1 and thresholded to remove noise voxels.

As the fiducial markers were present in T_1 -weighted images from the initial DAM acquisition and from subsequent patient scans, each marker had corresponding Left, Posterior, Superior (LPS) coordinates in DICOM images. A least squares estimation method^{31,32} was used to compute rotation

and translation matrices that would transform the fiducial markers' DAM acquisition LPS coordinates to patient scan coordinates. The B_1^+ map and the ^{13}C images were correspondingly converted from pixels to physical dimensions, matching the LPS coordinate system. The B_1^+ map was transformed as above and interpolated to the resolution of the ^{13}C scans, resulting in a registered B_1^+ map where each ^{13}C voxel corresponded to a B_1^+ scaling factor. This scaling factor, the relative transmit power per voxel, was used to scale the nominal flip angle accordingly. The corrected flip angle was subsequently provided as a parameter for an inputless two-site exchange model¹⁴ to estimate the forward reaction rate of pyruvate to lactate, or k_{PL} . k_{PL} maps were sinc interpolated to a matrix size of 1024 by 1024. Monte Carlo simulations were used to compute expected k_{PL} variations when varying B_1^+ in 10% increments from -20 to +100% relative to its original value.

4.4 Results

4.4.1 Patient Scans

Seven MR exams including HP ^{13}C were acquired from patients with progressing liver tumors from multiple primary cancers as summarized in Table 4.1. Representative data from Scan #5 are shown in Figures 4.2-4.3 and were acquired with the coil set-up shown in Figure 4.1. The conversion of pyruvate-to-lactate in the liver metastases was observed to be upregulated, consistent with the metabolic reprogramming known to occur in cancers.^{13,33,34}

4.4.2 Denoising & B_1^+ Transmit Field Inhomogeneity Correction

The denoising pipeline consisting of B_0 correction, tensor rank truncation, and zero- and first-order phase corrections was applied prior to B_1^+ correction and k_{PL} analysis for all seven scans with results summarized in Table 4.1. On average for all the voxels, pyruvate SNR increased by 37.4-fold, lactate

SNR increased by 34.0-fold, and alanine SNR increased by 20.1-fold. Figure 4.2 shows the spectral data before and after denoising for two selected voxels from a patient with metastatic pancreatic cancer to the liver (Scan #5). From left to right, the top row shows the acquired EPSI spectra before and after denoising for a tumor voxel and a normal-appearing voxel, respectively. The adjacent T_1 -weighted anatomical images highlight the tumors and selected voxels.

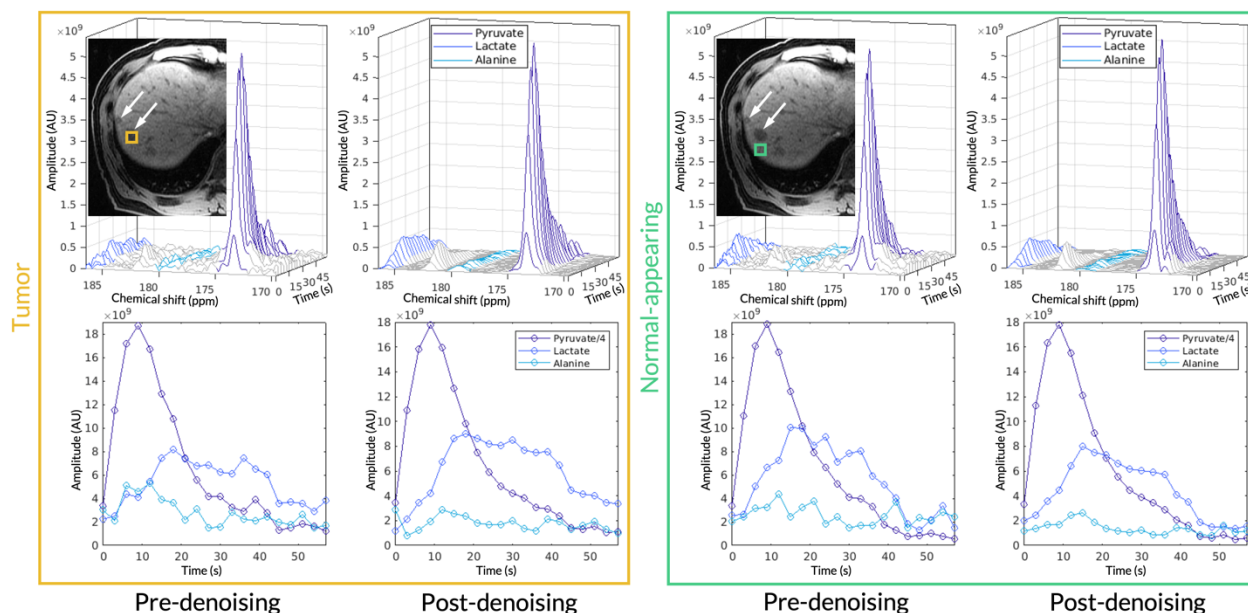


Figure 4.2. The left panel (orange box) shows the acquired HP ^{13}C EPSI spectrum and metabolite dynamics before and after denoising for the tumor voxel. Likewise, the right panel (green box) shows the acquired EPSI spectrum and metabolite dynamics before and after denoising for a normal-appearing voxel. The adjacent T_1 -weighted anatomical images highlight locations of the metastases and the selected voxel. Both are representative voxels taken from Scan #5.

Prior to denoising, there was a high noise floor obscuring the alanine peak. After denoising, both the lactate and alanine peaks were more clearly resolved both spectrally and dynamically through time with SNR increases of 26.2 and 28.9-fold, respectively. The lactate dynamic profile was likewise recovered and smoothed. Since the acquired pyruvate SNR was high, no significant changes in kinetics were observed after denoising. However, the mean pyruvate SNR increase was 58.7-fold. The dynamic curve for pyruvate remained similar pre- and post-denoising, however, the depiction of lactate and

alanine dynamics were greatly improved with the denoising pipeline, shown in the bottom row of Figure 4.2.

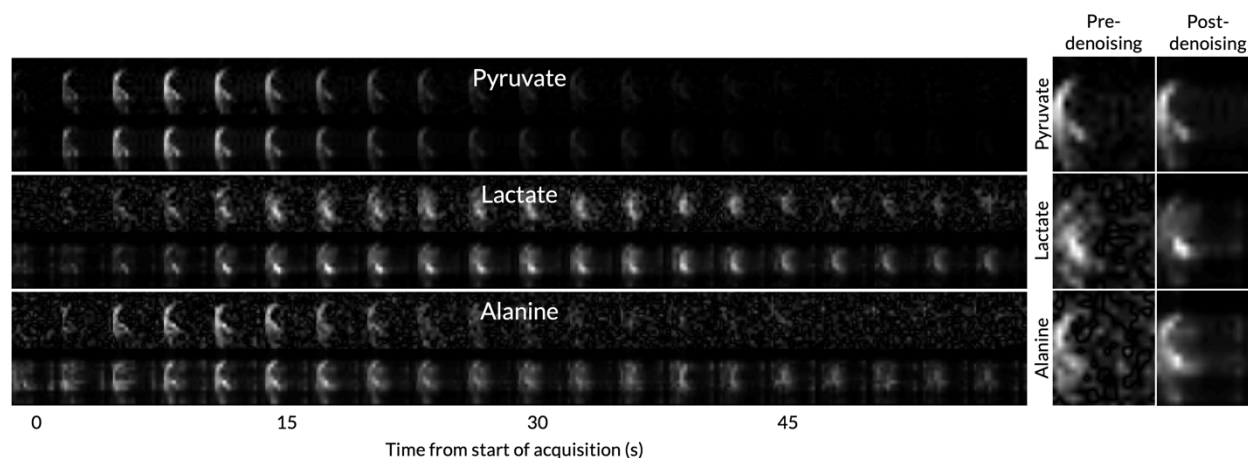


Figure 4.3. From Scan #5, the metabolite peaks from pyruvate, lactate, and alanine were integrated and the resulting time courses are shown on the left side of the figure. For each metabolite, the top row of images is from the original spectra and the bottom row of images shows the post-denoised metabolite maps. Every entire row of images is independently window-leveled relative to the other rows. On the right are displayed zoomed-in images before and after denoising for a selected time point (18 s from the start of acquisition) are highlighted on the right side of the figure.

For the same scan, the metabolite peaks of interest were integrated to create images of their spatiotemporal distributions shown in Figure 4.3. For each metabolite, the top row corresponds to pre-denoised spectra and the bottom row to post-denoised spectra, both rows independently normalized for display. Shown on the right are zoomed-in images for each metabolite pre- and post-denoising for the selected time point 18 s from the start of acquisition, corresponding to the peak of the lactate signal. The background noise was most apparent in the lactate and alanine pre-denoised images. In the denoised lactate images, bright voxels at $t = 18$ s correspond to the increased conversion to lactate in the metastatic tumors. However, the shape and location of these hot spots were blurred before denoising. These differences are clearly shown in the images on the right of the figure. The alanine signal is also noticeably recovered from a noisy background at $t = 21$ s. The improvement for pyruvate detection is not as significant because of its high SNR before denoising.

In addition to denoising, this analysis pipeline provided flip angle corrections by using a B_1^+ map acquired from a phantom scan to improve k_{PL} estimation (Figure 4.1B). The B_1^+ map was acquired and calculated using DAM and is shown as a contour map in Figure 4.1B showing variations in the B_1^+ field. The corresponding color bar indicates the relative power delivered to the region; 100% indicates the region received the prescribed flip angle.

Representative B_1^+ correction data are shown in Figure 4.4 from a patient with cholangiocarcinoma (Scan #3). Figure 4.4A shows an axial T_1 -weighted spoiled gradient-echo anatomical scan with arrows highlighting large tumors. Two tumor voxels were selected, labeled Voxel #1 and #2. Figure 4.4B shows the previously acquired B_1^+ map aligned using the coil's fiducial markers, highlighted in yellow. Figure 4.4C-D depict the k_{PL} values for Voxel #1 before and after B_1^+ correction, respectively. Before B_1^+ correction, the estimated k_{PL} for this voxel was 0.051 s^{-1} . After B_1^+ correction, the estimated k_{PL} was 0.063 s^{-1} . This voxel was over-flipped by 13% resulting in a -19.01% underestimation of k_{PL} without B_1^+ correction. Figure 4.4E-F depict the k_{PL} values for Voxel #2 before and after B_1^+ correction, respectively. Before B_1^+ correction, the estimated k_{PL} for this voxel was 0.080 s^{-1} . After B_1^+ correction, the estimated k_{PL} was 0.066 s^{-1} . This voxel was under-flipped by 13% resulting in a 20.22% overestimation of k_{PL} without B_1^+ correction. These voxels corresponded with the Monte Carlo simulations in that over-flipping resulted in an underestimation of k_{PL} and under-flipping resulted in an overestimation of k_{PL} (Supporting Information Figure S4.1).

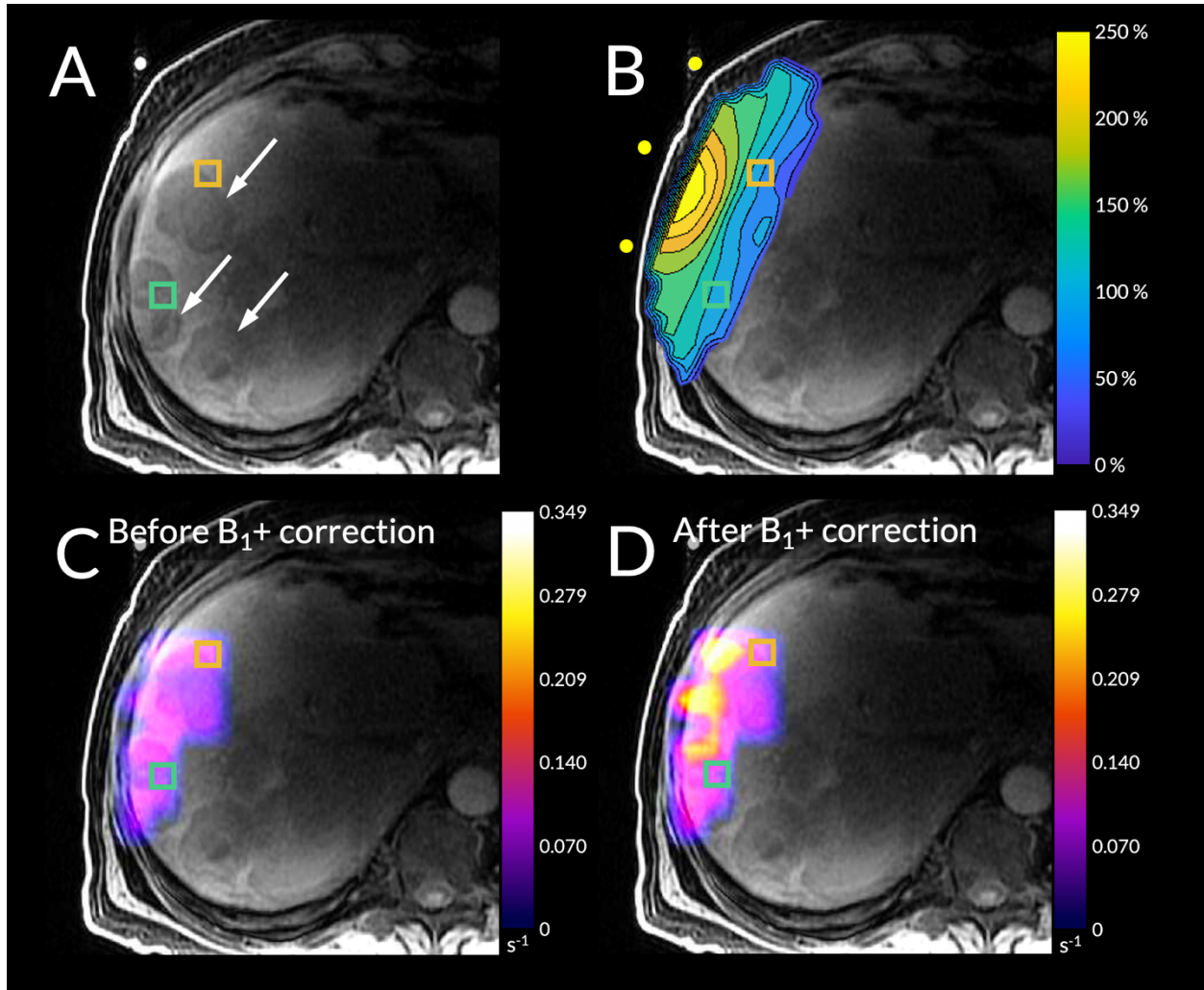


Figure 4.4. From Scan #3, **(A)** an axial T₁-weighted spoiled gradient-echo anatomical scan with an over-flipped tumor voxel highlighted in green (Voxel #1) and an under-flipped tumor voxel highlighted in orange (Voxel #2). **(B)** The B₁⁺ profile aligned to its position during the scan using the coil's fiducial markers. **(C)** The k_{PL} map before B₁⁺ correction. **(D)** The k_{PL} map after B₁⁺ correction. For Voxel #1, over-flipped by +13%, there was a -19.01% underestimation of k_{PL} without B₁⁺ correction (0.051 s⁻¹ before denoising and 0.063 s⁻¹ after denoising). For Voxel #2, under-flipped by -13%, there was a +20.22% overestimation of k_{PL} without B₁⁺ correction (0.080 s⁻¹ before denoising and 0.066 s⁻¹ after denoising).

4.5 Discussion

Hyperpolarized ^{13}C MRI has been used to quantitatively and dynamically image in vivo metabolic activity in a variety of human studies including cardiac diseases,^{2,3} breast cancer,^{4,5} brain cancer,⁶⁻⁹ and prostate cancer.¹⁰⁻¹² Due to metabolic reprogramming, cancer cells demonstrate upregulated expression and activity of LDH,^{35,36} the enzyme catalyzing the conversion of pyruvate to lactate, even in the presence of adequate oxygen (the “Warburg effect”).³³ Thus, metabolic conversion from pyruvate to lactate (or k_{PL}) within the cancer cell can serve as a biomarker of tumor characterization,³⁷ tumor aggressiveness and grading,^{11,38-40} metabolic pathway inhibition, and response to drug therapies.¹⁰ In mouse models, HP lactate signals correlated significantly with histologic prostate cancer grade as expected with increased LDH activity.^{38,40} Furthermore, the metabolic flux of pyruvate to lactate intratumorally has been shown to be a biomarker of response to therapy.¹⁷⁻¹⁹ Notably, changes in cancer HP [1- ^{13}C]pyruvate metabolism has been shown to be a more sensitive biomarker of early response to therapy compared to [^{18}F]FDG-PET in preclinical models.²⁰ In human studies, HP [1- ^{13}C]pyruvate MR has been used to interrogate metabolism in healthy volunteers^{2,41-43} and cancer patients, investigating metabolic reprogramming in primary tumors and metastases.^{5-7,10,12,22,44-47} These studies demonstrated that k_{PL} can serve as a biomarker and provide insight into the reprogrammed metabolism of tumors, elucidate response to therapy, and afford the ability to look at cancer progression and aggressiveness.

Differing from prior studies, this new project was designed to develop specialized methods to investigate liver tumor metabolism in patients using HP [1- ^{13}C]pyruvate. The goal of the project was to characterize these liver metastases, requiring a dedicated surface coil for acquisition. However, surface coils have an inherently inhomogeneous B_1^+ profile resulting in flip angles that vary through space. B_1^+ correction is especially important for studying inter- and intra-tumor heterogeneity and/or comparing cancerous tissue to normal-appearing tissue. Hence, for the first time, we implemented a

B_1^+ correction method within a denoising pipeline for improved spectral SNR using a figure-8 T/R ^{13}C surface coil.

To elucidate the relationships between B_1^+ error and k_{PL} estimations in the inputless model, the Monte Carlo simulations had to be modified to match the EPSI acquisitions. Methods were similar to prior work, however, instead of consolidating all excitations of a time point into a single effective flip angle (equation 4-7 in reference 14), each excitation per phase-encode was individually simulated and signal summation was performed later. This is more precise in that it allows for relaxation and conversion to occur between each RF pulse. Hence, for 16 phase encodes and 20 time points, all 320 excitations were computed. As seen from the Monte Carlo simulations presented in Supporting Information Figure S1, inaccuracies in k_{PL} estimations arise when it is assumed that all voxels receive the same prescribed nominal flip angle when in reality, there is non-negligible variation of power as a function of space. Hence, to more accurately estimate rates of conversion, namely the first-order conversion rate of pyruvate to lactate (k_{PL}), one must use a B_1^+ map to scale each voxel's flip angle correspondingly. In this work, we developed a novel EPSI processing pipeline that appends B_1^+ correction after a series of spectral processing steps: B_0 inhomogeneity corrections, tensor rank truncation to improve metabolite SNR, and zero- and first-order phase corrections.

In processing the HP ^{13}C EPSI data, the spectral data was denoised prior to B_1^+ correction. The spectra pre- and post-denoising of a representative voxel are shown in Figure 4.2. On average, pyruvate, lactate, and alanine SNRs were improved by 37.4, 34.0, and 20.1-fold in the spectral dimension, respectively, thus substantially recovering metabolite dynamics. This is most noticeable with the lactate and alanine peaks, which are either slightly above or entirely shrouded by the noise floor. By removing extraneous ranks primarily in the frequency dimension of the HP ^{13}C MRSI tensor, low signal metabolites can be extracted for improved subsequent kinetic modeling. The denoised lactate dynamics shown in Figure 4.2 also more accurately reflected physiological expectations.

Compared to the pre-denoised dynamics, the post-denoised dynamics have an elongated lactate plateau beginning from around 18 s until 40 s. With the liver's dual input blood supply from the hepatic artery and the portal vein, we should expect a sustained lactate peak as the portal vein, which delivers two-thirds of the liver's blood supply, brings HP ^{13}C lactate produced by the gastrointestinal tract to the liver. This physiological phenomenon is not as clearly perceptible prior to denoising and is reflected in the denoised dynamics. The denoised spectra were also corrected for B_1^+ field inhomogeneities before modeling metabolite dynamics in each voxel. A previously measured B_1^+ map using DAM was used to scale the nominal flip angle for each voxel. The corrected flip angles with the denoised spectra were provided as parameters for an inputless two-site model to estimate k_{PL} . The corrected k_{PL} values were compared against the expected changes derived from Monte Carlo simulations in which B_1^+ was varied. As shown in Supporting Information Figure S4.1 (appended below), the corrected k_{PL} values fit closely to the ± 1 standard deviation bounds and match the inverse relationship between relative B_1^+ error and fractional k_{PL} error: positive errors in B_1^+ resulted in underestimations of k_{PL} and negative errors resulted in overestimations.

The developed methods here not only restored quantitative accuracy in regions receiving excess or insufficient RF power due to transmit field inhomogeneity, but more importantly increased the number of available voxels outside of the B_1 -calibrated region of interest for k_{PL} estimations both in other lesions and in normal-appearing tissue. Limitations of the methods developed in this project include the need for prior mapping of the B_1^+ inhomogeneity profile specific to the coil. Recent real-time power calibration and B_1^+ mapping⁴⁸ could improve this approach for the future.

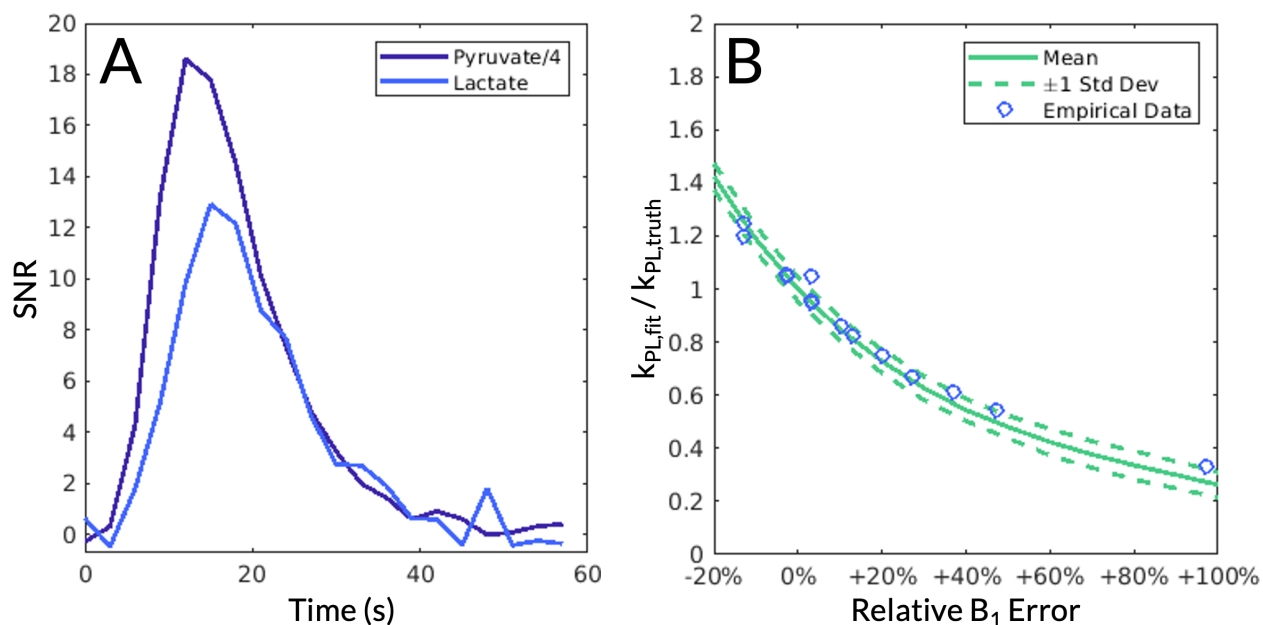
4.6 Conclusions

In this project, a specialized HP ^{13}C EPSI post-processing pipeline was developed that integrated tensor denoising and B_1^+ correction to measure k_{PL} conversion rates in patients with liver tumors, in order to improve the quantitative accuracy of surface coil HP ^{13}C metabolic MR in cancer patients. This approach could benefit future clinical trials using HP ^{13}C MRSI to measure cancer metabolism and response to targeted drug therapies.

4.7 Acknowledgements

This work was supported by NIH grants R01CA183071, U01EB026412, R01DK115987, and P41EB013598. We would also like to acknowledge the assistance of Jasmine Graham, Jim Slater, Mary Frost, Hope Williams, Kimberly Okamoto, and Jennifer Chow.

4.8 Supporting Information



Supporting Information Figure S4.1. (A) The simulated pyruvate and lactate signals. Following similar approaches,¹⁴ the inputless two-site exchange model was used, an approach that only fits the lactate magnetization and not the pyruvate magnetization while the measured pyruvate magnetization is used as the input at each time point. The nominal simulation values were $k_{PL} = 0.03 \text{ s}^{-1}$, T_1 of pyruvate = 30 s, and T_1 of lactate = 25 s. The noise standard deviation was set at 0.004 relative to a fixed total magnetization input normalized to 1. This value was chosen to approximately match the SNR of the simulated data with typical empirical data. The gamma-distribution function to simulate the pyruvate and lactate signals had an arrival time of 4 seconds and a full width at half-maximum of 8 s. The flip angle scheme was modified to match that of an EPSI acquisition with nominal 10° and 20° flips for pyruvate and lactate, respectively, for each of the 16 phase encodes and 20 time points. All 320 excitations were used to recapitulate each excitation's effect on the magnetization. Every 16 points, corresponding to each phase encode step, were averaged to match the final imaging scenario. **(B)** Monte Carlo simulations of the two-site inputless model demonstrated an inverse relationship between the relative B_1^+ error and the fractional k_{PL} error, the simulated k_{PL} values ($k_{PL,fit}$) against the input k_{PL} of 0.03 s^{-1} ($k_{PL,true}$). The solid and dashed lines indicate the mean and ± 1 standard deviation, respectively. Positive errors in B_1^+ resulted in underestimations of k_{PL} and negative errors resulted in overestimations, agreeing with acquired data. This relationship corresponded with the computed k_{PL} maps before and after B_1^+ correction. The selected voxels presented in Table 4.1 are indicated with blue circles and all but one are within the 1 standard deviation bounds.

4.9 References

1. Ardenkjær-Larsen JH, Golman K, Gram A, et al. Increase of signal-to-noise of more than 10,000 times in liquid state NMR. *Discov Med*. 2003;100(18):10158-10163.
2. Cunningham CH, Lau JYC, Chen AP, et al. Hyperpolarized ¹³C Metabolic MRI of the Human Heart: Initial Experience. *Circ Res*. 2016;119(11):1177-1182.
doi:10.1161/CIRCRESAHA.116.309769
3. Rider OJ, Apps A, Miller JJJ, et al. Noninvasive In Vivo Assessment of Cardiac Metabolism in the Healthy and Diabetic Human Heart Using Hyperpolarized ¹³C MRI. *Circ Res*. 2020;126(6):725-736. doi:10.1161/CIRCRESAHA.119.316260
4. Abeyakoon O, Latifoltojar A, Gong F, et al. Hyperpolarised ¹³C MRI: a new horizon for non-invasive diagnosis of aggressive breast cancer. *BJR Case Rep*. 2019;5(3):20190026.
doi:10.1259/bjrcr.20190026
5. Gallagher FA, Woitek R, McLean MA, et al. Imaging breast cancer using hyperpolarized carbon-13 MRI. *Proc Natl Acad Sci U S A*. 2020;117(4):2092-2098.
doi:10.1073/pnas.1913841117
6. Park I, Larson PEZ, Gordon JW, et al. Development of methods and feasibility of using hyperpolarized carbon-13 imaging data for evaluating brain metabolism in patient studies. *Magn Reson Med*. 2018;80(3):864-873. doi:10.1002/mrm.27077
7. Miloushev VZ, Granlund KL, Boltyanskiy R, et al. Metabolic imaging of the human brain with hyperpolarized ¹³C Pyruvate demonstrates ¹³C lactate production in brain tumor patients. *Cancer Res*. 2018;78(14):3755-3760. doi:10.1158/0008-5472.CAN-18-0221
8. Autry AW, Gordon JW, Carvajal L, et al. Comparison between 8- and 32-channel phased-array receive coils for in vivo hyperpolarized ¹³C imaging of the human brain. *Magn Reson Med*. 2019;82(2):833-841. doi:10.1002/mrm.27743

9. Mammoli D, Carvajal L, Slater JB, et al. Kinetic Modeling of Hyperpolarized Carbon-13 Pyruvate Metabolism in the Human Brain. *IEEE Trans Med Imaging*. 2020;39(2):320-327. doi:10.1109/TMI.2019.2926437
10. Aggarwal R, Vigneron DB, Kurhanewicz J. Hyperpolarized 1-[13C]-Pyruvate Magnetic Resonance Imaging Detects an Early Metabolic Response to Androgen Ablation Therapy in Prostate Cancer. *Eur Urol*. 2017;72(6):1028-1029. doi:10.1016/j.eururo.2017.07.022
11. Granlund KL, Tee SS, Vargas HA, et al. Hyperpolarized MRI of Human Prostate Cancer Reveals Increased Lactate with Tumor Grade Driven by Monocarboxylate Transporter 1. *Cell Metab*. 2020;31(1):105-114. doi:10.1016/j.cmet.2019.08.024
12. Chen HY, Aggarwal R, Bok RA, et al. Hyperpolarized 13C-pyruvate MRI detects real-time metabolic flux in prostate cancer metastases to bone and liver: a clinical feasibility study. *Prostate Cancer Prostatic Dis*. 2020;23(2):269-276. doi:10.1038/s41391-019-0180-z
13. Kurhanewicz J, Vigneron DB, Ardenkjaer-Larsen JH, et al. Hyperpolarized 13C MRI: Path to Clinical Translation in Oncology. *Neoplasia (United States)*. 2019;21(1):1-16. doi:10.1016/j.neo.2018.09.006
14. Larson PEZ, Chen HY, Gordon JW, et al. Investigation of analysis methods for hyperpolarized 13C-pyruvate metabolic MRI in prostate cancer patients. *NMR Biomed*. 2018;31(11):e3997. doi:10.1002/nbm.3997
15. Crane JC, Gordon JW, Chen HY, et al. Hyperpolarized 13C MRI data acquisition and analysis in prostate and brain at University of California, San Francisco. *NMR Biomed*. 2021;34(5):e4280. doi:10.1002/nbm.4280
16. Wang ZJ, Ohliger MA, Larson PEZ, et al. Hyperpolarized 13C MRI: State of the art and future directions. *Radiology*. 2019;291(2):273-284. doi:10.1148/radiol.2019182391
17. Day SE, Kettunen MI, Gallagher FA, et al. Detecting tumor response to treatment using

- hyperpolarized ^{13}C magnetic resonance imaging and spectroscopy. *Nat Med*. 2007;13(11):1382-1387. doi:10.1038/nm1650
18. Chaumeil MM, Ozawa T, Park IW, et al. Hyperpolarized ^{13}C MR spectroscopic imaging can be used to monitor Everolimus treatment in vivo in an orthotopic rodent model of glioblastoma. *Neuroimage*. 2012;59(1):193-201. doi:10.1016/j.neuroimage.2011.07.034
 19. Radoul M, Chaumeil MM, Eriksson P, Wang AS, Phillips JJ, Ronen SM. MR studies of glioblastoma models treated with dual PI3K/mTOR inhibitor and temozolomide: Metabolic changes are associated with enhanced survival. *Mol Cancer Ther*. 2016;15(5):1113-1122. doi:10.1158/1535-7163.MCT-15-0769
 20. Hesketh RL, Wang J, Wright AJ, et al. Magnetic resonance imaging is more sensitive than PET for detecting treatment-induced cell death-dependent changes in glycolysis. *Cancer Res*. 2019;79(14):3557-3569. doi:10.1158/0008-5472.CAN-19-0182
 21. Walker CM, Fuentes D, Larson PEZ, Kundra V, Vigneron DB, Bankson JA. Effects of excitation angle strategy on quantitative analysis of hyperpolarized pyruvate. *Magn Reson Med*. 2019;81(6):3754-3762. doi:10.1002/mrm.27687
 22. Nelson SJ, Kurhanewicz J, Vigneron DB, et al. Metabolic Imaging of Patients with Prostate Cancer Using Hyperpolarized $[1-^{13}\text{C}]$ Pyruvate. *Sci Transl Med*. 2013;5(198):198ra108. doi:10.1126/scitranslmed.3006070
 23. Chen HY, Larson PEZ, Gordon JW, et al. Technique development of 3D dynamic CS-EPSI for hyperpolarized ^{13}C pyruvate MR molecular imaging of human prostate cancer. *Magn Reson Med*. 2018;80(5):2062-2072. doi:10.1002/mrm.27179
 24. Larson PE, Bok R, Kerr AB, et al. Investigation of Tumor Hyperpolarized $[1-^{13}\text{C}]$ -Pyruvate Dynamics Using Time-Resolved Multiband RF Excitation Echo-Planar MRSI. *Magn Reson Med*. 2010;63(3):582-591. doi:10.1038/jid.2014.371

25. Brender JR, Kishimoto S, Merkle H, et al. Dynamic Imaging of Glucose and Lactate Metabolism by ^{13}C -MRS without Hyperpolarization. *Sci Rep.* 2019;9:3410.
doi:10.1038/s41598-019-38981-1
26. Chen HY, Autry AW, Brender JR, et al. Tensor image enhancement and optimal multichannel receiver combination analyses for human hyperpolarized ^{13}C MRSI. *Magn Reson Med.* 2020;84(6):3351-3365. doi:10.1002/mrm.28328
27. Stollberger R, Wach P, McKinnon G, Justich E, Ebner F. RF-filed mapping in vivo. In: *Proceedings of the 7th Annual Meeting of SMRM, San Francisco, CA, USA.* ; 1988:106.
28. Insko E, Bolinger L. B1 Mapping. In: *Proceedings of the 11th Annual Meeting of SMRM, Berlin, Germany.* ; 1992:4302.
29. Cunningham CH, Pauly JM, Nayak KS. Saturated double-angle method for rapid B1+ mapping. *Magn Reson Med.* 2006;55(6):1326-1333. doi:10.1002/mrm.20896
30. Hansen RB, Sánchez-Heredia JD, Bøgh N, et al. Coil profile estimation strategies for parallel imaging with hyperpolarized ^{13}C MRI. *Magn Reson Med.* 2019;82(6):2104-2117.
doi:10.1002/mrm.27892
31. Jacobsen M. Absolute Orientation - Horn's method. MATLAB Central File Exchange.
Published 2020. <https://www.mathworks.com/matlabcentral/fileexchange/26186-absolute-orientation-horn-s-method>
32. Ohliger MA, Gordon JW, Carvajal L, et al. ^{55}Mn -based fiducial markers for rapid and automated RF coil localization for hyperpolarized ^{13}C MRI. *Magn Reson Med.* 2021;85(1):518-530. doi:10.1002/mrm.28424
33. Warburg O. On the origin of cancer cells. *Science (80-).* 1956;123(3191):309-314.
doi:10.1126/science.123.3191.309
34. Vander Heiden MG, DeBerardinis RJ. Understanding the Intersections between Metabolism

- and Cancer Biology. *Cell*. 2017;168(4):657-669. doi:10.1016/j.cell.2016.12.039
35. Hu S, Balakrishnan A, Bok RA, et al. ¹³C-pyruvate imaging reveals alterations in glycolysis that precede c-Myc-induced tumor formation and regression. *Cell Metab*. 2011;14(1):131-142. doi:10.1016/j.cmet.2011.04.012
36. Keshari KR, Sriram R, Van Criekinge M, et al. Metabolic reprogramming and validation of hyperpolarized ¹³C lactate as a prostate cancer biomarker using a human prostate tissue slice culture bioreactor. *Prostate*. 2013;73(11):1171-1181. doi:10.1002/pros.22665
37. Sriram R, Van Criekinge M, Delos Santos J, et al. Non-Invasive Differentiation of Benign Renal Tumors from Clear Cell Renal Cell Carcinomas Using Clinically Translatable Hyperpolarized ¹³C Pyruvate Magnetic Resonance. *Tomography*. 2016;2(1):35-42. doi:10.18383/j.tom.2016.00106
38. Albers MJ, Bok R, Chen AP, et al. Hyperpolarized ¹³C lactate, pyruvate, and alanine: Noninvasive biomarkers for prostate cancer detection and grading. *Cancer Res*. 2008;68(20):8607-8615. doi:10.1158/0008-5472.CAN-08-0749
39. Sriram R, Van Criekinge M, Hansen A, et al. Real-time measurement of hyperpolarized lactate production and efflux as a biomarker of tumor aggressiveness in an MR compatible 3D cell culture bioreactor. *NMR Biomed*. 2015;28(9):1141-1149. doi:10.1002/nbm.3354
40. Serrao EM, Kettunen MI, Rodrigues TB, et al. MRI with hyperpolarised [1-¹³C]pyruvate detects advanced pancreatic preneoplasia prior to invasive disease in a mouse model. *Gut*. 2016;65(3):465-475. doi:10.1136/gutjnl-2015-310114
41. Grist JT, McLean MA, Riemer F, et al. Quantifying normal human brain metabolism using hyperpolarized [1-¹³C]pyruvate and magnetic resonance imaging. *Neuroimage*. 2019;189:171-179. doi:10.1016/j.neuroimage.2019.01.027
42. Lee CY, Soliman H, Geraghty BJ, et al. Lactate topography of the human brain using

- hyperpolarized ¹³C-MRI. *Neuroimage*. 2020;204:116202.
doi:10.1016/j.neuroimage.2019.116202
43. Gordon JW, Autry AW, Tang S, et al. A variable resolution approach for improved acquisition of hyperpolarized ¹³C metabolic MRI. *Magn Reson Med*. 2020;84:2943-2952.
doi:10.1002/mrm.28421
44. Gordon JW, Chen HY, Autry A, et al. Translation of Carbon-13 EPI for hyperpolarized MR molecular imaging of prostate and brain cancer patients. *Magn Reson Med*. 2019;81(4):2702-2709. doi:10.1002/mrm.27549
45. Tran M, Latifoltojar A, Neves JB, et al. First-in-human in vivo non-invasive assessment of intra-tumoral metabolic heterogeneity in renal cell carcinoma. *BJR | case reports*. 2019;5(3):20190003. doi:10.1259/bjrcr.20190003
46. Stødkilde-Jørgensen H, Laustsen C, Hansen ESS, et al. Pilot Study Experiences With Hyperpolarized [1-¹³C]pyruvate MRI in Pancreatic Cancer Patients. *J Magn Reson Imaging*. 2020;51(3):961-963. doi:10.1002/jmri.26888
47. Autry AW, Gordon JW, Chen HY, et al. Characterization of serial hyperpolarized ¹³C metabolic imaging in patients with glioma. *NeuroImage Clin*. 2020;27:102323.
doi:10.1016/j.nicl.2020.102323
48. Tang S, Milshteyn E, Reed G, et al. A regional bolus tracking and real-time B1 calibration method for hyperpolarized ¹³C MRI. *Magn Reson Med*. 2019;81(2):839-851.
doi:10.1002/mrm.27391

Chapter 5

Hyperpolarized Carbon-13 MRI in Liver

Diseases: Recent Advances & Future

Opportunities

Ye Z, Song B, Lee PM, Ohliger MA, and Laustsen C. Hyperpolarized carbon 13 MRI in liver diseases: Recent advances and future opportunities. *Liver International*. February 2022. DOI: 10.1111/liv.15222.

5.1 Abstract

Hyperpolarized carbon-13 magnetic resonance imaging (HP ^{13}C MRI) is a recently translated metabolic imaging technique. With dissolution dynamic nuclear polarization (d-DNP), more than 10,000-fold signal enhancement can be readily reached, making it possible to visualize real time metabolism and specific substrate-to-metabolite conversions in the liver after injecting ^{13}C labeled probes. Increasing evidence suggests that HP ^{13}C MRI is a potential tool in detecting liver abnormalities, predicting disease progression and monitoring response treatment. In this review, we will introduce the recent progresses of HP ^{13}C MRI in diffuse liver diseases and liver malignancies, and discuss its future opportunities from a clinical perspective, hoping to provide a comprehensive overview of this novel technique in liver diseases and highlight its scientific and clinical potential in the field of hepatology.

5.2 Introduction

The liver plays an important role in blood filtration, substance storage and all metabolic processes in the body, especially in the regulation of glycolysis and gluconeogenesis.¹ Aberrated metabolism is often directly linked to various liver pathological conditions.² It is worth noting that chronic diffuse liver diseases, such as nonalcoholic fatty liver disease (NAFLD) and cirrhosis, are becoming global health concerns and require early diagnosis and proper management.³ Likewise, liver cancer is the fourth leading cause of cancer-related death in the world,^{4,5} and imposes significant burdens on healthcare systems.

At present, histopathological assessment of hepatic tissues obtained by biopsy or resection remains the gold standard in most liver diseases. However, this invasive approach is prone to sampling error and may cause complications,⁶ which is less suitable for longitudinal studies, therefore requiring

noninvasive tools. Medical imaging has been widely applied in the detection, diagnosis and monitoring of liver diseases, including computed tomography (CT), magnetic resonance imaging (MRI) and positron emission tomography (PET). Images from CT and conventional proton MRI mainly reflect structural and functional changes and cannot assess altered metabolism. Non-invasive monitoring of metabolic changes may provide insight into understanding impaired or cancerous hepatic tissues. Currently, PET is the only imaging modality that provides metabolic information in the clinical setting. It enables visualization of hepatic glucose uptake by injecting ^{18}F labelled fluorodeoxyglucose (FDG) or fluoro-2-deoxy-D-galactose (FDGal), but fails to capture downstream metabolism that is often crucial in many pathological circumstances.⁷ Hyperpolarized (HP) MRI with carbon-13 (^{13}C) labeled substrates, also known as HP ^{13}C MRI, can uniquely track real-time metabolic uptake and conversion in vivo, which would be valuable in liver diseases.⁸

With the invention of dissolution dynamic nuclear polarization (d-DNP), dramatically enhanced signal of HP ^{13}C MRI can be detected within seconds and up to minutes after injection.⁹ By mapping the dynamic conversion between HP ^{13}C substrates and their metabolic products, for example, $[1-^{13}\text{C}]$ pyruvate to $[1-^{13}\text{C}]$ lactate or $[1-^{13}\text{C}]$ alanine, researchers can obtain additional data beyond routine imaging modalities and form a better understanding of liver pathogenesis. Recent evidence indicates that this technique holds great promise in both diffuse liver diseases¹⁰⁻¹² and liver malignancies,¹³⁻¹⁵ with special focus on detection and diagnosis; assessment of disease progression; and prediction of therapeutic responses. Therefore, this paper aims to provide a comprehensive overview of HP ^{13}C MRI in liver diseases by introducing the workflow of this technique, and then reviewing its recent applications in diffuse liver diseases and liver malignancies. More importantly, we will discuss the future opportunities in this field from a clinical perspective, hoping to highlight the scientific potential of this novel technique and foster its clinical translations in hepatology.

5.3 Hepatic Metabolism & Pyruvate

The liver is an essential metabolic organ in the body, responsible for the metabolism of carbohydrates, lipids and proteins, with pyruvate serving as the key branch point of multiple metabolic pathways. As a highly biologically relevant probe, HP [1-¹³C]pyruvate is rapidly taken up into hepatocytes following intravenous injection and metabolized into either [1-¹³C]lactate via lactate dehydrogenase (LDH) or [1-¹³C]alanine via alanine aminotransferase (ALT) in the cytoplasm. HP [1-¹³C]pyruvate can also be transported into the mitochondria and converted by pyruvate dehydrogenase (PDH) into acetyl-coenzyme A and [¹³C]CO₂, which is in rapid equilibrium with [¹³C]bicarbonate. Based on the different resonance frequencies (i.e. chemical shift) of the substrate and products, the signals of injected pyruvate and its metabolites can be detected on HP ¹³C MRI.

Hepatic metabolism is tightly controlled by a variety of factors and it changes under different liver pathological conditions.¹⁶ HP [1-¹³C]pyruvate is to date the only probe available for human examinations and thus widely studied. It has been predominantly used to interrogate metabolism associated with early and precise liver disease diagnosis and disease progression evaluation. For example, the activity of ALT is usually elevated in patients with liver injury, which can lead to the increase of [1-¹³C]alanine. Abnormal glucose and lipid metabolism also often occurs in NAFLD patients.¹⁷ In addition, metabolic reprogramming in hepatocellular carcinoma (HCC), especially the increased lactate production,¹⁸ can be identified by HP ¹³C MRI. Compared to current imaging methods, HP ¹³C MRI provides unique metabolic information about pathway-specific alterations without using ionizing radiation. This additional metabolic information opens up possible novel diagnostic and therapeutic opportunities, therefore, the multiparametric MRI examination with ¹H and ¹³C imaging will likely be the future direction for the comprehensive assessment of liver diseases (Figure 5.1).

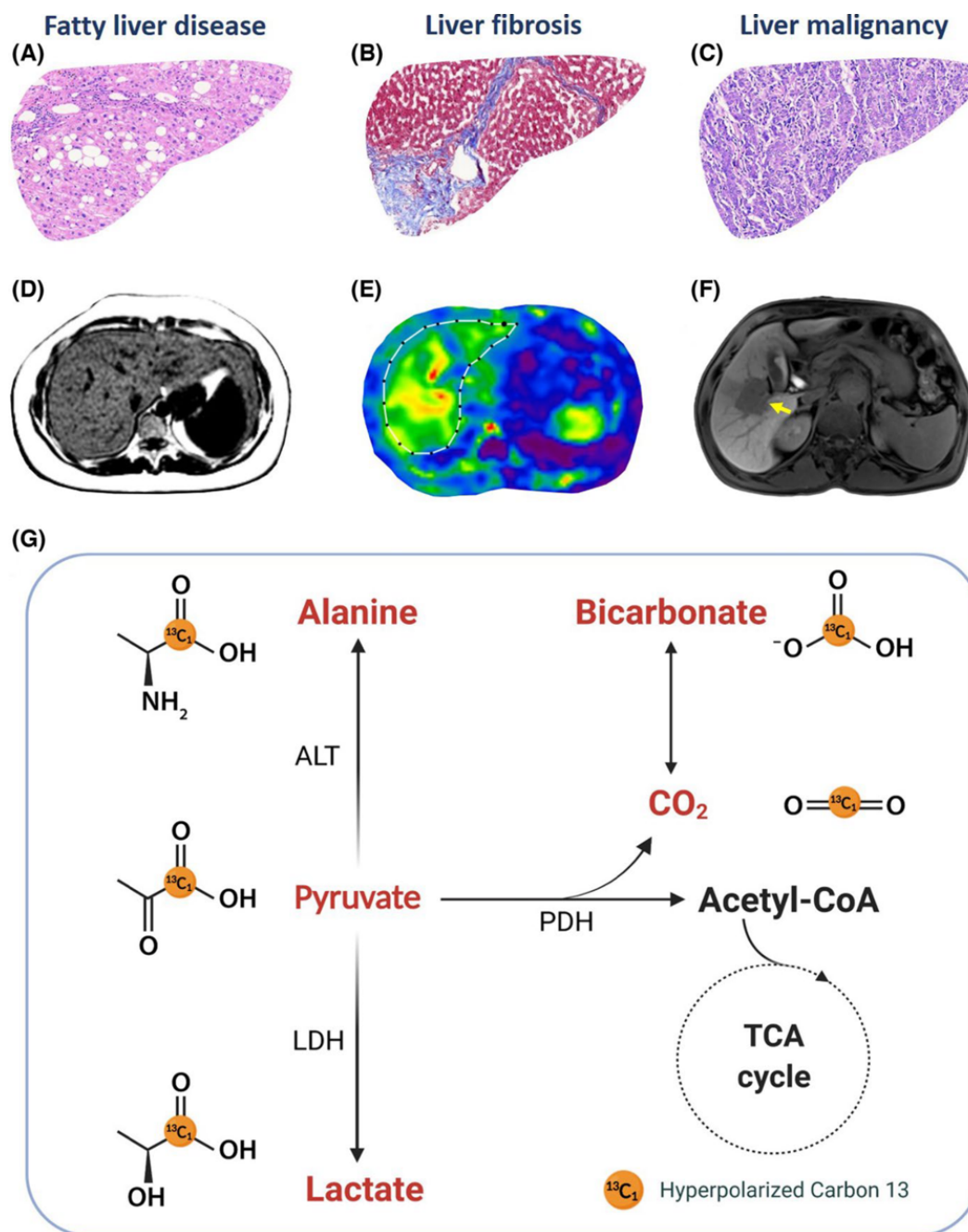


Figure 5.1. The histological changes, representative conventional images and typical metabolic pathways of different liver diseases. Fatty liver disease usually demonstrates accumulated fat droplets in histology **(A)** and high proton density fat fraction **(D)**. Liver fibrosis is characterized by excessive collagen deposition in Masson's trichrome staining **(B)** with increased stiffness in magnetic resonance elastography **(E)**. The liver malignancy typically manifests as poorly differentiated malignant cells **(C)** and a hypointense lesion (yellow arrow) in hepatobiliary phase **(F)**. These liver diseases closely associate with the change of metabolic activity **(G)**. ALT, alanine transferase; LDH, lactate dehydrogenase; PDH, pyruvate dehydrogenase; TCA, tricarboxylic acid.

5.4 Workflow of Hyperpolarized Carbon-13 MRI

The workflow of HP ^{13}C MRI is summarized in Figure 5.2, and can be simply divided into following four steps. The first step is to formulate the ^{13}C -enriched compounds by mixing ^{13}C substrate, typically [1- ^{13}C]pyruvate, and a radical with unpaired electrons. This preparation process should be conducted in a sterile environment and with the help of commercially available pharmacy kit if it is a human clinical study. Following this procedure, the sample is then placed into the polarizer to achieve hyperpolarization, where the solution experiences microwaves, cold temperature (0.8K) and strong magnetic field (5T). Based on the d-DNP technique, the unpaired electron spins can be polarized to nearly 100% in such environment, and the high polarization can be transferred to the ^{13}C isotope in ^{13}C -enriched pyruvate molecule. Current clinical polarizers can reach up to 50% polarization of [1- ^{13}C]pyruvate (MR signal is enhanced >10,000 times),¹⁹ which takes approximately 120 minutes. After the sample is polarized, a quality-control module measures its polarization level, pH, temperature, radical and pyruvate concentrations before injection to ensure it is safe for clinical use. As for the image acquisition, specialized ^{13}C radiofrequency coils are used for imaging the ^{13}C hyperpolarized molecule signals, preferably dual-tuned $^1\text{H}/^{13}\text{C}$ coils, allowing both anatomical and hyperpolarized ^{13}C imaging in a clinical workflow. Prior to injection, the scanner is calibrated for carbon imaging, including careful shimming of the main magnetic field and adjustment of the radiofrequency center frequency. Following the injection of the HP ^{13}C substrate, the subject is imaged with optimized fast ^{13}C sequences (typically less than 2 min), which would acquire the uptake and subsequent metabolic conversion in the liver parenchyma. In order to evaluate focal disease, imaging methods, such as chemical shift imaging (CSI) and spectral spatial excitation imaging, are the preferred option for liver applications. Finally, with the post-processing algorithms, the acquired data can be quantified and visualized for the exploration of metabolic alterations.²⁰ One common method is to express the total signal of downstream metabolites as a fraction of the signal from the injected probe. Alternatively,

quantitative metabolic measures such as the apparent rate constant for pyruvate-to-lactate conversion (k_{PL}) can also be calculated and quantify changes in specific drivers of the glycolysis.

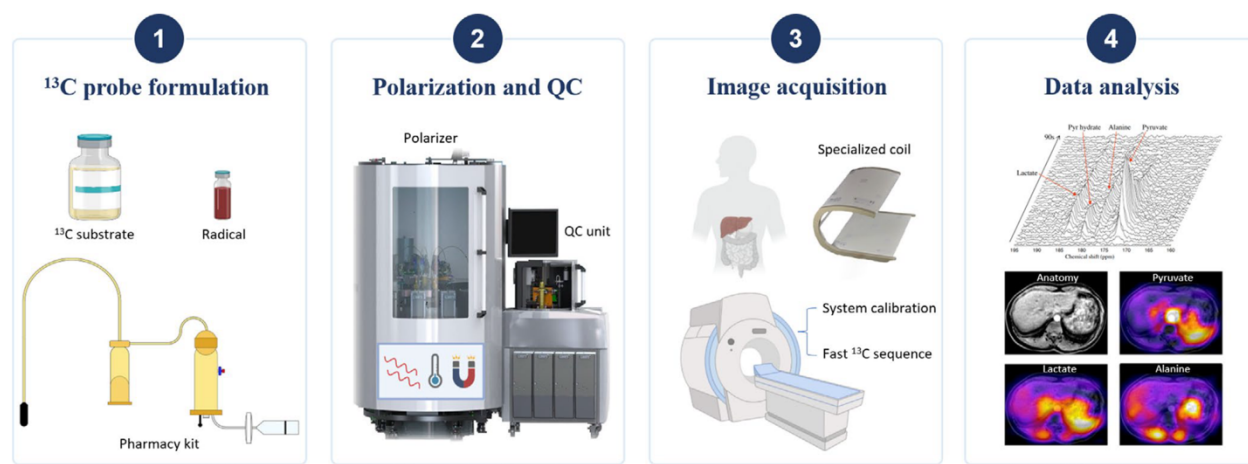


Figure 5.2. The workflow of hyperpolarized ^{13}C MRI in liver diseases. QC, quality control. The illustrations of pharmacy kit and ^{13}C spectra were reproduced with permission from reference 63 and reference 25.

Current technical challenges in HP ^{13}C MRI include the non-renewable HP ^{13}C signal, limited spatial resolution as well as unstandardized imaging procedures. The complexity and high expense of this technique may also limit its role as a primary screening and diagnostic tool in clinical practice.

5.5 Recent Advances

A summary of recent HP ^{13}C MRI studies on diffuse and focal liver diseases is shown in Table 5.1 and Table 5.2. Hereinafter, we will review the results and describe the possible clinical applications of HP ^{13}C MRI in liver injury, liver fibrosis and fatty liver diseases, as well as liver malignancies.

Table 5.1. Summary of HP ¹³C MRI in diffuse liver diseases.

Authors	Year	Probes	Subjects	Possible clinical applications
Lee et al ¹²	2013	[1- ¹³ C]pyruvate	Mice with high-fat diet induced diabetes	Assessment of drug response
Josan et al ²⁴	2015	[1- ¹³ C]pyruvate	Rats with CCl ₄ induced liver inflammation	Detection of liver injury
Kim et al ²⁵	2016	[1- ¹³ C]pyruvate	Rats with 1,3-DCP induced hepatotoxicity	Detection of liver injury
Kim et al ³⁴	2016	[1- ¹³ C]pyruvate	Rats with high-fat diet induced obesity	Detection of liver steatosis
Moon et al ³⁵	2017	[1- ¹³ C]pyruvate	Rats with high-fat diet induced NAFLD	Longitudinal assessment of NAFLD
Wilson et al ⁴⁰	2017	[1- ¹³ C]DHA	Mice with MCD diet induced NASH	Detection of monitoring of NASH
Moon et al ²⁹	2018	[1- ¹³ C]pyruvate	Rats with surgery induced hepatic IRI	Evaluation of liver injury
Moon et al ¹⁰	2019	[1- ¹³ C]pyruvate	Mice with TAA induced liver fibrosis	Detection and staging of liver fibrosis
Smith et al ¹¹	2021	[1- ¹³ C]pyruvate	Pigs with western diet induced NAFLD	Detection and monitoring of NAFLD

Abbreviations: 1,3-DCP, 1,3-dichloro-2-propanol; CCl₄, carbon tetrachloride; DHA, dehydroascorbic acid; IRI, ischaemia reperfusion injury; MCD, methionine-choline deficient; NAFLD, non-alcoholic fatty liver disease; NASH, steatohepatitis; TAA, thioacetamide.

Table 5.2. Summary of HP ¹³C MRI in liver malignancies.

Authors	Year	Probes	Subjects	Possible clinical applications
Gallagher et al ⁵⁸	2008	[5- ¹³ C]glutamine	HepG2	Assessment of tumor proliferation
Yen et al ⁵⁰	2010	[1- ¹³ C]pyruvate	Rats with Morris hepatoma	Detection of early HCC
Hu et al ⁴⁶	2011	[1- ¹³ C]pyruvate	Mice with <i>Myc</i> gene-driven liver cancer	Detection of early HCC
Darpolor et al ⁴⁹	2011	[1- ¹³ C]pyruvate	Rats with Morris hepatoma	Detection of early HCC
Von Morze et al ⁵⁹	2011	[¹³ C]urea	Tumor-bearing mice from a transgenic model	Assessment of tumor perfusion
Menzel et al ⁴⁸	2013	[1- ¹³ C]pyruvate	Rats with Morris hepatoma	Combination with PET
Cabella et al ⁶⁷	2013	[5- ¹³ C]glutamine	McA-RH7777, rats with Morris hepatoma	Evaluation of drug response
Jensen et al ⁵¹	2015	[1,3- ¹³ C ₂]EAA	HepG2, McA-RH7777, rats with Morris hepatoma	Detection of early HCC
Düwel et al ¹⁴	2016	[¹³ C, ¹⁵ N ₂]urea, [1- ¹³ C]pyruvate, [1,4- ¹³ C ₂]fumarate	Rats with Morris hepatoma	Evaluation of TAE response
Perkons et al ¹³	2020	[1- ¹³ C]pyruvate	HepG2, HR2, rats with DEN-induced HCC	Evaluation of TAE response
Chen et al ¹⁵	2020	[1- ¹³ C]pyruvate	Patients with metastatic liver cancer	Evaluation of drug response
Bliemsrieder et al ⁵⁶	2021	[1- ¹³ C]pyruvate	Rats with DEN-induced HCC	Assessment of HCC phenotypes

Note: Morris hepatoma model was built by injecting McA-RH7777 cells in rats; HR2 indicated the tumor cells derived from DEN- induced HCC rats.

Abbreviations: DEN, diethylnitrosamine; EAA, ethyl acetoacetate; HCC, hepatocellular carcinoma; HepG2, human hepatoma cells; PET, positron emission tomography; TAE, trans-arterial embolization.

5.5.1 Diffuse Liver Diseases

Liver Injury and Liver Fibrosis

Liver injury is commonly induced by excess alcohol consumption, drug intake and virus infection, which may progress to liver failure without timely intervention and thus requires early detection.^{21–23} Most liver injuries are initiated by disturbances in cellular metabolism, and present as a group of damaged hepatocytes in histology. As revealed by recent studies,^{24,25} the changed metabolism of liver impairment can be identified by HP ¹³C MRI. By intraperitoneally injecting CCl₄ in rats, Josan et al.²⁴ established an inflammatory liver injury model, and subsequently acquired the dynamic metabolic maps on them. They found both alanine/pyruvate and lactate/pyruvate ratios were higher in CCl₄-treated group compared with control group, and noted elevated activity of the ALT and LDH, respectively. Such ability of HP ¹³C MRI greatly supplements the deficiency of routine clinical blood tests for measuring ALT and LDH, as it can observe the actual changes of corresponding enzymatic activities and its spatial distribution. Similarly, Kim et al.²⁵ also suggested the levels of lactate and alanine as biomarkers in a preclinical hepatotoxicity model with administration of 1,3-dichloro-2-propanol. In animals administered the toxic chemical, liver damage was shown histologically, including hemorrhage in hepatic parenchyma, inflammatory cell infiltration, vacuolation, as well as degeneration and necrosis of hepatocytes. More importantly, a significant increase of the lactate to total carbon ratio and alanine to total carbon ratio was reported. These works confirmed the feasibility of HP ¹³C MRI in detecting liver injury, which indicates strong potential for clinical translation as it may help to monitor the disease progression and provide opportunity for treatments.

In addition, liver damage can be caused by ischemia reperfusion injury (IRI). Typically, vascular clamping is often required in major liver resection or liver transplantation to avoid excessive bleeding, which can induce a period of hepatic ischemia. When the blood flow is restored, the reperfusion could worsen cell injury on the already ischemic liver and precipitate tissue necrosis.²⁶ This

phenomenon is called hepatic IRI and can lead to acute liver failure.²⁷ Generally, alterations in biochemical and histopathological characteristics along with elevated levels of transaminases would occur during hepatic IRI, reflecting hepatocyte injury or stress.²⁸ With the application of HP ¹³C MRI, the additional metabolic changes of hepatic IRI can be captured in real time and in vivo. A recent study from Moon et al.²⁹ showed that IRI rats had increased alanine and lactate but decreased pyruvate levels, compared with both sham-operated controls and rats before IRI. They considered higher alanine level as an indicator of increased vulnerability of hepatic function to IRI, and associated the higher lactate level with increased LDH activity. Taken together with previous findings, HP ¹³C MRI and its metabolic biomarkers provide better understanding of mechanism related to liver injury, and show great promise in diagnosing and monitoring liver injury.

Repeated wound-healing response of liver injury can lead to accumulation of extracellular matrix and cause liver fibrosis, which progressively restricts normal hepatic regeneration, thereby increasing the risk of hepatic dysfunction, portal hypertension and even HCC.³⁰ Early or intermediate liver fibrosis can be reversed with elimination of causative injury triggers and the application of anti-fibrotic drugs,³¹ introducing the urgent need for its early detection and accurate staging in a noninvasive manner. Recently, Moon et al. applied HP ¹³C MRI in a liver fibrosis animal model induced by thioacetamide.¹⁰ Their findings demonstrated elevated levels of lactate and alanine in fibrosis groups compared to normal control group, validating the potential alterations of glycolysis and gluconeogenesis in hepatic fibrogenesis, and also suggested the ratios of alanine/pyruvate and alanine/total carbon as the indicators in assessing the severity of liver fibrosis. Moreover, negative correlation was presented between the level of HP ¹³C metabolites and pseudo-diffusion coefficient (D^*) derived from intravoxel incoherent motion (IVIM), which reflected perfusion-related information and was widely used to evaluate liver fibrosis.³² Hence, in conjunction with functional imaging

parameters, one could expect the future role of HP ^{13}C MRI in detecting and staging liver fibrosis, and aiding appropriate clinical therapeutic decisions.

Fatty Liver Diseases

NAFLD is characterized by excessive accumulation of fat in liver, and is histologically classified as non-alcoholic fatty liver (NAFL) and non-alcoholic steatohepatitis (NASH), with the latter presenting hepatic inflammation and oxidative stress.³³ Due to the dramatic changes in lifestyles and diet, the prevalence of NAFLD has increased in the past decades and has posed serious health and economic burdens worldwide.³ Accurate stratification of liver steatosis and early identification of NAFLD are of utmost importance in disease management, making the novel noninvasive imaging technique, HP ^{13}C MRI, a promising tool in this context. Consecutive studies from Jeong's group initially explored the time-course changes of HP ^{13}C metabolites in obese and NAFLD rats induced by high-fat diet (HFD), suggesting the increased levels of alanine and lactate as the useful biomarkers of fatty liver diseases.^{34,35} Subsequently, Smith et al. quantified the metabolic changes in NAFLD and normal pigs by measuring time to peak (TTP) of HP ^{13}C pyruvate and its metabolites.¹¹ They noted the decreased liver lactate TTP in ^{13}C spectra in NAFLD pigs, indicating an increased rate of lactate production and a disturbance in liver lipid synthesis. Based on these findings, it is anticipated to incorporate HP ^{13}C MRI in clinical practice to properly understand the underlying mechanisms of NAFLD, and eventually guide clinicians to better manage this disease and help its reversal.

A growing body of evidence suggests that NAFLD is greatly associated with metabolic dysfunctions, such as insulin resistance and type 2 diabetes mellitus (T2DM),³⁶ therefore, the nomenclature was recently revised to metabolic associated fatty liver disease (MAFLD),³⁷ allowing for a wider definition of the disease. A pioneer study by Lee et al. successfully utilized HP ^{13}C MRI to determine the changes in hepatic gluconeogenesis in HFD-induced mouse model of T2DM.¹²

Particularly, compared with control group, increased exchange rates of pyruvate to aspartate and malate were demonstrated in HFD mice, with the former exchange rate exhibiting significant correlation with gluconeogenic pyruvate carboxylase (PC) activity, suggesting the critical role of the PC pathway in hepatic glucose production. What is more, they showed that HFD mice treated with metformin displayed lower aspartate and malate signals as well as decreased exchange rates from pyruvate, agreeing with down-regulated gluconeogenesis. Encouraged by the capability of HP ^{13}C MRI in probing metabolism that were previously inaccessible in other imaging modalities, we believe this noninvasive technique may facilitate identification of novel therapeutic targets and longitudinal assessment of therapeutic response in MAFLD patients.

Given the adverse consequences of NASH, namely liver cirrhosis and cancers, it is crucial to recognize the disease at an early stage and initiate corresponding medical treatments. The ongoing research for pharmacological treatment and therapeutic targets necessitates an understanding of the metabolic pathways in this field.³⁸ Fortunately, HP ^{13}C MRI offers additional ^{13}C probes alternative to pyruvate, such as [1- ^{13}C]dehydroascorbic acid (DHA), which can be converted to Vitamin C (VitC) in liver and used for exploring redox reaction in vivo.³⁹ Wilson et al. induced a NASH animal model with methionine-choline deficient (MCD) diet and then intravenously injected HP ^{13}C labeled DHA in them.⁴⁰ In relative to control group, a 49% reduction in the ratio of DHA to VitC was observed in mice with MCD diet, accompanied by hepatic fat deposition. Notably, the alterations in metabolic ratios returned to baseline when placing the previous MCD animals on a normal diet for one week. Even though the exact metabolic and catalytic process can be difficult to identify under the complexity of the intracellular redox network, there is no doubt that HP ^{13}C MRI have broadened the current knowledge of NASH-related metabolic abnormalities, which could possibly introduce novel therapeutic chances in near future.

5.5.2 Liver Malignancy

Detection of Early HCC

Typical hepatocarcinogenesis is considered as a stepwise development, from regenerative nodules, to dysplastic nodules and early HCC, and finally to overt HCC.⁴¹ This multistep progression is accompanied by morphological, histopathological and hemodynamic changes, as well as altered metabolism.⁴²⁻⁴⁴ However, since a majority of HCCs arise in the cirrhotic background, which consists of a heterogeneous structure and displays as multiple mass-like nodules,⁴⁵ the detection of small or early HCC can be extremely challenging with conventional imaging modalities, making metabolic imaging a potential tool in this regard. By investigating an animal model of *Myc* gene-driven liver cancer with HP ¹³C MRI, Hu et al. found that tumor metabolic alterations preceded any observable morphological and histological changes.⁴⁶ More specifically, their findings showed a significant increase in the conversion of pyruvate to alanine in pretumor tissues, which was absent in either normal tissues or established tumors, and they also indicated the precancerous regions with the most abundant alanine signal tended to eventually develop into tumors. In clinical scenarios, most HCC patients are diagnosed at an advanced stage and have limited treatment options, therefore, these promising results of HP ¹³C MRI in HCC early detection are of great importance, which provides the possibility of capturing early tumorigenesis and identifying it before tumor formation.

Consistent with prior knowledge of the Warburg effect that cancer cells prefer glycolysis rather than oxidative metabolism despite the adequate oxygen supply,⁴⁷ HCC is characterized by increased flux of pyruvate to lactate, which can be readily detected by HP ¹³C MRI.^{46,48} Moreover, significant alanine production was also noted in HCC cells and animal model with implanted Morris hepatoma in a study from Darpolor et al.⁴⁹ They reported increased lactate and alanine in tumor tissues, and attributed these changes to elevated LDH and ALT activity. Interestingly, the conversion from pyruvate to alanine significantly superseded that of pyruvate to lactate in their study, which was in

good agreement with a previous literature with same animal model.⁵⁰ However, controversial results were demonstrated in studies with different animal models⁴⁶ or different tumor implanted locations,⁴⁸ showing higher lactate signal than alanine in tumor tissues, which may have been due to the difference in tumor growth microenvironment and vascularization. Thus, although these metabolic signatures from HP ¹³C MRI may help to unveil the underlying mechanisms of HCC development, and facilitate tumor detection and differential diagnosis, metabolic aberrations in patients with primary liver malignancy remains unknown and requires extended investigations in the future.

More recently, new HP ¹³C probe, [1,3-¹³C₂]ethyl acetoacetate (EAA), has been reported feasible in imaging the metabolism in rats with implanted HCC.⁵¹ It is generally acknowledged that the concentrations and activities of carboxylesterases, an enzyme that turn EAA to acetoacetate (AA), are lower in cancer cells compared to the corresponding normal cells.⁵² In particular, as shown by Jensen et al,⁵¹ approximately four times higher substrate-to-product signal ratio was observed in tumor tissues when compared to the surrounding healthy tissue. Furthermore, in comparison with the images from commonly used pyruvate, the contrast to noise ratio of images was significantly improved by using EAA. These findings of new metabolic biomarkers in HP ¹³C MRI are promising, because they offer an opportunity to develop novel strategies for enhancing image contrast between cancerous and normal tissues, and ultimately improving the detection of small and early cancer lesions.

Assessment of Biological Characteristics

Although most HCCs have similar imaging features, different biological characteristics do exist in HCCs, which can significantly affect treatment efficacy and prognosis.⁵³ As pyruvate and its products showed great potential in identifying tumor aggressiveness in several tumor entities,^{54,55} the various biological characteristics in HCCs could be noninvasively evaluated with the help of HP ¹³C MRI. In order to better delineate the metabolic phenotyping of HCCs and explore its correlation with tumor

biological behaviors, Bliemsrieder et al. recently conducted a sophisticated study, firstly inducing endogenous HCC in rats, and then re-implanting the extracted tumor cells in another group of nude rats.⁵⁶ Their findings showed different lactate-to-alanine signal ratios of endogenous HCCs, and higher lactate signal in re-implanted tumors derived from high lactate-to-alanine ratios tumor cells. Additionally, they suggested HCCs with high lactate-to-alanine ratios may be more aggressive, because high lactate production was reported to be associated with higher biological aggressiveness in cancers.⁵⁷ In other words, metabolic alterations detected by HP ¹³C MRI, especially glucose metabolism and lactate production, provides more insights into biological characteristics of liver malignancy, and therefore may promote the development of additional diagnostic and prognostic biomarkers.

Alternative HP ¹³C probes were also introduced in the evaluation of tumor biological characteristics.^{58,59} Previous evidence suggested that HCCs with highly proliferated properties tend to be more aggressive,⁶⁰ leading to early recurrence and poor prognosis, which makes [5-¹³C₁] glutamine a promising substrate in HP ¹³C MRI. Physiologically, glutamine can be converted to glutamate by intramitochondrial glutaminase. It plays an essential role in tumor cell metabolism and is related to cell proliferation.⁶¹ An initial study confirmed the feasibility of HP ¹³C MRI in imaging the conversion from glutamine to glutamate in human hepatoma cells,⁵⁸ which may allow for the assessment of tumor proliferation and the prediction of prognosis in patients with HCC in the future. Apart from metabolically active HP ¹³C substrates, inactive agents, such as [¹³C]urea, can be possibly used for assessing biological characteristics in liver malignancy with its promising results in perfusion imaging.^{62,63} Von Morze et al. found significant differences in regional perfusion characteristics in cancerous tissues by injecting HP [¹³C] urea in a preclinical HCC model.⁵⁹ In particular, a 19% reduction in mean blood flow was observed in tumors, whereas 26% elevation was found in the tumor rim. These results and the described method were clinically relevant, because tumors typically exhibit

altered blood flow and perfusion patterns due to abnormal neovascularization. Therefore, with the obtained perfusion information by HP ^{13}C MRI, researchers could probably predict the biological behaviors of HCC, and patients may finally benefit from individual pre-therapeutic tumor assessment.

Evaluation of Treatment Response

Unresectable HCCs are usually recommended for loco-regional treatment, including trans-arterial embolization (TAE) with or without chemo drugs, or systemic therapy.⁶⁴ Nevertheless, frequent local recurrence and metastasis after treatment can be problematic in refractory HCCs, which results in poor overall survival and high mortality in patients.⁴ Current imaging paradigms mostly provide information on tumor volume and vascularity for the assessment of treatment efficacy,⁶⁵ which fails to detect the latent tumor cells and emphasizes the need for advanced metabolic imaging methods, such as HP ^{13}C MRI. Recently, Perkons and his colleagues found that latent HCC cells activated metabolic reprogramming to survive TAE induced ischemia.¹³ Notably, decreased anabolism and increased lactate production were observed in latent HCC undergoing TAE induced ischemia both in vitro and in vivo. In addition, as illustrated in the representative images in their study, conventional proton imaging failed to detect viable tumor cells with absent contrast enhancement, while HP ^{13}C MRI enabled the direct detection of persistent metabolism in surviving HCC cells at the tumor periphery. Together, these inspiring findings hold significant implications for evaluating therapeutic response and guiding subsequent interventions in patients with unresectable HCC, and help to improve their clinical outcomes.

Pathologically, necrosis is usually the consequence of embolizing feeding hepatic arteries and depriving tumors from nutrients in TAE treatment, which can be easily detected by using another HP ^{13}C probe, [1,4- $^{13}\text{C}_2$]fumarate. In general, the conversion rate and concentration of fumarate and its metabolite (i.e., malate) would rapidly change when the tumor cells are in a necrotic condition without

intact membrane.⁶⁶ To simultaneously collect the information about tumor metabolism, perfusion and necrosis after TAE therapy, Düwel et al. performed a HP ¹³C MRI experiment with multiple HP substrates, including pyruvate, urea and fumarate, in a rat model with orthotopic HCC.¹⁴ As expected on TAE treatment, decreased urea and pyruvate signals, as well as an increased apparent conversion rate from pyruvate to lactate were observed in their study, indicating reduced perfusion and increased hypoxic glycolysis. Furthermore, there was a significant elevation of malate after embolization, and the ratio of total malate to total fumarate greatly correlated with the histological necrosis level, with correlation coefficient of 0.86. Hence, when integrating various information provided by different ¹³C probes, HP ¹³C MRI may be able to assess the treatment efficacy of HCC and identify beneficiary patient cohort for specific treatments, and even aid the development of novel therapeutic concepts.

Given the close relationship between pharmacologic action of chemotherapy and metabolic pathways, it is possible to utilize HP ¹³C MRI to evaluate chemotherapeutic response of liver malignancy. A recent pilot study investigated the dynamic metabolism in a prostate cancer patient with liver metastasis before and after chemotherapy.¹⁵ As shown in their research, the pyruvate-to-lactate conversion rate of the metastatic liver lesion decreased from 0.026 to 0.015 s⁻¹ (42% reduction), and the tumor size reduced from 19.3mm to 11.8mm (39% reduction) two months after the initiation of chemotherapy. In addition, Cabella et al.⁶⁷ proposed a novel preparation method for HP [5-¹³C] glutamine and confirmed its ability in measuring the response to chemotherapy in HCC cells. In light of these findings, HP ¹³C MRI may become the solution to current unmet clinical dilemma of liver cancer, which can be especially helpful in guiding the development of new chemotherapeutic and targeted drugs, and acting as a robust biomarker in longitudinal follow-up trails.

5.6 Future Opportunities

HP ^{13}C MRI provides a fundamentally new way of looking at patients with liver diseases. By identifying intracellular metabolism, we can expect to better understand the biology of diffuse liver diseases and therefore better manage them. These specific metabolic markers can be the noninvasive surrogate in monitoring the disease progression and assessing therapeutic response. As for liver malignancies, the information on downstream metabolism offers the possibility of detecting early HCC before observable morphological changes, and understanding its pathogenic mechanism. Such metabolic biomarkers can also help assess biological behaviors of tumors and aid personalized treatment strategies. For example, the metabolic alterations in tumor and peritumoral parenchyma may guide surgeons to determine the actual resected areas. In addition, based on the previous findings, HP ^{13}C MRI can be a powerful tool in evaluating the treatment efficacy and predicting the clinical outcomes of patients. Despite the encouraging results and great potential of this technique in both diffuse and focal liver diseases, further research is still warranted to optimize the workflow.

Continuing works on the imaging hardware and acquisition sequences are needed to improve the sensitivity of HP ^{13}C MRI and increase its clinical applicability. Besides the development and technical improvements of dual-tuned $^1\text{H}/^{13}\text{C}$ volume coils for abdominal organs, works on receive surface coils with short coil-to-sample distance and optimal coil combinations are currently ongoing.^{68,69} Additionally, in order to further prevent signal loss and capture rapid metabolic conversion without significant motion artifacts, new fast acquisition is required to obtain volumetric and dynamic HP MR data of the liver, preferably towards whole liver coverage, sub-centimeter spatial resolution and higher temporal resolution (e.g. 1 second for pyruvate and 3 seconds for its metabolites). With the combination of parallel imaging technique, compress sensing and spiral trajectories,⁷⁰ it is believed that current acquisition methods will advance to these expectations in the near future. More recently, a novel post-processing pipeline was proposed to reduce background noise

in HP spectra and increase the accuracy of kinetic estimations in patients with liver tumors,⁷¹ emphasizing the needs for new analysis techniques with improved spectral SNR and more accurate measurements.

In view of the heterogeneous nature of liver diseases, especially liver malignancies, the combination of HP ¹³C MRI with multiphasic and multiparametric ¹H imaging, as well as multimodal findings could be of great significance for personalized medicine in the future. For example, the liver-specific gadolinium contrast-agent can not only provide valuable multiphasic information about haemodynamic changes, but also selectively suppress normal hepatocyte contributions to hyperpolarized ¹³C MRI signal, which could be applied to separate the metabolic signals arising from the small tumors and surrounding normal hepatocytes.⁷² On the other hand, a multiparametric imaging approach with both HP ¹³C MRI and diffusional or other functional sequences is anticipated to monitor the therapeutic effects in liver diseases.^{10,29,73} Besides, the combination of HP ¹³C MRI and PET was shown promise in a rat model with HCC.⁴⁸ This multimodal technique was named as HyperPET,⁷⁴ and it is believed to provide complementary information and allow for better evaluation of the biological behaviors and treatment response in liver cancers.

In addition to the widely investigated pyruvate, a number of different ¹³C substrates have been proposed and tested promising in the liver, including earlier mentioned DHA, EAA, glutamine, urea and fumarate, as well as dihydroxyacetone,^{75,76} alanine⁷⁷ and several others^{78,79} (Table 5.3), providing further details on the metabolism under different hepatic pathologies. As reported, dihydroxyacetone is sensitive to dysregulation of hepatic gluconeogenesis and glycolysis,^{75,76} and may be used to investigate metabolic diseases such as NAFLD or cirrhosis in a noninvasive manner. Furthermore, alanine has a potential role in measuring hepatic redox reaction, which could be utilized in the evaluation of liver damage.⁷⁷ Moreover, simultaneous co-polarization and co-injection of multiple compounds was recently shown feasible in a preclinical HCC model.¹⁴ This is significant because it

enables the assessment of several cellular processes at the same time and optimizes the workflow, and could possibly become a future research direction. Further work with higher and faster polarizations and simplified delivery of sterile HP probes are also needed to facilitate the clinical adoption of this technique.

Table 5.3. Established and promising hyperpolarized ^{13}C probes in liver diseases.

Molecule	Pathways/functions	Possible applications	References
[1- ^{13}C]pyruvate	Glycolysis and ALT, LDH, PDH activity	Diffuse liver diseases and liver cancers	10–15, 24, 25, 29, 34, 35, 46, 48–50, 56
[1- ^{13}C]dehydroascorbic acid	Redox status	Liver injury and NASH	40
[1,3- $^{13}\text{C}_2$]ethyl acetoacetate	Carboxylesterase activity	Liver cancers	51
[5- ^{13}C]glutamine	Glutaminolysis, cellular proliferation	Liver cancers	58, 67
[^{13}C]urea or [^{13}C , $^{15}\text{N}_2$]urea	Perfusion	Liver fibrosis and liver cancers	14, 59
[1-4- $^{13}\text{C}_2$]fumarate	Cellular necrosis	Liver cancers	14
[2- ^{13}C]dihydroxyacetone	Gluconeogenesis	NAFLD	75, 76
[1- ^{13}C]alanine	Redox status	Liver injury and NASH	77
[1- ^{13}C , U- $^2\text{H}_5$]ethanol	Aldehyde dehydrogenase activity	Alcoholic liver disease and liver cancers	78
[1- ^{13}C]-L-lactate	Pyruvate carboxylase activity	NAFLD	79

Abbreviations: ALT, alanine transaminase; LDH, lactate dehydrogenase; NAFLD, non-alcoholic fatty liver disease; NASH, non-alcoholic steatohepatitis; PDH, pyruvate dehydrogenase.

Last but not least, extended preclinical studies of liver metabolism are still needed to bridge the translational gap of HP ^{13}C MRI. Currently, there is an ongoing clinical trial aiming to explore the effect of nutritional state and fatty liver on TCA cycle in healthy subjects and patients with fatty liver diseases by using HP ^{13}C pyruvate injection.⁸⁰ Nevertheless, due to the limited human studies in real clinical scenarios, multicenter trials are necessary to better standardize this technique and improve its robustness, reliability, and efficiency.⁷ Hopefully, with the help of multiple collaborations, HP ^{13}C MRI can be integrated as a short (5-minute) add-on into the routine MRI examination in the coming future.

5.7 Conclusions

HP ^{13}C MRI is an emerging and promising technique in both diffuse liver diseases and liver malignancies. It allows for real time visualization of hepatic metabolism and enzymatic conversions, and is of significant potential in detecting liver diseases, monitoring its progression and assessing the treatment efficacy. There are still unresolved barriers of this technique on the road to clinical transformation, but it also brings future research opportunities in this field. With the improvement of this technique and optimization of the workflow, HP ^{13}C MRI is expected to become a powerful tool for the diagnosis and management of liver diseases in clinical practice.

5.8 References

1. Adeva-Andany MM, Pérez-Felpete N, Fernández-Fernández C, Donapetry-García C, Pazos-García C. Liver glucose metabolism in humans. *Biosci Rep*. 2016;36(6). doi:10.1042/BSR20160385
2. Chen Z, Tian R, She Z, Cai J, Li H. Role of oxidative stress in the pathogenesis of nonalcoholic fatty liver disease. *Free Radic Biol Med*. 2020;152:116-141. doi:10.1016/j.freeradbiomed.2020.02.025
3. Ray K. NAFLD—the next global epidemic. *Nat Rev Gastroenterol Hepatol*. 2013;10(11):621-621. doi:10.1038/nrgastro.2013.197
4. Bertuccio P, Turati F, Carioli G, et al. Global trends and predictions in hepatocellular carcinoma mortality. *J Hepatol*. 2017;67(2):302-309. doi:10.1016/j.jhep.2017.03.011
5. Torre LA, Bray F, Siegel RL, Ferlay J, Lortet-Tieulent J, Jemal A. Global cancer statistics, 2012. *CA Cancer J Clin*. 2015;65(2):87-108. doi:10.3322/caac.21262
6. Regev A, Berho M, Jeffers LJ, et al. Sampling error and intraobserver variation in liver biopsy in patients with chronic HCV infection. *Am J Gastroenterol*. 2002;97(10):2614-2618. doi:10.1111/j.1572-0241.2002.06038.x
7. Wang ZJ, Ohliger MA, Larson PEZ, et al. Hyperpolarized ¹³C MRI: State of the art and future directions. *Radiology*. 2019;291(2):273-284. doi:10.1148/radiol.2019182391
8. Kurhanewicz J, Vigneron DB, Ardenkjaer-Larsen JH, et al. Hyperpolarized ¹³C MRI: Path to Clinical Translation in Oncology. *Neoplasia (United States)*. 2019;21(1):1-16. doi:10.1016/j.neo.2018.09.006
9. Knowles BR, Friedrich F, Fischer C, Paech D, Ladd ME. Beyond T2 and 3T: New MRI techniques for clinicians. *Clin Transl Radiat Oncol*. 2019;18:87-97. doi:10.1016/j.ctro.2019.04.009

10. Moon CM, Shin SS, Heo SH, et al. Metabolic Changes in Different Stages of Liver Fibrosis: In vivo Hyperpolarized ¹³C MR Spectroscopy and Metabolic Imaging. *Mol Imaging Biol.* 2019;21(5):842-851. doi:10.1007/s11307-019-01322-9
11. Smith LM, Pitts CB, Friesen-Waldner LJ, et al. In Vivo Magnetic Resonance Spectroscopy of Hyperpolarized [1-¹³C]Pyruvate and Proton Density Fat Fraction in a Guinea Pig Model of Non-Alcoholic Fatty Liver Disease Development After Life-Long Western Diet Consumption. *J Magn Reson Imaging.* 2021;54(5):1404-1414. doi:10.1002/jmri.27677
12. Lee P, Leong W, Tan T, Lim M, Han W, Radda GK. In Vivo hyperpolarized carbon-13 magnetic resonance spectroscopy reveals increased pyruvate carboxylase flux in an insulin-resistant mouse model. *Hepatology.* 2013;57(2):515-524. doi:10.1002/hep.26028
13. Perkons NR, Kiefer RM, Noji MC, et al. Hyperpolarized Metabolic Imaging Detects Latent Hepatocellular Carcinoma Domains Surviving Locoregional Therapy. *Hepatology.* 2020;72(1):140-154. doi:10.1002/hep.30970
14. Düwel S, Durst M, Gringeri C V., et al. Multiparametric human hepatocellular carcinoma characterization and therapy response evaluation by hyperpolarized ¹³C MRSI. *NMR Biomed.* 2016;29(7):952-960. doi:10.1002/nbm.3561
15. Chen HY, Aggarwal R, Bok RA, et al. Hyperpolarized ¹³C-pyruvate MRI detects real-time metabolic flux in prostate cancer metastases to bone and liver: a clinical feasibility study. *Prostate Cancer Prostatic Dis.* 2020;23(2):269-276. doi:10.1038/s41391-019-0180-z
16. Khomich O, Ivanov A V., Bartosch B. Metabolic Hallmarks of Hepatic Stellate Cells in Liver Fibrosis. *Cells.* 2019;9(1):24. doi:10.3390/cells9010024
17. Lu Q, Tian X, Wu H, et al. Metabolic Changes of Hepatocytes in NAFLD. *Front Physiol.* 2021;12. doi:10.3389/fphys.2021.710420
18. De Matteis S, Ragusa A, Marisi G, et al. Aberrant Metabolism in Hepatocellular Carcinoma

- Provides Diagnostic and Therapeutic Opportunities. *Oxid Med Cell Longev*. 2018;2018:1-13.
doi:10.1155/2018/7512159
19. Ardenkjær-Larsen JH, Golman K, Gram A, et al. Increase of signal-to-noise of more than 10,000 times in liquid state NMR. *Discov Med*. 2003;100(18):10158-10163.
 20. Larson PEZ, Gordon JW. Hyperpolarized Metabolic MRI—Acquisition, Reconstruction, and Analysis Methods. *Metabolites*. 2021;11(6):386. doi:10.3390/metabo11060386
 21. Louvet A, Mathurin P. Alcoholic liver disease: mechanisms of injury and targeted treatment. *Nat Rev Gastroenterol Hepatol*. 2015;12(4):231-242. doi:10.1038/nrgastro.2015.35
 22. Stine JG, Chalasani N. Chronic liver injury induced by drugs: a systematic review. *Liver Int*. 2015;35(11):2343-2353. doi:10.1111/liv.12958
 23. Zhao R-H, Shi Y, Zhao H, Wu W, Sheng J-F. Acute-on-chronic liver failure in chronic hepatitis B: an update. *Expert Rev Gastroenterol Hepatol*. 2018;12(4):341-350.
doi:10.1080/17474124.2018.1426459
 24. Josan S, Billingsley K, Orduna J, et al. Assessing inflammatory liver injury in an acute CCl₄ model using dynamic 3D metabolic imaging of hyperpolarized [1-¹³C]pyruvate. *NMR Biomed*. 2015;28(12):1671-1677. doi:10.1002/nbm.3431
 25. Kim G-W, Oh C-H, Kim J-C, et al. Noninvasive biomarkers for acute hepatotoxicity induced by 1,3-dichloro-2-propanol: hyperpolarized ¹³C dynamic MR spectroscopy. *Magn Reson Imaging*. 2016;34(2):159-165. doi:10.1016/j.mri.2015.10.023
 26. Bahde R, Spiegel H-U. Hepatic ischaemia–reperfusion injury from bench to bedside. *Br J Surg*. 2010;97(10):1461-1475. doi:10.1002/bjs.7176
 27. Peralta C, Jiménez-Castro MB, Gracia-Sancho J. Hepatic ischemia and reperfusion injury: Effects on the liver sinusoidal milieu. *J Hepatol*. 2013;59(5):1094-1106.
doi:10.1016/j.jhep.2013.06.017

28. Lanitis S, Lolis E, Dafnios N, Sgourakis G, Voros DC, Vassiliou I. The effect of warm liver ischaemia & reperfusion injury on circulating plasma lipid levels & lipolytic enzyme activity in rat & the impact of ischaemic preconditioning. *Indian J Med Res.* 2012;136(2):272-279. <http://www.ncbi.nlm.nih.gov/pubmed/22960895>
29. Moon C-M, Shin S-S, Lim N-Y, et al. Metabolic alterations in a rat model of hepatic ischaemia reperfusion injury: In vivo hyperpolarized ¹³C MRS and metabolic imaging. *Liver Int.* 2018;38(6):1117-1127. doi:10.1111/liv.13695
30. Wang S, Friedman SL. Hepatic fibrosis: A convergent response to liver injury that is reversible. *J Hepatol.* 2020;73(1):210-211. doi:10.1016/j.jhep.2020.03.011
31. Roehlen N, Crouchet E, Baumert TF. Liver Fibrosis: Mechanistic Concepts and Therapeutic Perspectives. *Cells.* 2020;9(4):875. doi:10.3390/cells9040875
32. Ye Z, Wei Y, Chen J, Yao S, Song B. Value of intravoxel incoherent motion in detecting and staging liver fibrosis: A meta-analysis. *World J Gastroenterol.* 2020;26(23):3304-3317. doi:10.3748/wjg.v26.i23.3304
33. Rinella ME, Sanyal AJ. Management of NAFLD: a stage-based approach. *Nat Rev Gastroenterol Hepatol.* 2016;13(4):196-205. doi:10.1038/nrgastro.2016.3
34. Kim G-W, Ahn K-Y, Kim Y-H, Jeong G-W. Time-course metabolic changes in high-fat diet-induced obesity rats: A pilot study using hyperpolarized ¹³C dynamic MRS. *Magn Reson Imaging.* 2016;34(8):1199-1205. doi:10.1016/j.mri.2016.06.002
35. Moon CM, Oh CH, Ahn KY, et al. Metabolic biomarkers for non-alcoholic fatty liver disease induced by high-fat diet: In vivo magnetic resonance spectroscopy of hyperpolarized [1-¹³C] pyruvate. *Biochem Biophys Res Commun.* 2017;482(1):112-119. doi:10.1016/j.bbrc.2016.08.118
36. Tilg H, Moschen AR, Roden M. NAFLD and diabetes mellitus. *Nat Rev Gastroenterol Hepatol.* 2017;14(1):32-42. doi:10.1038/nrgastro.2016.147

37. Eslam M, Sanyal AJ, George J, et al. MAFLD: A Consensus-Driven Proposed Nomenclature for Metabolic Associated Fatty Liver Disease. *Gastroenterology*. 2020;158(7):1999-2014.e1. doi:10.1053/j.gastro.2019.11.312
38. Ratziu V, Goodman Z, Sanyal A. Current efforts and trends in the treatment of NASH. *J Hepatol*. 2015;62(1):S65-S75. doi:10.1016/j.jhep.2015.02.041
39. Keshari KR, Kurhanewicz J, Bok R, Larson PEZ, Vigneron DB, Wilson DM. Hyperpolarized ¹³C dehydroascorbate as an endogenous redox sensor for in vivo metabolic imaging. *Proc Natl Acad Sci*. 2011;108(46):18606-18611. doi:10.1073/pnas.1106920108
40. Wilson DM, Di Gialleonardo V, Wang ZJ, et al. Hyperpolarized ¹³C spectroscopic evaluation of oxidative stress in a rodent model of steatohepatitis. *Sci Rep*. 2017;7(46014):1-7. doi:10.1038/srep46014
41. Craig AJ, von Felden J, Garcia-Lezana T, Sarcognato S, Villanueva A. Tumour evolution in hepatocellular carcinoma. *Nat Rev Gastroenterol Hepatol*. 2020;17(3):139-152. doi:10.1038/s41575-019-0229-4
42. Kudo M. Multistep human hepatocarcinogenesis: correlation of imaging with pathology. *J Gastroenterol*. 2009;44(S19):112-118. doi:10.1007/s00535-008-2274-6
43. Tan Y, Yin P, Tang L, et al. Metabolomics Study of Stepwise Hepatocarcinogenesis From the Model Rats to Patients: Potential Biomarkers Effective for Small Hepatocellular Carcinoma Diagnosis. *Mol Cell Proteomics*. 2012;11(2):M111.010694. doi:10.1074/mcp.M111.010694
44. Ribback S, Calvisi DF, Cigliano A, et al. Molecular and metabolic changes in human liver clear cell foci resemble the alterations occurring in rat hepatocarcinogenesis. *J Hepatol*. 2013;58(6):1147-1156. doi:10.1016/j.jhep.2013.01.013
45. Park YN, Kim M-J. Hepatocarcinogenesis: imaging-pathologic correlation. *Abdom Imaging*. 2011;36(3):232-243. doi:10.1007/s00261-011-9688-y

46. Hu S, Balakrishnan A, Bok RA, et al. ¹³C-pyruvate imaging reveals alterations in glycolysis that precede c-Myc-induced tumor formation and regression. *Cell Metab.* 2011;14(1):131-142. doi:10.1016/j.cmet.2011.04.012
47. Vander Heiden MG, Cantley LC, Thompson CB. Understanding the Warburg Effect: The Metabolic Requirements of Cell Proliferation. *Science (80-)*. 2009;324(5930):1029-1033. doi:10.1126/science.1160809
48. Menzel MI, Farrell E V., Janich MA, et al. Multimodal Assessment of In Vivo Metabolism with Hyperpolarized [¹⁻¹³C]MR Spectroscopy and ¹⁸F-FDG PET Imaging in Hepatocellular Carcinoma Tumor-Bearing Rats. *J Nucl Med.* 2013;54(7):1113-1119. doi:10.2967/jnumed.112.110825
49. Darpolor MM, Yen Y-F, Chua M-S, et al. In vivo MRSI of hyperpolarized [¹⁻¹³C]pyruvate metabolism in rat hepatocellular carcinoma. *NMR Biomed.* 2011;24(5):506-513. doi:10.1002/nbm.1616
50. Yen Y-F, Le Roux P, Mayer D, et al. T₂ relaxation times of ¹³C metabolites in a rat hepatocellular carcinoma model measured in vivo using ¹³C-MRS of hyperpolarized [¹⁻¹³C]pyruvate. *NMR Biomed.* Published online 2010:n/a-n/a. doi:10.1002/nbm.1481
51. Jensen PR, Serra SC, Miragoli L, et al. Hyperpolarized [1,3-¹³C₂]ethyl acetoacetate is a novel diagnostic metabolic marker of liver cancer. *Int J Cancer.* 2015;136(4):E117-E126. doi:10.1002/ijc.29162
52. Na K, Lee E-Y, Lee H-J, et al. Human plasma carboxylesterase 1, a novel serologic biomarker candidate for hepatocellular carcinoma. *Proteomics.* 2009;9(16):3989-3999. doi:10.1002/pmic.200900105
53. Vasuri F, Renzulli M, Fittipaldi S, et al. Pathobiological and Radiological Approach For Hepatocellular Carcinoma Subclassification. *Sci Rep.* 2019;9(1):14749. doi:10.1038/s41598-

- 019-51303-9
54. Bidkhorji G, Benfeitas R, Klevstig M, et al. Metabolic network-based stratification of hepatocellular carcinoma reveals three distinct tumor subtypes. *Proc Natl Acad Sci*. 2018;115(50). doi:10.1073/pnas.1807305115
 55. Gallagher FA, Woitek R, McLean MA, et al. Imaging breast cancer using hyperpolarized carbon-13 MRI. *Proc Natl Acad Sci U S A*. 2020;117(4):2092-2098. doi:10.1073/pnas.1913841117
 56. Bliemsrieder E, Kaissis G, Grashei M, et al. Hyperpolarized ¹³C pyruvate magnetic resonance spectroscopy for in vivo metabolic phenotyping of rat HCC. *Sci Rep*. 2021;11(1):1191. doi:10.1038/s41598-020-80952-4
 57. Walenta S, Wetterling M, Lehrke M, et al. High lactate levels predict likelihood of metastases, tumor recurrence, and restricted patient survival in human cervical cancers. *Cancer Res*. 2000;60(4):916-921. <http://www.ncbi.nlm.nih.gov/pubmed/10706105>
 58. Gallagher FA, Kettunen MI, Day SE, Lerche M, Brindle KM. ¹³C MR spectroscopy measurements of glutaminase activity in human hepatocellular carcinoma cells using hyperpolarized ¹³C-labeled glutamine. *Magn Reson Med*. 2008;60(2):253-257. doi:10.1002/mrm.21650
 59. von Morze C, Larson PEZ, Hu S, et al. Imaging of blood flow using hyperpolarized [¹³C]Urea in preclinical cancer models. *J Magn Reson Imaging*. 2011;33(3):692-697. doi:10.1002/jmri.22484
 60. Ye Z, Cao L, Wei Y, et al. Preoperative prediction of hepatocellular carcinoma with highly aggressive characteristics using quantitative parameters derived from hepatobiliary phase MR images. *Ann Transl Med*. 2020;8(4):85-85. doi:10.21037/atm.2020.01.04
 61. Bode BP, Fuchs BC, Hurley BP, et al. Molecular and functional analysis of glutamine uptake

- in human hepatoma and liver-derived cells. *Am J Physiol Liver Physiol.* 2002;283(5):G1062-G1073. doi:10.1152/ajpgi.00031.2002
62. Johansson E, Månsson S, Wirestam R, et al. Cerebral perfusion assessment by bolus tracking using hyperpolarized ^{13}C . *Magn Reson Med.* 2004;51(3):464-472. doi:10.1002/mrm.20013
63. Qin H, Tang S, Riselli AM, et al. Clinical translation of hyperpolarized ^{13}C pyruvate and urea MRI for simultaneous metabolic and perfusion imaging. *Magn Reson Med.* 2022;87(1):138-149. doi:10.1002/mrm.28965
64. Llovet JM, Kelley RK, Villanueva A, et al. Hepatocellular carcinoma. *Nat Rev Dis Prim.* 2021;7(1):6. doi:10.1038/s41572-020-00240-3
65. Forner A, Ayuso C, Varela M, et al. Evaluation of tumor response after locoregional therapies in hepatocellular carcinoma. *Cancer.* 2009;115(3):616-623. doi:10.1002/cncr.24050
66. Gallagher FA, Kettunen MI, Hu D-E, et al. Production of hyperpolarized [1,4- ^{13}C 2]malate from [1,4- ^{13}C 2]fumarate is a marker of cell necrosis and treatment response in tumors. *Proc Natl Acad Sci.* 2009;106(47):19801-19806. doi:10.1073/pnas.0911447106
67. Cabella C, Karlsson M, Canapè C, et al. In vivo and in vitro liver cancer metabolism observed with hyperpolarized [5- ^{13}C]glutamine. *J Magn Reson.* 2013;232:45-52. doi:10.1016/j.jmr.2013.04.010
68. Zhu Z, Zhu X, Ohliger MA, et al. Coil combination methods for multi-channel hyperpolarized ^{13}C imaging data from human studies. *J Magn Reson.* 2019;301:73-79. doi:10.1016/j.jmr.2019.01.015
69. Sánchez-Heredia JD, Baron R, Hansen ESS, Laustsen C, Zhurbenko V, Ardenkjær-Larsen JH. Autonomous cryogenic RF receive coil for ^{13}C imaging of rodents at 3 T. *Magn Reson Med.* 2020;84(1):497-508. doi:10.1002/mrm.28113
70. Gordon JW, Chen H, Dwork N, Tang S, Larson PEZ. Fast Imaging for Hyperpolarized MR

- Metabolic Imaging. *J Magn Reson Imaging*. 2021;53(3):686-702. doi:10.1002/jmri.27070
71. Lee PM, Chen HY, Gordon JW, et al. Specialized computational methods for denoising, B1 correction, and kinetic modeling in hyperpolarized ^{13}C MR EPSI studies of liver tumors. *Magn Reson Med*. 2021;86(5):2402-2411. doi:10.1002/mrm.28901
 72. Ohliger MA, von Morze C, Marco-Rius I, et al. Combining hyperpolarized ^{13}C MRI with a liver-specific gadolinium contrast agent for selective assessment of hepatocyte metabolism. *Magn Reson Med*. 2017;77(6):2356-2363. doi:10.1002/mrm.26296
 73. Marco-Rius I, Gordon JW, Mattis AN, et al. Diffusion-weighted imaging of hyperpolarized [^{13}C]urea in mouse liver. *J Magn Reson Imaging*. 2018;47(1):141-151. doi:10.1002/jmri.25721
 74. Gutte H, Hansen AE, Larsen MME, et al. Simultaneous Hyperpolarized ^{13}C -Pyruvate MRI and ^{18}F -FDG PET (HyperPET) in 10 Dogs with Cancer. *J Nucl Med*. 2015;56(11):1786-1792. doi:10.2967/jnumed.115.156364
 75. Marco-Rius I, Wright AJ, Hu D, et al. Probing hepatic metabolism of [^{13}C]dihydroxyacetone in vivo with ^1H -decoupled hyperpolarized ^{13}C -MR. *Magn Reson Mater Physics, Biol Med*. 2021;34(1):49-56. doi:10.1007/s10334-020-00884-y
 76. Marco-Rius I, von Morze C, Sriram R, et al. Monitoring acute metabolic changes in the liver and kidneys induced by fructose and glucose using hyperpolarized [^{13}C]dihydroxyacetone. *Magn Reson Med*. 2017;77(1):65-73. doi:10.1002/mrm.26525
 77. Park JM, Khemtong C, Liu S, Hurd RE, Spielman DM. In vivo assessment of intracellular redox state in rat liver using hyperpolarized [^{13}C]Alanine. *Magn Reson Med*. 2017;77(5):1741-1748. doi:10.1002/mrm.26662
 78. Dzien P, Kettunen MI, Marco-Rius I, et al. ^{13}C magnetic resonance spectroscopic imaging of hyperpolarized [^{13}C , ^2H] ethanol oxidation can be used to assess aldehyde dehydrogenase activity in vivo. *Magn Reson Med*. 2015;73(5):1733-1740.

doi:10.1002/mrm.25286

79. Chen J, Hackett EP, Kovacs Z, Malloy CR, Park JM. Assessment of hepatic pyruvate carboxylase activity using hyperpolarized [1- ¹³C]-1 -lactate. *Magn Reson Med*. 2021;85(3):1175-1182. doi:10.1002/mrm.28489
80. Malloy CR. Effect of Fatty Liver on TCA Cycle Flux and the Pentose Phosphate Pathway (HPFFF). ClinicalTrials.gov. Published 2021.
<https://clinicaltrials.gov/ct2/show/NCT03480594>

Chapter 6

Whole-Abdomen Metabolic Imaging of Healthy Volunteers Using Hyperpolarized [1-¹³C]pyruvate MRI

Lee PM, Chen HY, Gordon JW, Wang ZJ, Bok R, Hashoian R, Kim Y, Liu X, Nickles T, Cheung K, De Las Alas F, Daniel H, Larson PEZ, Von Morze C, Vigneron DB, and Ohliger MA. Whole-Abdomen Metabolic Imaging of Healthy Volunteers Using Hyperpolarized [1-¹³C]pyruvate MRI. *Journal of Magnetic Resonance Imaging*. April 2022. DOI: 0.1002/jmri.28196.

6.1 Abstract

6.1.1 Background

Hyperpolarized ^{13}C MRI quantitatively measures enzyme-catalyzed metabolism in cancer and metabolic diseases. Whole-abdomen imaging will permit dynamic metabolic imaging of several abdominal organs simultaneously in healthy and diseased subjects.

6.1.2 Purpose

Image hyperpolarized $[1-^{13}\text{C}]$ pyruvate and products in the abdomens of healthy volunteers, overcoming challenges of motion, magnetic field variations, and spatial coverage. Compare hyperpolarized $[1-^{13}\text{C}]$ pyruvate metabolism across abdominal organs of healthy volunteers.

6.1.3 Study Type

Prospective technical development.

6.1.4 Subjects

13 healthy volunteers (8 male), 21-64 years (median 36).

6.1.5 Field Strength/Sequence

3T. Proton: T_1 -weighted spoiled gradient echo, T_2 -weighted single-shot fast spin echo, multi-echo fat/water imaging. Carbon-13: echo-planar spectroscopic imaging, metabolite-specific echo-planar imaging.

6.1.6 Assessment

Transmit magnetic field was measured. Variations in main magnetic field (ΔB_0) determined using multi-echo proton acquisitions were compared to carbon-13 acquisitions. Changes in ΔB_0 were measured after localized shimming. Improvements in metabolite signal-to-noise ratio were calculated. Whole-organ regions of interests were drawn over the liver, spleen, pancreas, and kidneys by a single investigator. Metabolite signals, time-to-peak, decay times, and mean first-order rate constants for pyruvate-to-lactate (k_{PL}) and alanine (k_{PA}) conversion were measured in each organ.

6.1.7 Statistical Tests

Linear regression, one-sample Kolmogorov-Smirnov tests, paired t -tests, one-way ANOVA, Tukey's multiple comparisons tests. $P \leq 0.05$ considered statistically significant.

6.1.8 Results

Proton ΔB_0 maps correlated with carbon-13 ΔB_0 maps (slope=0.93, y-intercept=-2.88, $R^2=0.73$, $P < 0.0001$). Localized shimming resulted in mean frequency offset within ± 25 Hz for all organs. Metabolite SNR increased after denoising ($P < 0.0001$). Mean k_{PL} and k_{PA} were highest in liver, followed by pancreas, spleen, and kidneys (all comparisons with liver $P \leq 0.0022$).

6.1.9 Data Conclusion

Whole-abdomen coverage with hyperpolarized carbon-13 MRI was feasible despite technical challenges. Multi-echo gradient echo ^1H acquisitions accurately predicted chemical shifts observed using carbon-13 spectroscopy. Carbon-13 acquisitions benefited from local shimming. Metabolite

energetics in the abdomen compiled for healthy volunteers can be used to design larger clinical trials in patients with metabolic diseases.

6.2 Introduction

Hyperpolarized (HP) carbon-13 (^{13}C) MRI permits rapid, dynamic, quantitative measurements of in vivo enzyme-catalyzed metabolism in humans ¹. In recent years, it has been applied in patients with cardiac diseases, cancers, and other metabolic diseases, with the goal of improved patient care and outcomes (2–12). HP ^{13}C MRI is enabled by dynamic nuclear polarization of ^{13}C -labeled compounds, such as $[1-^{13}\text{C}]$ pyruvate ¹³. Upon dissolution, HP compounds can be safely injected into human subjects while retaining an observable signal that is $\geq 10,000$ times higher than thermal values ¹.

HP $[1-^{13}\text{C}]$ pyruvate is of particular clinical relevance because pyruvate sits at the intersection of multiple major metabolic pathways that are metabolically reprogrammed in cancers and other diseases ^{14–16}. As the product of glycolysis, pyruvate is either exchanged into lactate or else into acetyl-CoA and bicarbonate prior to the tricarboxylic acid cycle. Pyruvate can also be converted to alanine via alanine amino transferase. This process leads to three potentially observable HP ^{13}C products from $[1-^{13}\text{C}]$ pyruvate: $[1-^{13}\text{C}]$ lactate, ^{13}C -bicarbonate, and $[1-^{13}\text{C}]$ alanine. Analysis and kinetic modeling can quantify the enzymatic conversion rate of pyruvate to lactate through lactate dehydrogenase (LDH) ^{1,17,18}. The apparent first-order rate constant, k_{PL} , is a potential biomarker that is elevated in cancer and reflects treatment response in animal models and in humans ^{1,2,4,19–23}. Hence, HP $[1-^{13}\text{C}]$ pyruvate MRI has seen much success in characterizing metabolism in the prostate, brain, heart, and the kidneys, and in quantifying response to therapy in multiple cancers ^{2–9,24,25}. The apparent first-order rate constant of pyruvate conversion to alanine, k_{PA} , can also be measured and quantified.

The liver is a common site of tumors and metabolic diseases including non-alcoholic fatty liver disease (NAFLD). NAFLD, which is characterized by the ectopic accumulation of fat in the liver, can progress to non-alcoholic steatohepatitis (NASH), with the risk of cirrhosis, portal hypertension, and hepatocellular carcinoma²⁶. The current gold standard for distinguishing between simple steatosis and NASH is with a biopsy. New improved methods are needed to better distinguish between simple steatosis and NASH noninvasively. Pre-clinical models of liver injury, diabetes, and fatty liver have revealed that HP ¹³C MRI is responsive to changes in liver metabolism that occur in these diseases.²⁷⁻

30

Clinical translation of these methods to benefit patients requires reliable whole-abdomen imaging methods. Whole-abdomen coverage using HP ¹³C MRI is challenging for the following reasons. First, the large field of view requires adequate transmitter and receiver coil coverage. Second, physiologic motion such as respiration, cardiac activity, and bowel peristalsis requires a fast, motion-insensitive imaging sequence. Finally, the presence of air-filled structures such as the lungs and the bowel can cause non-uniformities in the magnetic field (B_0) that could confound metabolite-specific imaging methods.

The first aim of this study was to develop a specialized approach combining several important imaging tools to overcome these limitations for performing HP ¹³C MRI throughout the whole abdomen in healthy volunteers. The second aim of this study was to obtain preliminary estimates of normal HP [1-¹³C]pyruvate metabolism and its variation in solid abdominal organs of healthy volunteers.

6.3 Methods

This study was approved by the local Institutional Review Board (IRB), with written informed consent under a protocol approved by the US Food and Drug Administration Investigational New Drug (FDA IND) application.

6.3.1 Radiofrequency Coil Array

HP ^{13}C data were acquired using a volumetric transmitter and an 8-channel flexible receiver array (QTAR, Clinical MR Solutions, Brookfield, WI) that covered the abdomen. Figure 6.1A and 6.1B show the internal coil arrays of the transmitter and receiver components, respectively. The transmitter coil was 33.0×22.9 cm and each receiver coil was 21.5×15.0 cm.

6.3.2 B_1^+ Mapping

In order to characterize the spatial uniformity of the transmitter coil, transmit field (B_1^+) mapping was performed on a 27.8 cm-diameter spherical dimethyl silicon phantom using a Bloch-Siegert acquisition scheme on a clinical 3 T scanner (MR750, GE Healthcare, Milwaukee, WI) with commercial software (RTHawk, HeartVista, Inc., Los Altos, CA) (Figure 6.1C) ³¹. The imaging sequence followed previously published methods beginning with a single-band spectral-spatial radiofrequency (RF) pulse with a 130 Hz full width at half maximum (FWHM) passband and an 868 Hz stopband (all subsequently stated frequencies in text and in figures have been scaled to reflect ^{13}C imaging) ^{31,32}. The excitation pulse was followed by an off-resonance Fermi pulse (duration = 12 ms, frequency offset = ± 4.5 kHz, and phase shift constant, K_{BS} , of 6.76 rad/G^2) and a single-shot spiral readout ^{31,33}. Other scan parameters were: repetition time (TR) = 300 ms, echo time (TE) = 21 ms, acquisition matrix =

30×30 voxels, in-plane spatial resolution = 30×30 mm, flip angle = 75° , acquisition bandwidth = 250 kHz, and signal averages = 200.

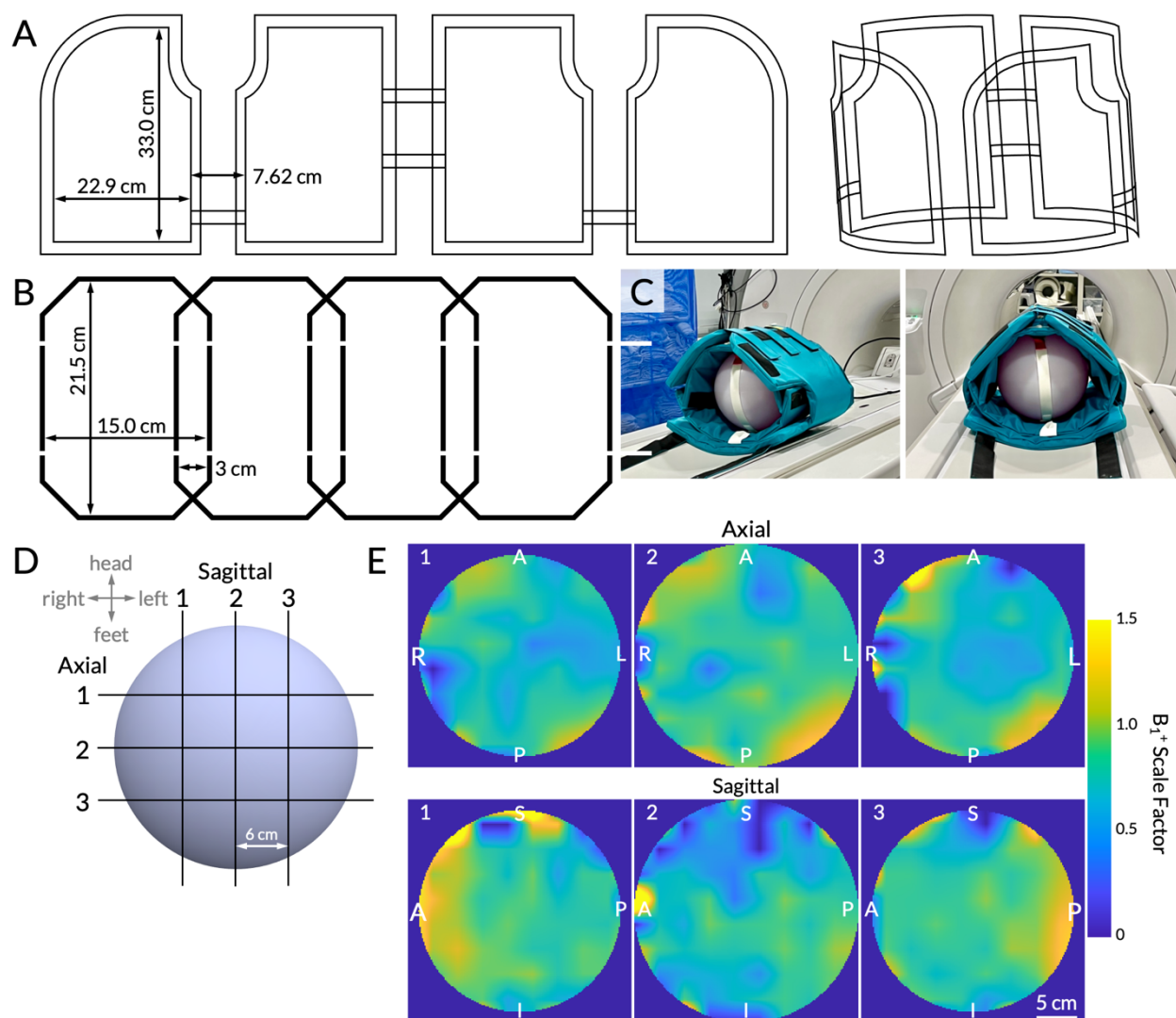


Figure 6.1. (A) Schematic conductor paths of the ^{13}C volumetric transmitter, shown flat and in 3D. (B) Schematic conductor paths of the ^{13}C receiver array. One of two identical 4-channel arrays is shown. (C) The coil setup using a 27.8 cm wide spherical dimethyl silicon phantom for Bloch-Siegert B_1^+ mapping. The inner vest is the 8-channel receiver array and the outer vest is the transmitter. (D) A schematic of the multi-slice B_1^+ maps. Three slices were acquired in the sagittal and axial planes with a 6 cm center-to-center separation. The slice numbers correspond to the B_1^+ maps (interpolated for display) shown in (E). Right/Left, Anterior/Posterior, and Superior/Inferior labels are displayed on the edges. The adjacent color bar shows the B_1^+ scale factor ranging from 0 to 1.5, with 1.0 indicating transmit power that matches the prescribed value.

Three 3.0 cm-thick slices were acquired in sagittal and axial planes, each separated by 6.0 cm (Figure 6.1D shows a schematic of these slices). Data were reconstructed using MATLAB 2021a (The

MathWorks, Inc., Natick, MA) following previously published methods³¹. The complex conjugate of the positive phase map was multiplied with the negative phase map. After taking the sum in the coil dimension, the phase, ϕ_{BS} , of the resulting matrix was obtained. The B_1^+ map was calculated using Equation 6.1:

$$B_1^+ = \frac{\sqrt{\frac{\phi_{BS}}{2K_{BS}}}}{B_{1,ref}} \quad (6.1)$$

where $B_{1,ref}$ is a reference maximum power of the Fermi pulse (0.3 G)^{31,33–35}. The resulting B_1^+ values were normalized such that a value of 1.0 indicated delivery of the prescribed flip angle. Images were interpolated to match the resolution of proton (^1H) images with a final matrix size of 576×576 . Regions outside the phantom were masked as determined by the phantom's size and the image voxel size. The mean and standard deviation of the B_1^+ scale factors were calculated over a circular 10 cm region of interest (ROI) placed in the center of the middle slice and the four quadrants.

6.3.3 Study Eligibility

Inclusion criteria for this pilot study were age ≥ 18 years at the time of study. Subjects were excluded if they had 1) poorly controlled hypertension (systolic blood pressure >160 mmHg or diastolic blood pressure >100 mmHg); 2) congestive heart failure (New York Heart Association status ≥ 2); 3) pregnant or nursing; or 4) any contraindications to MRI.

6.3.4 ^1H MRI Scans

Proton imaging was performed with standard clinical imaging sequences and the full-volume body coil for both transmit and receive (Table 6.1). T_1 -weighted spoiled gradient echo and T_2 -weighted single-shot fast spin echo images were obtained for scan planning and anatomic registration of ^{13}C

data. In addition, multi-echo gradient echo acquisition (Iterative Decomposition of water and fat with Echo Asymmetry and Least square estimation (IDEAL IQ), GE Healthcare) was used to generate fat fraction, T_2^* , and ΔB_0 maps. All images were acquired at end-inspiration to match the positioning of the ^{13}C images.

Table 6.1. Scan parameters for all proton (^1H) and carbon-13 (^{13}C) human scans.

Sequence	Repetition time (TR); echo time (TE)	In-plane spatial resolution	Matrix size; FOV	# Slices; slice thickness; slice gap	Flip angle	Pixel Bandwidth	Acquisition time; temporal resolution
T_1 -weighted spoiled gradient echo (^1H anatomical images)	3.73-4.12 ms; 1.67-1.88 ms	0.352×0.352 to 0.938×0.938 mm	512×512 to 1024×1024 ; 36×36 to 48×48 cm	44-152; 4.4-10 mm; 0 mm	8°	391-558 Hz	< 30 s; N/A
T_2 -weighted single-shot fast spin echo (axial ^1H anatomical images)	545-2200 ms; 48.6-83.8 ms	0.703×0.703 to 1.563×1.563 mm	256×256 to 512×512 ; 30×30 to 40×40 cm	40-92; 5-6 mm; 0 mm	90°	195-326 Hz	< 60 s total scan time divided into ≥ 4 acquisitions; N/A
T_2 -weighted single-shot fast spin echo (coronal ^1H anatomical images)	1690-4400 ms; 9.70-86.4 ms	0.664×0.664 to 0.781×0.781 mm	512×512 ; 340×340 to 400×400 cm	10-36; 5-14 mm; 0-1 mm	90°	195-244 Hz	< 60 s total scan time divided into ≥ 4 acquisitions; N/A
Multi-echo gradient echo (ΔB_0 maps)	6.73-7.70 ms; 3.11-3.592 ms; 7 echoes; 0.86 ms echo spacing	1.406×1.406 to 1.875×1.875 mm	256×256 ; 36×36 to 48×48 cm	16-46; 7-10 mm; 0 mm	$3-4^\circ$	710 Hz	< 35 s; N/A
Echo-planar spectroscopic imaging (EPSI) (^{13}C spectroscopic images)	130 ms; 3.5-5.2 ms; 53 echoes; 1.83 ms echo spacing (545 Hz spectral bandwidth)	20×20 to 22×22 mm	16×18 ; 32×36 cm to 35.2×39.6 cm	1; 20-30 mm; N/A	pyruvate: 10° ; lactate: 20° ; alanine: 15° (constant flip angles)	Slice-selective multiband spectral-spatial;	60 s; 3 s
Echo-planar imaging (EPI) (^{13}C metabolite images)	64-72 ms; 22 ms	20×20 mm	16×16 ; 32×32 cm	7-14; 20 mm; 20 mm	pyruvate: 30° ; lactate: 60° ; alanine: 60° (constant flip angles)	Slice-selective single-band spectral-spatial	60 s; 3 s

6.3.5 Hyperpolarized ^{13}C MRI Scans

Hyperpolarization of $[1-^{13}\text{C}]$ pyruvate

A mixture of 1.46 g Good Manufacturing Practice grade $[1-^{13}\text{C}]$ pyruvic acid (ISOTECH Stable Isotope Division, MilliporeSigma, Miamisburg, OH) and 15 mM trityl radical (GE Healthcare, Milwaukee, WI) was prepared and loaded in pharmacy kits (GE Healthcare, Milwaukee, WI) according to the IRB- and FDA IND-approved manufacturing processes. Following polarization for at least two hours in a 5 T SPINlab clinical-research polarizer (GE Healthcare, Milwaukee, WI), the sample was rapidly warmed, dissolved, and neutralized in 18.25 g of buffer composed of 333 mM Tris, 600 mM sodium hydroxide, and 333 mg/L disodium EDTA. Injection was performed following approval of a staff clinical pharmacist. The injection rate was 5 mL/s followed by a 20 mL saline flush. The injection volume was determined using the weight-based dose of 0.43 mL/kg (total body weight) with a maximum of 40 mL.

Radiofrequency Power Calibration

The RF pulse was calibrated using a spherical dimethyl silicon phantom and a 2 ms hard pulse. The transmit gain for a 90° flip was recorded and confirmed using a 30° flip which resulted in a signal with half the maximum amplitude.

Subject and Coil Positioning

After calibration, the subject was placed on the scanner bed and the QTAR receiver array was first fitted around the abdomen followed by the transmitter. The positioning of the coil was iteratively adjusted using embedded fiducial markers and ^1H anatomical scans to ensure coil coverage from the top of the liver to the bottom of the kidneys.

¹³C Center Frequency Determination

An initial estimate of the center frequency for the HP [1-¹³C]pyruvate acquisition was determined using the center frequency of the ¹H scans and a conversion factor empirically derived from prior acquisitions³⁶. For a subset of the subjects receiving two HP ¹³C scans, further adjustments were made according to the procedure described below.

Shimming

For all subjects, shimming was initially determined based on the scanner's built-in auto-shimming algorithm that was performed at the time of the IDEAL IQ acquisition. For a subset of scans, additional shimming was performed using a localized shim box to reduce B₀ inhomogeneities within the target volume. The targeted shim region was centered on the right hepatic lobe and kept below the diaphragm to avoid air-tissue interfaces. The size of the local shim box varied depending on the size of the liver and measured 10 cm Left/Right, 8-12 cm Anterior/Posterior, and 11-15 cm Superior/Inferior. The z-shim was further adjusted manually to reduce residual B₀ inhomogeneities in the through-plane direction.

Quantification of the final state of B₀ homogeneity within each organ was performed post-injection using whole organ 3D ROIs drawn in MATLAB by an investigator (PML, 4 years). Frequency variations without and with local shimming were visualized with box plots. Outliers were defined as values more than 1.5 times the interquartile range from the top or bottom of the box. Upper and lower quartile bounds were used to compare not only frequency variance but also to evaluate whether the majority of the voxels in each organ were within the FWHM, or 50% excitation, of the excitation pulse's passband.

Hyperpolarized ^{13}C Acquisition Timing

The serial dynamic HP ^{13}C MRI acquisition was started 5 s after the saline injection completed. Each subject was asked to hold their breath as long as easily tolerated, followed by free breathing for the rest of the 60 s acquisition.

Echo-planar Spectroscopic Imaging

The 2D dynamic echo-planar spectroscopic imaging (EPSI) pulse sequence consisted of a slice-selective multiband spectral-spatial pulse followed by an EPSI readout similar to prior prostate cancer studies^{4,37,38}. The scan parameters were (Table 6.1): TR = 130 ms, TE = 3.5-5.2 ms, number of echoes = 53, echo spacing = 1.83 ms, spectral bandwidth = 545 Hz, in-plane spatial resolution = 20×20 to 22×22 mm, matrix size = 16 phase encode \times 18 readout voxels, slice thickness = 20-30 mm, constant flip angles = 10° for pyruvate, 20° for lactate, and 15° for alanine, acquisition time = 60 s, and temporal resolution = 3 s.

EPSI-derived ΔB_0 Maps

EPSI data were processed according to previously published methods, including tensor rank truncation, phase corrections, and baseline correction, but not B_0 (this would nullify the desired ΔB_0 maps) or B_1^+ corrections³⁹. For each voxel, spectra were summed through time and the highest value within the chemical shift range of 171.13 to 174.10 ppm was taken to be the pyruvate peak. An empirical pyruvate peak reference value of 172.58 ppm was used to compute the ΔB_0 for each voxel, resulting in EPSI-derived ΔB_0 maps (subsequently referred to as ^{13}C ΔB_0 maps).

These ^{13}C ΔB_0 maps were compared against those acquired using the ^1H multi-echo gradient echo acquisitions (subsequently referred to as ^1H ΔB_0 maps). First, the ^1H ΔB_0 maps were scaled to

account for the different gyromagnetic ratio of ^{13}C and then an ROI was drawn around the abdomen by an investigator (PML, 4 years). The ^1H ΔB_0 maps were then down-sampled to match the spatial resolution of the ^{13}C ΔB_0 maps (Figure 6.2A). An empirical signal-to-noise ratio (SNR) threshold of 40.0 for pyruvate was used to filter out voxels in both ΔB_0 maps. In addition to taking their difference, the two ΔB_0 maps were plotted against each other and linear regressions were computed to quantify correlations. To investigate biases, the differences in frequencies between the two ΔB_0 maps were plotted against the ^1H ΔB_0 map.

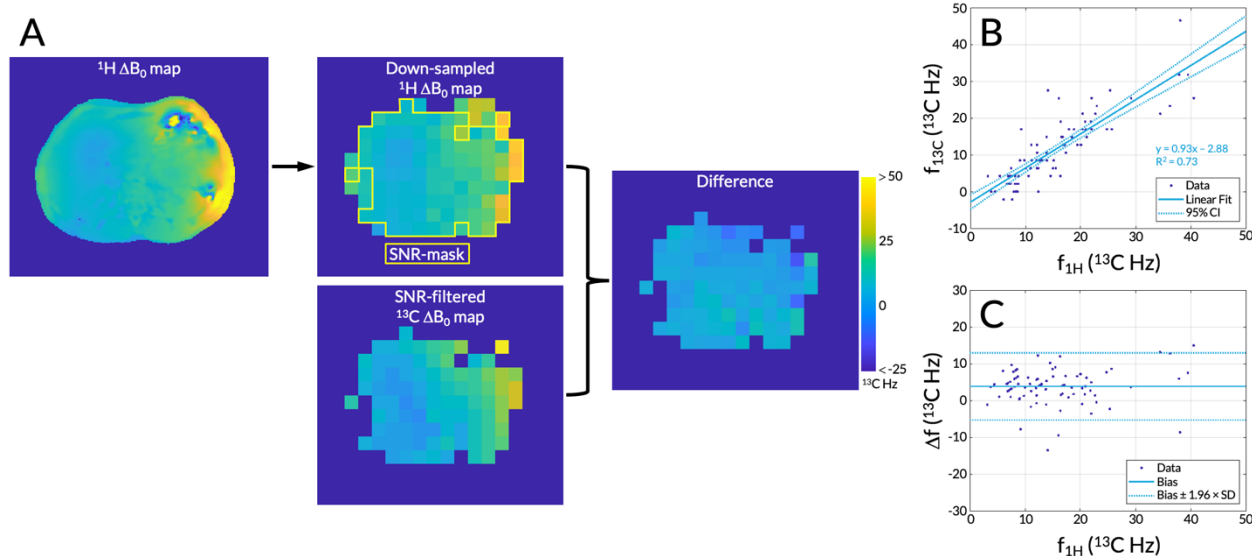


Figure 6.2. (A) A representative ^1H ΔB_0 map, which was down-sampled to match the spatial resolution of the ^{13}C ΔB_0 map. A signal-to-noise ratio (SNR) filter using empirical thresholds based on the echo-planar spectroscopic imaging (EPSI) data was applied to both ΔB_0 maps. Voxels in the ^1H ΔB_0 map that passed this SNR filter are highlighted with a yellow outline. Both ΔB_0 maps were scaled using the ^{13}C gyromagnetic ratio and the difference between the two maps was taken. The same color bar is applicable to all images. (B) A correlation plot of the frequencies from each separate ΔB_0 map plotted against each other with 95% confidence interval (CI) shown. (C) A Bland-Altman plot showing the bias between the two ΔB_0 maps with dotted lines indicating $\pm 1.96 \times$ the standard deviation, or 95% of the differences having tested for normality.

Metabolite-specific Echo-planar Imaging

$[1-^{13}\text{C}]$ pyruvate, $[1-^{13}\text{C}]$ lactate and $[1-^{13}\text{C}]$ alanine signals were acquired using a multi-slice metabolite-specific echo-planar imaging (EPI) acquisition⁴⁰. The scan parameters were (Table 6.1): TR (time per

metabolite per slice) = 64-72 ms, TE = 22 ms, in-plane spatial resolution = 20×20 mm, matrix size = 16×16 voxels, number of slices = 7-14, slice thickness = 20 mm, constant flip angles = 30° for pyruvate and 60° for lactate and alanine, acquisition time = 60 s, and temporal resolution = 3 s. A variable number of slices was used in order to cover the top of the liver to the bottom of the kidneys.

When the EPI scan was the sole ^{13}C acquisition, the center frequency was determined using the center frequency of the ^1H scans and the empirical conversion factor discussed earlier. When the EPI scan was preceded by an EPSI scan, the initial estimate of the center frequency was adjusted based on the acquired spectra.

6.3.6 Data Processing & Kinetic Modeling

Kinetic modeling was performed based on data from metabolite-specific EPI acquisitions. Data were phase corrected, Fourier transformed, pre-whitened, and coil-combined using the pyruvate signals to estimate the coil weights in MATLAB, as previously described ⁴¹. Data were denoised using a patch-based higher-order singular value decomposition (HOSVD) with the following previously-published parameters: patch size = 5×5 , search window size = 11, step length = 2, $k_{\text{global}} = 0.4$ and $k_{\text{local}} = 0.8$ ⁴².

Data were linearly interpolated in the slice dimension by a factor of 4 and then interpolated in the x and y dimensions by zero-padding k -space also by a factor of 4. A 2D radially symmetric Fermi filter was computed using the following Fermi-Dirac distribution (Equation 6.2):

$$f = \frac{1}{1 + e^{\frac{(x^2+y^2)-\alpha}{\beta}}} \quad (6.2)$$

where x and y are the number of voxels in the image's two dimensions, $\alpha = 0.5 \times \frac{N-1}{2}$, and $\beta = 0.07813 \times \frac{N-1}{2}$, with N being the number of voxels in the image's longest dimension. The zero-

padded k -space data were multiplied by the Fermi filter and subsequently 2D inverse Fourier transformed.

An ROI was drawn around the entire abdomen by an investigator (PML, 4 years) to generate a mask to remove voxels outside of the abdomen. The SNR of each voxel was computed as the AUC ^{13}C signal divided by the standard deviation of background noise (calculated using test scans acquired prior to injection). Empirical SNR thresholds (pyruvate = 50.0, lactate = 20.0, and alanine = 10.0) were then used to create SNR masks to filter out noise voxels. Quantification of SNR improvement was measured by the percent of voxels within the abdominal ROI that passed these metabolite SNR thresholds before and after denoising. Additionally, the mean SNR of the voxels within the abdominal ROI was computed for each metabolite over the 20 timepoints and compared against the SNR thresholds (divided by time due to data being dynamic) to evaluate improvements in SNR after denoising.

For each subject with an EPI scan, the pyruvate dynamic curves of every voxel in five organs of interest (the liver, right and left kidneys, pancreas, and spleen) were characterized by the metrics time-to-peak and decay time. Time-to-peak was defined as the timepoint when the pyruvate signal reached its highest value after the start of acquisition. Timepoints greater than 50 s were rejected. Decay time was defined as the interval between the peak timepoint and the following half-maximum timepoint. To calculate the decay time, the two timepoints before and after the signal crossed the half-maximum value were obtained. If neither of the two timepoints were greater than 50 s, the signal was linearly interpolated to estimate the half-maximum timepoint. The half-maximum timepoint was subtracted by the time-to-peak to give the decay time. Finally, both metrics in all organs were normalized by the mean values of the right and left kidneys.

Metabolite signals were summed over the entire time course to produce metabolite area under the curve (AUC) maps. First-order conversion rates of pyruvate to lactate (k_{PL}) and of pyruvate to

alanine (k_{PA}) were computed using an inputless two-site exchange model¹⁷. Fitting was performed across a range of flip angles centered around the nominal values and the flip angles that resulted in the lowest lactate and alanine root-mean-square error were chosen. In addition to the flip angles, other parameters given to the model were: number of phase encodes per timepoint = 1, number of timepoints = 20, TR = 3, T_1 of pyruvate = 30 s, T_1 of lactate = 25 s, and T_1 of alanine = 25 s. Initial estimates of k_{PL} and k_{PA} of 0.02 s^{-1} and 0.01 s^{-1} , respectively, were used as starting conditions for the fits.

Both ^1H and ^{13}C MR images were imported into ITK-SNAP⁴³. Five 3D ROIs were drawn on the ^1H images for the liver, right and left kidneys, pancreas, and spleen by an investigator (PML, 4 years). From these 3D ROIs, mean and standard deviation values of pyruvate time-to-peak and decay time, pyruvate, lactate, and alanine AUC signals, and k_{PL} and k_{PA} values were computed for each organ. Pyruvate time-to-peak, decay time, k_{PL} , and k_{PA} values for each organ were also averaged across EPI scans.

6.3.7 Statistical Analysis

Statistical analysis was conducted in GraphPad Prism 9 (GraphPad Software, San Diego, CA) and MATLAB. Linear regression and Bland-Altman analysis were conducted to investigate correlations between the ^1H and ^{13}C ΔB_0 maps. One-sample Kolmogorov-Smirnov tests were used to test for normality ($P \geq 0.05$ to accept the null hypothesis that data come from a normal distribution). Upon confirming normality, paired t -tests were used to evaluate effects of denoising and an ordinary one-way ANOVA was conducted on the averaged k_{PL} and k_{PA} values. Tukey's multiple comparisons tests were also used to investigate differences in k_{PL} and k_{PA} between organs. $P \leq 0.05$ was considered to be statistically significant.

6.4 Results

6.4.1 B_1^+ Characterization of QTAR

Multi-slice B_1^+ maps of the QTAR coil were acquired with a center-to-center separation of 60 mm (Figure 6.1D). B_1^+ maps acquired using a Bloch-Siegert acquisition revealed higher-than-nominal transmit power in the right-anterior regions (Figure 6.1E, axial images #1-3 and sagittal image #1). Higher transmit power was also observed in the left-posterior regions, similarly reflected in the corresponding sagittal image (Figure 6.1E, axial images #1-3 and sagittal image #3).

The mean B_1^+ scale factor in a central, circular 10 cm region was 0.80 ± 0.10 (Figure 6.1E, axial image #2). The maximum value was 1.03 and the minimum was 0.36. In the right-anterior region of the central axial slice (where the liver would be), the mean B_1^+ scale factor was 0.90 ± 0.16 . The left-posterior region had a mean B_1^+ scale factor of 0.95 ± 0.13 . Lower mean B_1^+ scale factors were observed in the right-posterior and the left-anterior regions, which had mean B_1^+ scale factors of 0.80 ± 0.16 and 0.75 ± 0.13 , respectively.

6.4.2 Healthy Volunteer Scans

A total of thirteen healthy volunteers were prospectively recruited for this study. A summary of all HP ^{13}C acquisitions is shown in Table S6.1. Eight subjects were male and five were female. Subjects were between 21 and 64 years old with a median age of 36 years. Of the thirteen subjects, subject #6 was unable to be imaged due to hardware failure. Due to the iterative nature of this pilot study, two subjects were scanned exclusively with a different pulse sequence or with a different coil than the other subjects. Therefore, data from these subjects were not considered in the final analysis. Of the remaining ten subjects, three had an EPSI acquisition alone, five had an EPI acquisition alone, and two had both.

Pre-injection quality control results were as follows: sterile pyruvate concentration of 245 ± 13 mM, pH of 7.6 ± 0.3 , temperature of 32.4 ± 1.1 °C, and a polarization of $32.7 \pm 8.5\%$. Time from dissolution to injection was 51.2 ± 3.3 s.

6.4.3 ^1H vs. ^{13}C ΔB_0 Maps using Pyruvate's Frequency Offsets

In one representative case comparing the ^1H and ^{13}C ΔB_0 maps, a linear regression had a slope of 0.93 ± 0.12 (95% confidence interval) and a y-intercept of -2.88 ± 1.99 with an R^2 of 0.74 and a $P < 0.0001$ (Figure 6.2B). The bias between the ^1H and ^{13}C ΔB_0 maps was 3.90 ± 9.18 Hz and differences ranged from -13.51 to 15.07 Hz (Figure 6.2C). A one-sample Kolmogorov-Smirnov test accepted the null hypothesis that the differences between the two maps came from a normal distribution ($P = 0.34$). Hence, 95% of the differences fall between $\pm 1.96 \times$ the standard deviation, that is, -5.27 and 13.08 Hz (Figure 6.2C).

6.4.4 B_0 Inhomogeneity Corrections

Representative axial ^1H ΔB_0 maps without and with local shimming are shown in Figure 6.3A. The frequency offsets of various regions of interest in the liver and kidneys are highlighted. The location of the shim box is shown overlaid on the top of T_2 -weighted anatomical references. Box plots of the frequency variation within each organ of interest are shown in Figure 6.3B, both without and with local shimming. Outliers are indicated with X's. The dashed lines at ± 50 Hz correspond to the FWHM, or 50% excitation, of the single-band spectral-spatial pulse's passband used in the metabolite-specific EPI sequence ⁴⁴.

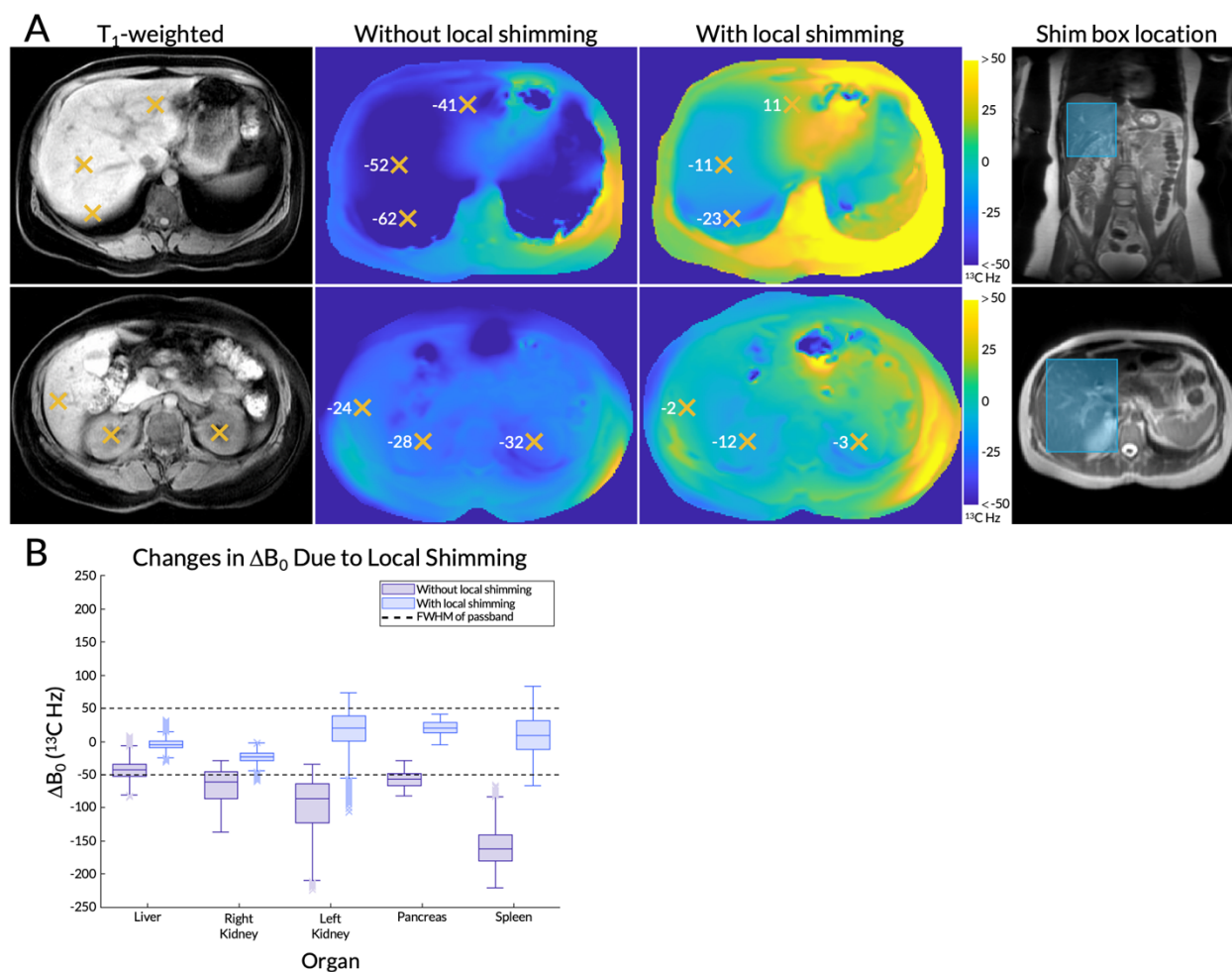


Figure 6.3. (A) Axial ^1H ΔB_0 maps from a representative subject for two slices of interest (T_1 -weighted anatomical images on the left) without and with local shimming. The frequency offsets (scaled to ^{13}C Hz) of various regions of interest in the liver and kidneys are highlighted with orange X's. The location of the shim box is shown on top of T_2 -weighted anatomical references. **(B)** A box and whisker plot of the frequency variation within each organ, both with and without local shimming. Outliers are indicated with X's. The dashed lines at ± 50 ^{13}C Hz correspond to the full width at half maximum (FWHM), or 50% excitation, of the single-band spectral-spatial pulse's passband used in the metabolite-specific echo-planar imaging (EPI) sequence.

Without local shimming, frequency variations in the liver ranged from -80.74 to -6.54 Hz (excluding outliers), with a median of -43.26 Hz. The lower quartile was -53.07 Hz, at the edge of the spectral-spatial pulse's passband. The upper quartiles of the frequency variations in the right and left kidneys were -46.03 and -64.14 Hz, respectively. Hence, the majority of their voxels was outside of the 50% excitation passband. The pancreas had an upper quartile of -49.30 Hz and the spleen's upper

whisker reached -83.51 Hz, with its entire interquartile range far beyond the passband. After local shimming in the liver, median frequency offsets and variations in B_0 were both reduced in the liver as expected (median was -5.03 Hz and whiskers ranged from -24.65 to 15.09 Hz), but also in other organs. All organs had a median value between ± 25 Hz and the upper and lower whiskers of the liver, right kidney, and pancreas were also within the passband. The left kidney and spleen (located further from the shim box) contained some voxels with frequencies outside of the passband.

6.4.5 Patch-Based Denoising

In one representative subject, EPI data denoised using HOSVD had reduced background noise across all timepoints (Figure 6.4A). Figure 6.4B shows the fifth timepoint (time = 12 s) of the central ^{13}C slice enlarged, with arrows pointing to the head and tail of the pancreas. Quantification over data from all seven EPI scans showed that before denoising, $27 \pm 13\%$ of all pyruvate voxels in the abdomen passed the SNR threshold of 50.0. This increased to $87 \pm 15\%$ after denoising ($P < 0.0001$) (Figure 6.4C). Similar increases were observed for lactate ($20 \pm 8.0\%$ to $87 \pm 13\%$, $P < 0.0001$) and alanine ($22 \pm 10\%$ to $91 \pm 12\%$, $P < 0.0001$). The large variance observed after denoising is attributable principally to data from one subject (subject #9, Figure S4.1). Despite this outlier, tests for normality using data from all seven subjects passed with $P \geq 0.19$ in accepting the null hypothesis. For the same slice highlighted in Figure 6.4B, the mean SNR within the abdomen was also elevated throughout the entire time course after denoising (Figure 6.4D). Before denoising, the mean SNR dropped below the empirical SNR thresholds (scaled for dynamic data) at time = 30 s for pyruvate, time = 36 s for lactate, and time = 51 s for alanine. After denoising, the SNR did not drop below the thresholds over the 60 second time course.

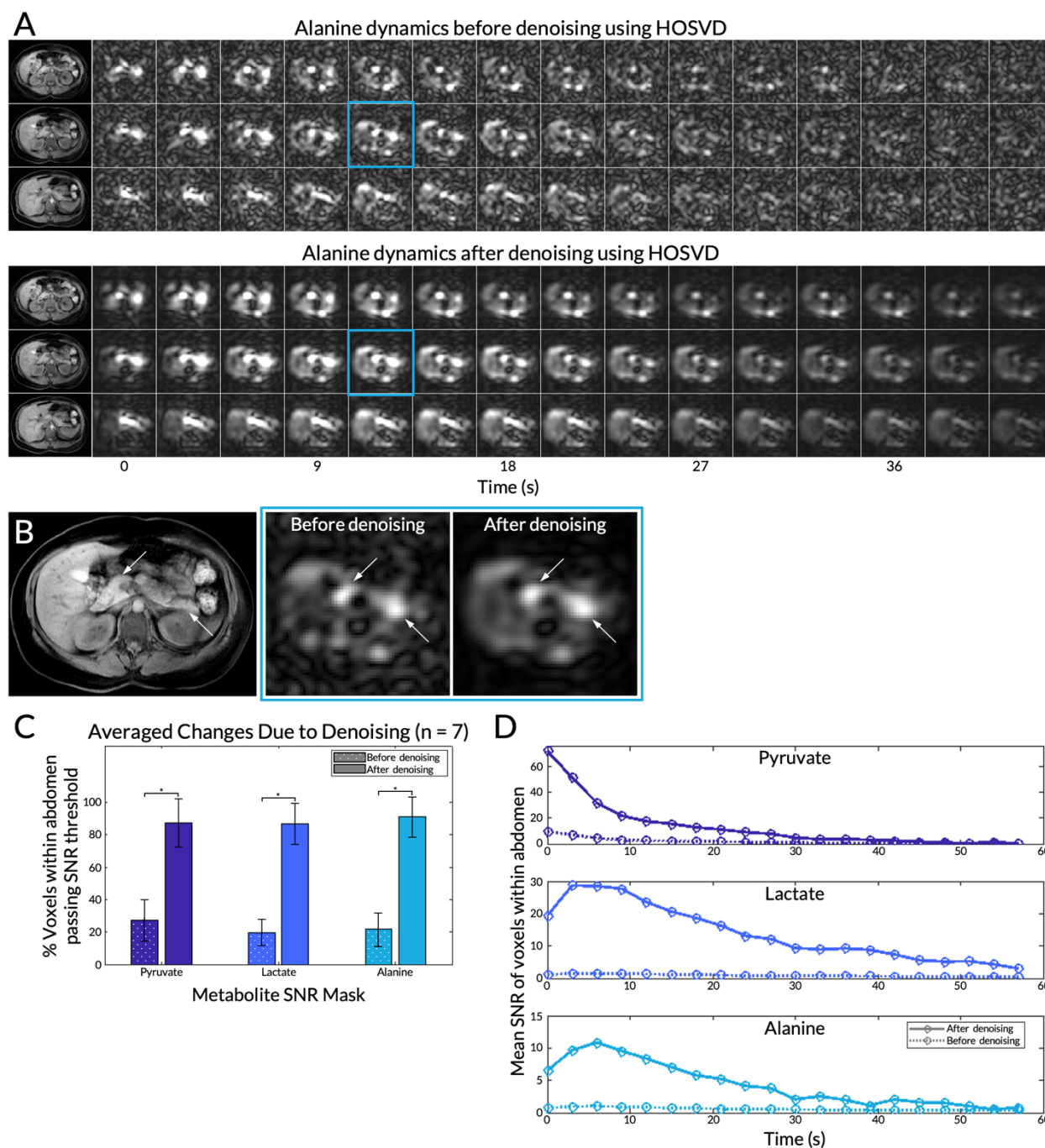


Figure 6.4. (A) The first 42 seconds of the alanine dynamics before and after patch-based higher-order singular value decomposition (HOSVD) denoising for three slices from a representative subject. Corresponding T_1 -weighted anatomical references are on the left. (B) Detailed view of the fifth timepoint images (time = 12 s) of the central ^{13}C slice before and after denoising enlarged. Left and right arrows point to the head and tail of the pancreas, respectively. (C) Percent of voxels passing the SNR thresholds for each metabolite before and after denoising. Error bars indicate standard deviations. Significance levels are indicated by asterisks, with *** meaning $P \leq 0.0001$. (D) For the same slice highlighted in (B), the mean SNR of voxels within the whole abdomen before and after denoising over the course of the 20 timepoints.

6.4.6 Metabolite Dynamics in Each Organ

Plots of the dynamic curves for each metabolite in the right kidney, liver, spleen, and pancreas from a representative EPI scan are shown in Figure 6.5A. The raw signals are plotted with circles and dashed line while the fitted curves, computed by the inputless two-site exchange model, are shown in solid lines. Of the seven subjects with EPI scans, data from subject #13 was not considered because acquisition began after the peak pyruvate signal in the kidneys had occurred. From the remaining six scans, the mean normalized pyruvate peak time in the liver was 2.9 ± 2.4 s (Figure 6.5B). Those of the kidneys were 0 s due to normalization. The time-to-peak in the pancreas and spleen were -0.7 ± 0.7 s and 1.1 ± 1.2 s, respectively. Decay time was highest in the liver and the spleen ($P \leq 0.052$) at 4.6 ± 1.8 s and 4.9 ± 2.3 s, respectively. Tests for normality passed for both metrics in all organs ($P \geq 0.52$). One-way ANOVA tests for both metrics across organs gave $P < 0.0001$. However, comparisons of time-to-peak between organs were not statistically significant ($P \geq 0.069$). While comparisons of decay time in the liver and the spleen were not significantly different, comparisons between the liver and the other organs were ($P < 0.05$).

6.4.7 Summed Metabolite Signals & Metabolite Kinetics in Each Organ

From a representative subject, the metabolite maps summed through time are displayed in Figure 6.6A, overlaid on top of a T_1 -weighted anatomical reference. The mean pyruvate, lactate, and alanine signals within each organ for this subject are shown in Figure 6.6B. In this subject, mean pyruvate signals were highest in the spleen (1.8 ± 0.69 AU) and the kidneys (right: 1.2 ± 0.29 AU, left: 1.4 ± 0.32 AU) (Figure 6.6B). The same organs also exhibited the highest lactate signals (spleen: 0.28 ± 0.083 AU, right kidney: 0.18 ± 0.043 AU, and left kidney: 0.23 ± 0.050 AU). The liver had the lowest overall pyruvate and lactate signals and it also had the lowest standard deviation for the two metabolites

(pyruvate = 0.13 AU, lactate = 0.028 AU) compared to the other organs. The highest alanine signal was observed in the pancreas (0.14 ± 0.031 AU) while the lowest were in the liver (0.045 ± 0.019 AU) and spleen (0.039 ± 0.021 AU). Though not measured using an ROI, elevated alanine signals were observed in the paraspinal muscles compared to the background (Figure 6.6A). Although the right kidney is not shown in the anatomical reference, pyruvate signal from that kidney is present in this axial slice due to partial volume effects and the 20 mm slice thickness.

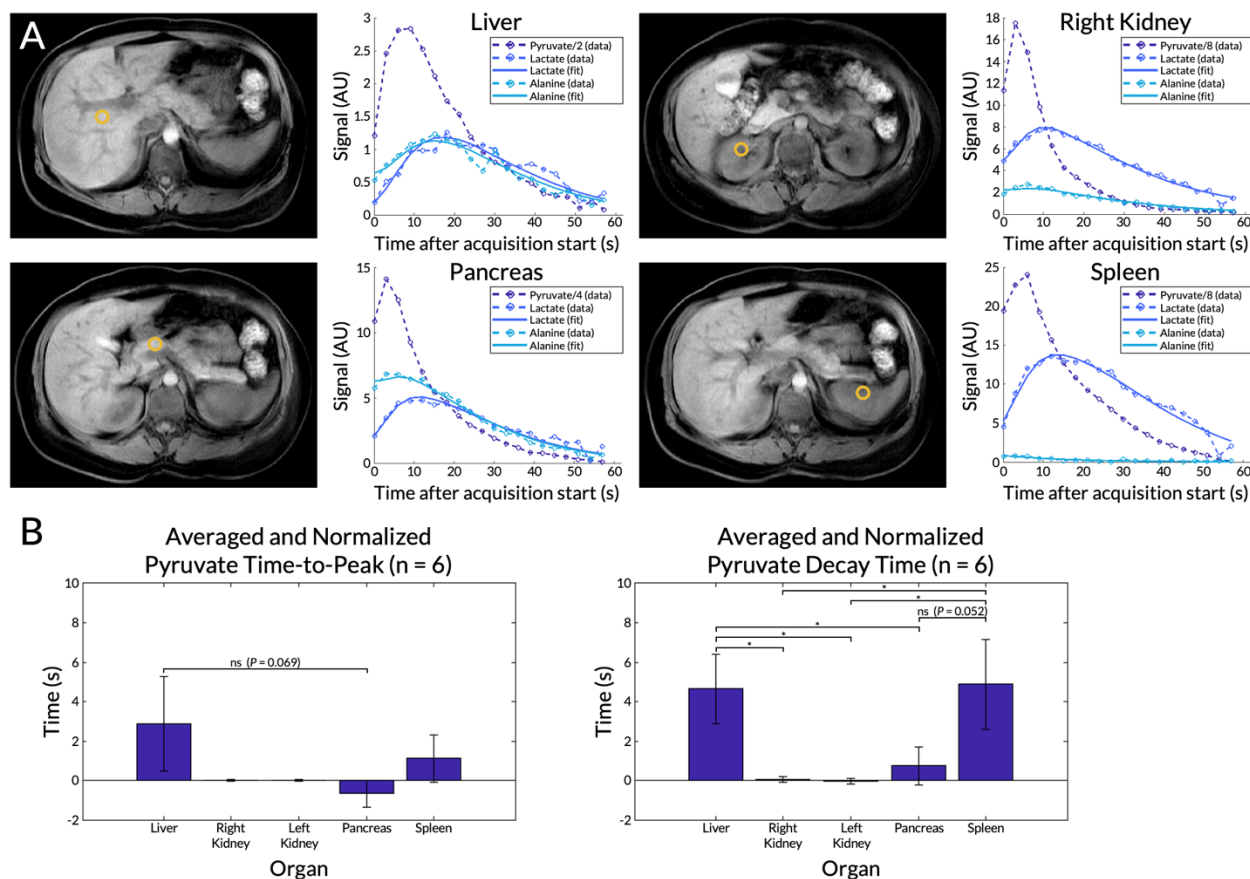


Figure 6.5. (A) Dynamic curves for each metabolite from a selected voxel in the liver, right kidney, pancreas, and spleen from a representative EPI scan. Locations of the voxels are shown in the corresponding T_1 -weighted anatomical images. Measured signals (circles and dashed lines) are shown together with curve fits computed using an inputless two-site exchange model (solid lines). The pyruvate signals were scaled for display. **(B)** Mean pyruvate time-to-peak and decay time for each organ averaged across six subjects with EPI scans (subject #9 was excluded). Error bars indicate standard deviations. Significance levels are indicated by asterisks, with * meaning $P \leq 0.05$, ** meaning $P \leq 0.01$, and “ns” meaning $P > 0.05$. Unlabeled comparisons were not statistically significant.

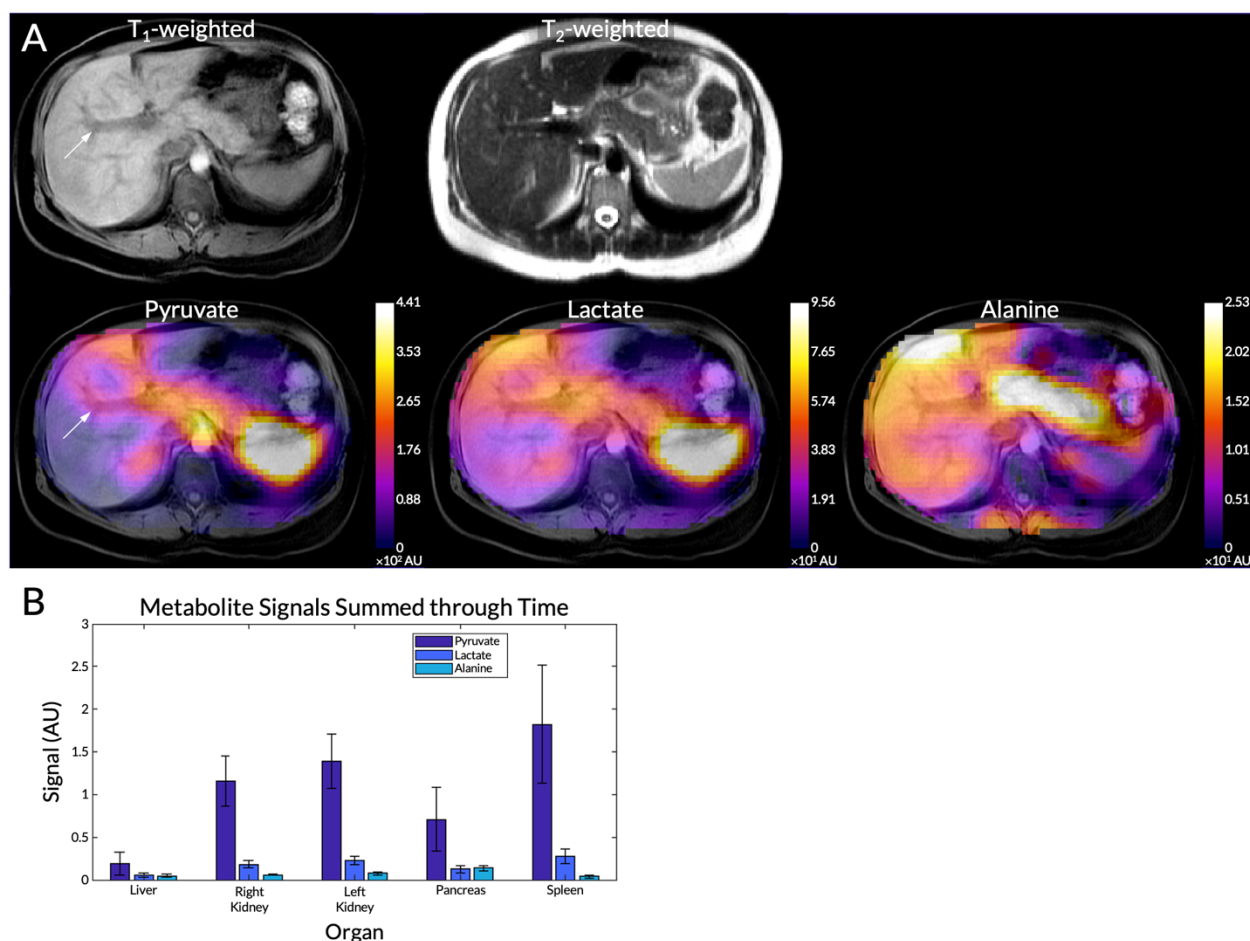


Figure 6.6. (A) Pyruvate, lactate, and alanine maps summed through time from a representative subject overlaid on top of a T_1 -weighted anatomical reference. The T_2 -weighted anatomical reference is also shown in the top row. An arrow highlights the portal vein. (B) Mean pyruvate, lactate, and alanine signals within each organ for this subject. Error bars indicate intra-organ standard deviation.

For the same subject, values of k_{PL} and k_{PA} were greatest in the parenchymal tissue of the liver, with voids around blood vessels as expected (highlighted with arrows in Figure 6.7). Low k_{PA} was observed in the spleen. Mean k_{PL} and k_{PA} values for the seven successful EPI scans are shown in Figure 6.8. Tests for normality passed for both metrics in all organs ($P \geq 0.23$). Mean and standard deviation values and comparisons between organs with statistical significance values are displayed in Table 6.2. One-way ANOVA tests for both k_{PL} and k_{PA} across organs gave $P < 0.0001$. All comparisons of k_{PL} and k_{PA} between the liver and those of other organs were statistically significant, with all having $P < 0.0001$ except for the liver versus the spleen, which had $P < 0.0028$. Hence, although the absolute

lactate and alanine signals were lower in the liver compared to other organs (Figure 6.6B), the liver exhibited the highest rate of conversion from pyruvate to lactate and to alanine ($k_{PL} = 0.019 \pm 0.0076 \text{ s}^{-1}$, $k_{PA} = 0.012 \pm 0.0037 \text{ s}^{-1}$, $P \leq 0.0022$). Although not statistically significant, the pancreas did exhibit a trend of higher alanine production compared to the kidneys (right: $P = 0.12$, left: $P = 0.078$) and the spleen ($P = 0.057$).

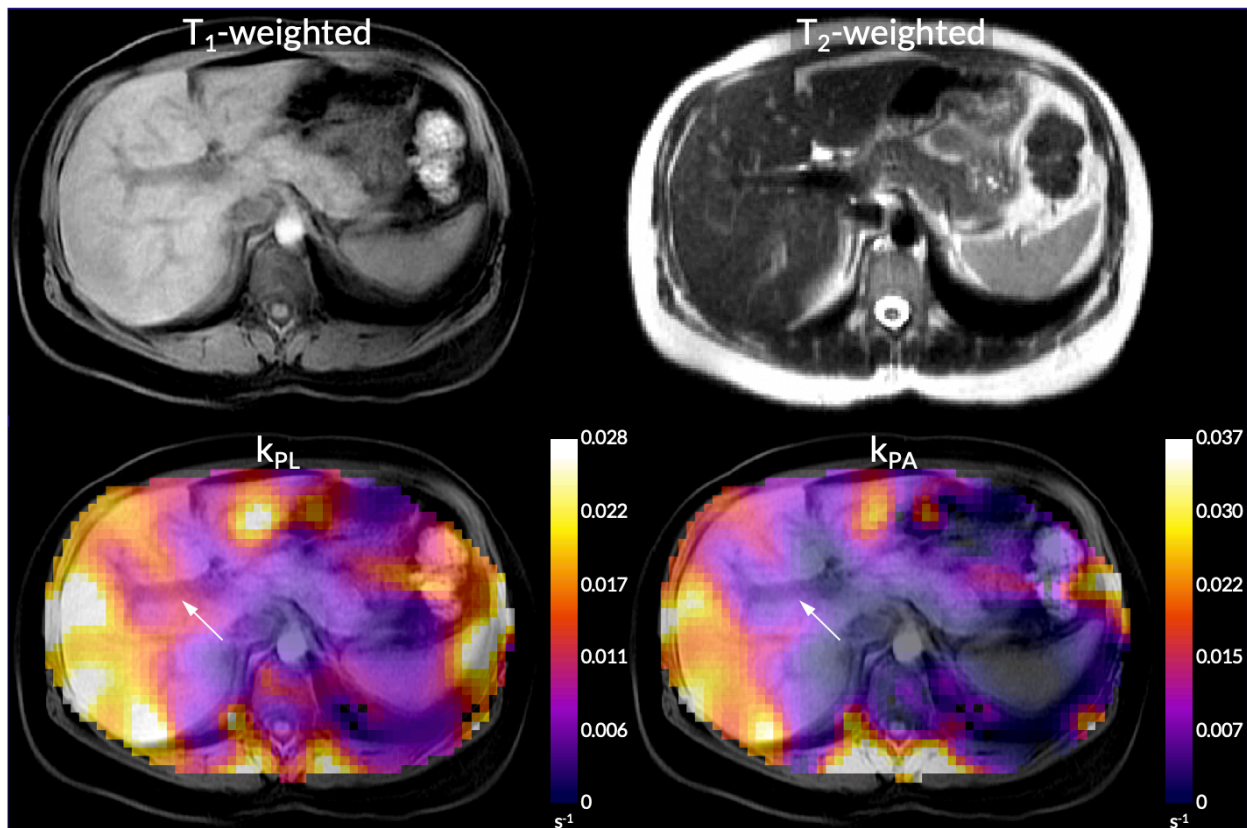


Figure 6.7. k_{PL} and k_{PA} maps overlaid on top of a T_1 -weighted anatomical reference from the same subject shown in **Figure 6.6**. The T_2 -weighted anatomical reference is also shown in the top row. An arrow highlight the portal vein.

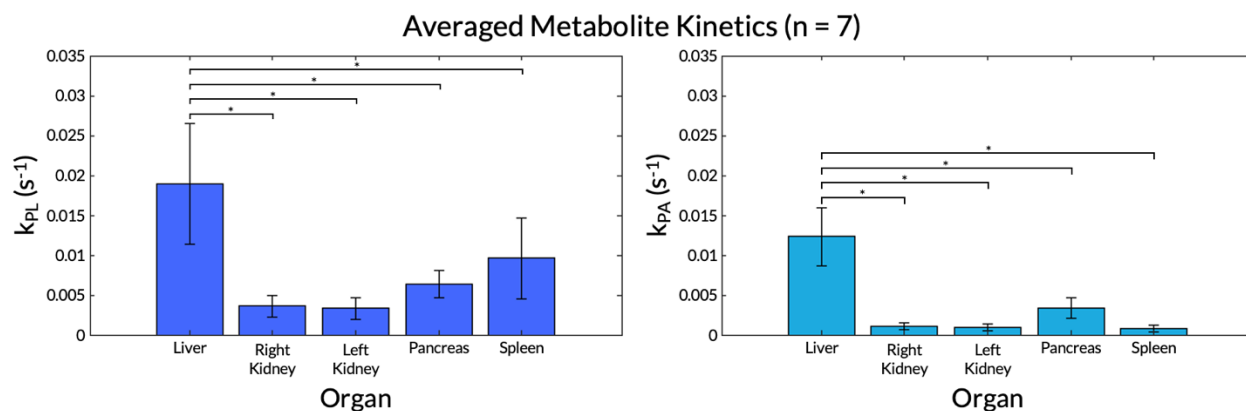


Figure 6.8. k_{PL} and k_{PA} values for each organ averaged across all seven subjects with EPI scans. Error bars indicate standard deviations. Significance levels are indicated by asterisks, with ** meaning $P \leq 0.01$ and **** meaning $P \leq 0.0001$. All other comparisons were not significant ($P > 0.05$). Unlabeled comparisons were not statistically significant.

6.5 Discussion

To effectively translate HP [1-¹³C]pyruvate MRI into the clinic for assessing neoplastic and metabolic disease in the abdomen, a specialized whole-abdomen imaging approach is required. This method must have sufficient coverage, be insensitive to respiratory motion, and address B_0 inhomogeneities present due to air-tissue interfaces. Post-processing of the data must address low SNR through denoising methods, and compute key metabolic metrics, such as k_{PL} and k_{PA} , to metabolically characterize organs of interest. In this study, a whole-abdomen HP [1-¹³C]pyruvate metabolic imaging protocol was developed and used to characterize normal metabolic energetics in the human liver, kidneys, pancreas, and spleen.

This imaging protocol did not seek to address all challenges that can occur when conducting HP ¹³C MRI studies, such as dissolution hardware failures. Additionally, to avoid confounding factors, data from spiral gradient echo acquisition schemes were not used, although data acquisition was itself successful. Only for one scan was there a QTAR coil hardware failure. Therefore, given the scope of this pilot study and its aims, with only one acquisition failing against twelve successful scans, this imaging protocol was considered reliable for future studies.

Table 6.2. Summary of averaged k_{PL} and k_{PA} values across successful echo-planar imaging (EPI) scans, including mean and standard deviation and comparisons between organs with corresponding significance levels.

Kinetic Parameter	Organ	Mean \pm SD (n = 7)	Comparison	P	Significance Level	
k_{PL}	Liver	0.019 \pm 0.0076	Liver vs. right kidney	<0.0001	****	
			Liver vs. left kidney	<0.0001	****	
			Liver vs. pancreas	<0.0001	****	
			Liver vs. spleen	0.0022	**	
	Right kidney	0.0036 \pm 0.0013	Right kidney vs. left kidney	>0.99	ns	
			Right kidney vs. pancreas	0.75	ns	
			Right kidney vs. spleen	0.085	ns	
	Left kidney	0.0033 \pm 0.0014	Left kidney vs. pancreas	0.67	ns	
			Left kidney vs. spleen	0.064	ns	
	Pancreas	0.0063 \pm 0.0017	Pancreas vs. spleen	0.56	ns	
	Spleen	0.0096 \pm 0.0050	Ordinary one-way ANOVA		<0.0001	****
	k_{PA}	Liver	0.012 \pm 0.0037	Liver vs. right kidney	<0.0001	****
				Liver vs. left kidney	<0.0001	****
				Liver vs. pancreas	<0.0001	****
Liver vs. spleen				<0.0001	****	
Right kidney		0.0011 \pm 0.00039	Right kidney vs. left kidney	>0.99	ns	
			Right kidney vs. pancreas	0.12	ns	
			Right kidney vs. spleen	>0.99	ns	
Left kidney		0.00087 \pm 0.00042	Left kidney vs. pancreas	0.078	ns	
			Left kidney vs. spleen	>0.99	ns	
Pancreas		0.0034 \pm 0.0013	Pancreas vs. spleen	0.057	ns	
Spleen		0.00073 \pm 0.00044	Ordinary one-way ANOVA		<0.0001	****

This approach combined several innovations to address the challenges of performing HP ^{13}C MR imaging in the abdomen: 1) a flexible multi-channel coil array and volumetric transmitter to broaden the imaging field of view, 2) a fast, multi-slice metabolite-specific EPI technique to mitigate

the effects of motion, 3) careful shimming and frequency measurement to ensure B_0 field uniformity over the liver, and 4) denoising using patch-based HOSVD to improve the overall apparent SNR.

The flexible large-volume transmit and receive coil used in this study was first characterized. While the homogeneity of the transmitter was sufficient for ^{13}C acquisitions, higher transmit power was observed in the right-anterior and left-posterior regions in a phantom setup. These variations were likely in part due to the flexible transmitter design that resulted in a somewhat irregular transmit coil geometry. The transmitter had cutouts for the coil to fit under the subject's arms at the cost of B_1^+ homogeneity. In addition, as the B_1^+ field is determined by the spatial positioning of the conductors in the transmitter, it was expected that the B_1^+ field of the QTAR coil would vary depending on how it was wrapped around people of different sizes⁴⁵. However, as the standard deviations of B_1^+ scale factors were less than 0.2 (or 20% of 100% transmit power) in each quadrant and in the central, circular 10 cm region of the central axial slice, the B_1^+ variation was acceptable for this pilot study and sufficient signal was still obtained in every organ of interest. Metabolite signals in the right kidney, which were in the region of lower transmit power, had high enough signal for metabolic characterization.

To obtain volumetric and dynamic HP $[1-^{13}\text{C}]$ pyruvate, $[1-^{13}\text{C}]$ lactate, and $[1-^{13}\text{C}]$ alanine signals, a multi-slice metabolite-specific EPI acquisition scheme was used to acquire twenty timepoints over one minute. This approach eliminated motion artifacts due to its short (64-72 ms) acquisition time per slice. One challenge of using metabolite-specific EPI acquisitions was the need to ensure that the relevant metabolites were centered in the 100 Hz passband of the spectral-spatial pulse used in this approach. For several subjects, the ^{13}C frequency range was confirmed using separate HP ^{13}C EPSI acquisitions that included the full chemical shift range for each voxel. As an alternative to these separate HP ^{13}C acquisitions, a simplified ^1H imaging approach with an IDEAL-IQ acquisition was used to measure B_0 frequency shifts. This latter method had the advantage of not requiring a second

injection. As expected, a strong linear correlation between the acquired ^1H ΔB_0 map and the EPSI-derived ^{13}C ΔB_0 map was observed. This allowed forgoing the EPSI acquisition for later subjects with each patient scan, instead using the IDEAL IQ-derived field map to ensure the correct ^{13}C acquisition frequencies.

Measurement of the B_0 field revealed large variations throughout the abdomen, both in-plane and through-plane. These large field variations were a result of the scanner's automatic shimming process and risked placing several regions of the abdomen outside of the 100 Hz FWHM passband employed by the spectral-spatial pulse. After a localized shim volume was placed over the liver, followed by manual adjustments of through-plane frequency variations, frequency variations were greatly reduced throughout the abdomen. Before local shimming, four out of five organs of interest had a median frequency offset outside of the FWHM range of the spectral spatial pulse. After local shimming, all organs had a median frequency offset within the passband; also, the liver, right kidney, and pancreas had minimum and maximum values within the passband. The improvement was more noticeable in the liver and the right kidney than in other organs, likely because the localized shim box was placed over the liver. Therefore, frequency variations in more distant organs, such as in the left kidney and the spleen, were not as affected. Nevertheless, all organs were shifted closer to a 0 Hz median. For instance, the spleen had a median of -83.5 Hz which was corrected to 9.1 Hz. This was a critical improvement as otherwise voxels in these organs would have less than 50% of the expected RF power resulting in lower flip angles and would have experienced EPI chemical shift artifacts.

In addition to using a fast acquisition scheme and careful shimming to mitigate motion effects, patch-based denoising was used to greatly increase the quality of acquired metabolite images⁴². More voxels of metabolite signals within the whole abdomen passed the empirical SNR thresholds after denoising. As observed in one subject, the mean SNR of voxels within the whole abdomen were above

the SNR thresholds for a longer duration after denoising, demonstrating an improvement of HP ^{13}C dynamics against the background noise.

The liver trended towards a longer time-to-peak, which was compounded upon a longer decay time, resulting in an overall broadened dynamic curve. The kidneys, pancreas, and spleen exhibited steeper drop-offs after reaching peak pyruvate signal. Thus, even though the spleen had a comparable decay time to the liver, the liver's pyruvate uptake and dynamics remained distinct. This is perhaps reflective of the organ's unique dual blood-supply, where the portal venous phase (75-80% of the blood entering the liver) occurs approximately 8 seconds after the hepatic arterial phase^{46,47}.

Summed metabolite maps showed absolute metabolite signals from the kidneys and spleen that were 3-7 times higher than those from liver and pancreas, likely reflecting differences in perfusion and/or blood volume. However, smaller variance in pyruvate and lactate signals indicated more uniform distributions in the liver.

Although absolute metabolite signals were lower in the liver, k_{PL} and k_{PA} were both higher in the liver than in other abdominal organs, indicating higher relative production of these metabolites. Heterogeneity in the k_{PL} and k_{PA} maps of the liver was observed. In one subject, areas of low signal conformed to non-metabolically active regions such as the falciform ligament and the portal vein. In addition, heterogeneity may be caused by residual effects of transmit field non-uniformities as well as partial volume effects, for example due to the kidneys in nearby slices. These can be addressed in future work. Right and left kidney metabolism were symmetric as expected. The pancreas showed higher levels of alanine production relative to other organs, possibly due to high levels of protein synthesis related to its digestive enzyme and endocrine hormone functions.

6.5.1 Limitations

This study took place at a single center, using a single scanner of a single field strength from a single vendor. Additionally, there was a small number of subjects in this study. There was no available external reference for the measured pyruvate-to-lactate and pyruvate-to-alanine conversion rates. All of the subjects examined in this study were healthy volunteers. Although the RF coil used in this work was designed to have relatively uniform transmit and receive sensitivity over the entire imaging volume, residual variations due to non-uniformities in the transmit field and surface coil sensitivity profiles were present. In future studies, the effects of transmit field non-uniformities can be corrected through post-injection B_1^+ measurements or the future development and use of a built-in ^{13}C full-volume body coil³¹. Another limitation of this study was that it relied on a kinetic model that did not explicitly incorporate the effects of non-uniform excitation profiles. This has been shown to potentially cause overestimation of lactate exchange, particularly when large flip angles are used⁴⁸. This can also be explored in future work. As this was a technical development study, some minor variations in scan protocol were tested between different subjects. These variations mainly related to the degree of localized shimming that was performed as well as whether subjects received the EPSI acquisition, EPI acquisition, or both. None of the variations that were tested were expected to affect the overall conclusions drawn from the results.

6.6 Conclusions

In this study, a novel approach was developed and applied for acquiring HP ^{13}C metabolic images of multiple organs, that utilized a multi-echo gradient echo ^1H acquisition to inform ^{13}C center frequencies and to overcome challenges of broad spatial coverage as well as B_0 inhomogeneities. This enabled metabolically characterizing the healthy liver, kidneys, pancreas, and spleen. This normative data will be valuable in further investigations of cancer as well as metabolic liver diseases.

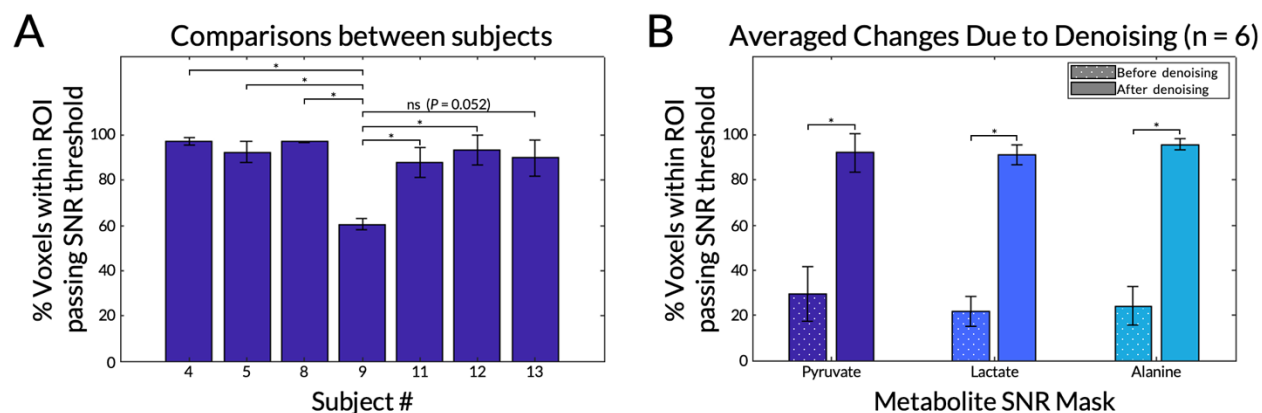
6.7 Acknowledgements

We would like to acknowledge the assistance of Jim Slater, Andrew Riselli, Evelyn Escobar, Mary Frost, Kimberly Okamoto, Jonathan Lin, James Lo, Sammy Gutierrez, and Kevin Sung.

6.8 Supporting Information

Supporting Information Table S6.1. Summary of all hyperpolarized ^{13}C acquisitions in healthy volunteers.

Subject # (sex; age)	HP ^{13}C imaging sequences	Successful data acquisition?	Considered in final analysis?
1 (M; 44)	Spiral gradient echo	Yes	No – incomparable pulse sequence
2 (M; 58)	EPSI	Yes	Yes
	Spiral gradient echo	Yes	No – incomparable pulse sequence
3 (M; 26)	EPSI	No – coil error (amplifier excessive power)	No
	EPSI	Yes	No – switched to a surface coil; incomparable coil set-up
4 (F; 34)	EPSI	Yes	Yes
	EPI	Yes	Yes
5 (M; 64)	EPI	Yes	Yes
6 (M; 60)	EPSI	No – coil cable was disconnected	No
	EPI	No – coil cable was disconnected	No
7 (M; 49)	EPSI	Yes	Yes
	EPI	No – dissolution fluid path failure	No
8 (F; 26)	EPSI	Yes	Yes
	EPI	Yes	Yes
9 (F; 33)	EPSI	No – IV injection line was closed	No
	EPI	Yes	Yes
10 (F; 21)	EPSI	Yes	Yes
	EPI	No – insufficient dissolution volume	No
11 (M; 36)	EPI	Yes	Yes
	EPI	No – dissolution fluid path failure	No
12 (F; 36)	EPI	Yes	Yes
13 (M; 33)	EPI	Yes	Yes



Supporting Information Figure S6.1. (A) Percentages of abdominal voxels passing the SNR threshold following denoising for each of the seven subjects with EPI scans. The post-denoising percentages for each metabolite (pyruvate, lactate, and alanine) of each subject were averaged. One-sample Kolmogorov-Smirnov tests accepted the null hypothesis that the values for each subject came from a normal distribution (all $P \geq 0.69$). Differences between the subjects were then compared using Tukey's multiple comparisons test. All significant comparisons are shown; all other comparisons were not significant. Significance levels are indicated by asterisks, with * meaning $P \leq 0.05$, ** meaning $P \leq 0.01$, and "ns" meaning $P > 0.05$. **(B)** The percent of voxels which passed the SNR thresholds for each metabolite before and after denoising excluding data points from subject #9. Presentation of data from all the subjects is given in **Figure 4C**. One-sample Kolmogorov-Smirnov tests accepted the null hypothesis that the values from the six scans came from a normal distribution (all $P \geq 0.29$). Differences before and after denoising were evaluated using paired t -tests. Significance levels are indicated by asterisks, with **** meaning $P \leq 0.0001$. Unlabeled comparisons were not statistically significant.

6.9 References

1. Kurhanewicz J, Vigneron DB, Ardenkjaer-Larsen JH, et al. Hyperpolarized ¹³C MRI: Path to Clinical Translation in Oncology. *Neoplasia (United States)*. 2019;21(1):1-16. doi:10.1016/j.neo.2018.09.006
2. Aggarwal R, Vigneron DB, Kurhanewicz J. Hyperpolarized 1-[¹³C]-Pyruvate Magnetic Resonance Imaging Detects an Early Metabolic Response to Androgen Ablation Therapy in Prostate Cancer. *Eur Urol*. 2017;72(6):1028-1029. doi:10.1016/j.eururo.2017.07.022
3. Granlund KL, Tee SS, Vargas HA, et al. Hyperpolarized MRI of Human Prostate Cancer Reveals Increased Lactate with Tumor Grade Driven by Monocarboxylate Transporter 1. *Cell Metab*. 2020;31(1):105-114. doi:10.1016/j.cmet.2019.08.024
4. Chen HY, Aggarwal R, Bok RA, et al. Hyperpolarized ¹³C-pyruvate MRI detects real-time metabolic flux in prostate cancer metastases to bone and liver: a clinical feasibility study. *Prostate Cancer Prostatic Dis*. 2020;23(2):269-276. doi:10.1038/s41391-019-0180-z
5. Park I, Larson PEZ, Gordon JW, et al. Development of methods and feasibility of using hyperpolarized carbon-13 imaging data for evaluating brain metabolism in patient studies. *Magn Reson Med*. 2018;80(3):864-873. doi:10.1002/mrm.27077
6. Miloushev VZ, Granlund KL, Boltvanskiy R, et al. Metabolic imaging of the human brain with hyperpolarized ¹³C Pyruvate demonstrates ¹³C lactate production in brain tumor patients. *Cancer Res*. 2018;78(14):3755-3760. doi:10.1158/0008-5472.CAN-18-0221
7. Autry AW, Gordon JW, Carvajal L, et al. Comparison between 8- and 32-channel phased-array receive coils for in vivo hyperpolarized ¹³C imaging of the human brain. *Magn Reson Med*. 2019;82(2):833-841. doi:10.1002/mrm.27743
8. Cunningham CH, Lau JYC, Chen AP, et al. Hyperpolarized ¹³C Metabolic MRI of the Human Heart: Initial Experience. *Circ Res*. 2016;119(11):1177-1182.

- doi:10.1161/CIRCRESAHA.116.309769
9. Rider OJ, Apps A, Miller JJJJ, et al. Noninvasive In Vivo Assessment of Cardiac Metabolism in the Healthy and Diabetic Human Heart Using Hyperpolarized ^{13}C MRI. *Circ Res.* 2020;126(6):725-736. doi:10.1161/CIRCRESAHA.119.316260
 10. Mammoli D, Carvajal L, Slater JB, et al. Kinetic Modeling of Hyperpolarized Carbon-13 Pyruvate Metabolism in the Human Brain. *IEEE Trans Med Imaging.* 2020;39(2):320-327. doi:10.1109/TMI.2019.2926437
 11. Abeyakoon O, Latifoltojar A, Gong F, et al. Hyperpolarised ^{13}C MRI: a new horizon for non-invasive diagnosis of aggressive breast cancer. *BJR Case Rep.* 2019;5(3):20190026. doi:10.1259/bjrcr.20190026
 12. Gallagher FA, Woitek R, McLean MA, et al. Imaging breast cancer using hyperpolarized carbon-13 MRI. *Proc Natl Acad Sci U S A.* 2020;117(4):2092-2098. doi:10.1073/pnas.1913841117
 13. Ardenkjær-Larsen JH, Golman K, Gram A, et al. Increase of signal-to-noise of more than 10,000 times in liquid state NMR. *Discov Med.* 2003;100(18):10158-10163.
 14. Warburg O. On the origin of cancer cells. *Science (80-).* 1956;123(3191):309-314. doi:10.1126/science.123.3191.309
 15. Hu S, Balakrishnan A, Bok RA, et al. ^{13}C -pyruvate imaging reveals alterations in glycolysis that precede c-Myc-induced tumor formation and regression. *Cell Metab.* 2011;14(1):131-142. doi:10.1016/j.cmet.2011.04.012
 16. Keshari KR, Sriram R, Van Crieking M, et al. Metabolic reprogramming and validation of hyperpolarized ^{13}C lactate as a prostate cancer biomarker using a human prostate tissue slice culture bioreactor. *Prostate.* 2013;73(11):1171-1181. doi:10.1002/pros.22665
 17. Larson PEZ, Chen HY, Gordon JW, et al. Investigation of analysis methods for

- hyperpolarized ¹³C-pyruvate metabolic MRI in prostate cancer patients. *NMR Biomed.* 2018;31(11):e3997. doi:10.1002/nbm.3997
18. Crane JC, Gordon JW, Chen HY, et al. Hyperpolarized ¹³C MRI data acquisition and analysis in prostate and brain at University of California, San Francisco. *NMR Biomed.* 2021;34(5):e4280. doi:10.1002/nbm.4280
 19. Wang ZJ, Ohliger MA, Larson PEZ, et al. Hyperpolarized ¹³C MRI: State of the art and future directions. *Radiology.* 2019;291(2):273-284. doi:10.1148/radiol.2019182391
 20. Day SE, Kettunen MI, Gallagher FA, et al. Detecting tumor response to treatment using hyperpolarized ¹³C magnetic resonance imaging and spectroscopy. *Nat Med.* 2007;13(11):1382-1387. doi:10.1038/nm1650
 21. Chaumeil MM, Ozawa T, Park IW, et al. Hyperpolarized ¹³C MR spectroscopic imaging can be used to monitor Everolimus treatment in vivo in an orthotopic rodent model of glioblastoma. *Neuroimage.* 2012;59(1):193-201. doi:10.1016/j.neuroimage.2011.07.034
 22. Radoul M, Chaumeil MM, Eriksson P, Wang AS, Phillips JJ, Ronen SM. MR studies of glioblastoma models treated with dual PI3K/mTOR inhibitor and temozolomide: Metabolic changes are associated with enhanced survival. *Mol Cancer Ther.* 2016;15(5):1113-1122. doi:10.1158/1535-7163.MCT-15-0769
 23. Hesketh RL, Wang J, Wright AJ, et al. Magnetic resonance imaging is more sensitive than PET for detecting treatment-induced cell death-dependent changes in glycolysis. *Cancer Res.* 2019;79(14):3557-3569. doi:10.1158/0008-5472.CAN-19-0182
 24. Tran M, Latifoltojar A, Neves JB, et al. First-in-human in vivo non-invasive assessment of intra-tumoral metabolic heterogeneity in renal cell carcinoma. *BJR | case reports.* 2019;5(3):20190003. doi:10.1259/bjrcr.20190003
 25. Tang S, Meng M V., Slater JB, et al. Metabolic imaging with hyperpolarized ¹³C pyruvate

- magnetic resonance imaging in patients with renal tumors—Initial experience. *Cancer*. 2021;127(15):2693-2704. doi:10.1002/cncr.33554
26. Kwanten WJ, Martinet W, Francque SM. Autophagy in Non-Alcoholic Fatty Liver Disease (NAFLD). In: *Autophagy in Current Trends in Cellular Physiology and Pathology*. InTech; 2016:455-483. doi:10.5772/64534
 27. Moon CM, Oh CH, Ahn KY, et al. Metabolic biomarkers for non-alcoholic fatty liver disease induced by high-fat diet: In vivo magnetic resonance spectroscopy of hyperpolarized [1-13C] pyruvate. *Biochem Biophys Res Commun*. 2017;482(1):112-119. doi:10.1016/j.bbrc.2016.08.118
 28. Wilson DM, Di Gialleonardo V, Wang ZJ, et al. Hyperpolarized 13C spectroscopic evaluation of oxidative stress in a rodent model of steatohepatitis. *Sci Rep*. 2017;7(46014):1-7. doi:10.1038/srep46014
 29. Kjærgaard U, Laustsen C, Nørlinger T, et al. Hyperpolarized [1- 13 C] pyruvate as a possible diagnostic tool in liver disease. *Physiol Rep*. 2018;6(23):1-11. doi:10.14814/phy2.13943
 30. Morze C Von, Allu PKR, Chang GY, et al. Non-invasive detection of divergent metabolic signals in insulin deficiency vs. insulin resistance in vivo. *Sci Rep*. 2018;8(1):1-12. doi:10.1038/s41598-018-20264-w
 31. Tang S, Milshteyn E, Reed G, et al. A regional bolus tracking and real-time B1 calibration method for hyperpolarized 13C MRI. *Magn Reson Med*. 2019;81(2):839-851. doi:10.1002/mrm.27391
 32. Lau AZ, Chen AP, Hurd RE, Cunningham CH. Spectral-spatial excitation for rapid imaging of DNP compounds. *NMR Biomed*. 2011;24(8):988-996. doi:10.1002/nbm.1743
 33. Schulte RF, Sacolick L, Deppe MH, et al. Transmit gain calibration for nonproton MR using the Bloch-Siegert shift. *NMR Biomed*. 2011;24(9):1068-1072. doi:10.1002/nbm.1657
 34. Lau AZ, Chen AP, Cunningham CH. Integrated Bloch-Siegert B1 mapping and multislice

- imaging of hyperpolarized ^{13}C pyruvate and bicarbonate in the heart. *Magn Reson Med.* 2012;67(1):62-71. doi:10.1002/mrm.22977
35. Sacolick LI, Wiesinger F, Hancu I, Vogel MW. B1 mapping by Bloch-Siegert shift. *Magn Reson Med.* 2010;63(5):1315-1322. doi:10.1002/mrm.22357
 36. Grist JT, Hansen ESS, Sánchez-Heredia JD, et al. Creating a clinical platform for carbon-13 studies using the sodium-23 and proton resonances. *Magn Reson Med.* 2020;84(4):1817-1827. doi:10.1002/mrm.28238
 37. Nelson SJ, Kurhanewicz J, Vigneron DB, et al. Metabolic Imaging of Patients with Prostate Cancer Using Hyperpolarized [1- ^{13}C]Pyruvate. *Sci Transl Med.* 2013;5(198):198ra108. doi:10.1126/scitranslmed.3006070
 38. Chen HY, Larson PEZ, Gordon JW, et al. Technique development of 3D dynamic CS-EPSI for hyperpolarized ^{13}C pyruvate MR molecular imaging of human prostate cancer. *Magn Reson Med.* 2018;80(5):2062-2072. doi:10.1002/mrm.27179
 39. Lee PM, Chen HY, Gordon JW, et al. Specialized computational methods for denoising, B1 correction, and kinetic modeling in hyperpolarized ^{13}C MR EPSI studies of liver tumors. *Magn Reson Med.* 2021;86(5):2402-2411. doi:10.1002/mrm.28901
 40. Gordon JW, Chen HY, Autry A, et al. Translation of Carbon-13 EPI for hyperpolarized MR molecular imaging of prostate and brain cancer patients. *Magn Reson Med.* 2019;81(4):2702-2709. doi:10.1002/mrm.27549
 41. Zhu Z, Zhu X, Ohliger MA, et al. Coil combination methods for multi-channel hyperpolarized ^{13}C imaging data from human studies. *J Magn Reson.* 2019;301:73-79. doi:10.1016/j.jmr.2019.01.015
 42. Kim Y, Chen H, Autry AW, et al. Denoising of hyperpolarized ^{13}C MR images of the human brain using patch-based higher-order singular value decomposition. *Magn Reson Med.*

- 2021;86(5):2497-2511. doi:10.1002/mrm.28887
43. Yushkevich PA, Piven J, Hazlett HC, et al. User-guided 3D active contour segmentation of anatomical structures: Significantly improved efficiency and reliability. *Neuroimage*. 2006;31(3):1116-1128. doi:10.1016/j.neuroimage.2006.01.015
 44. Gordon JW, Larson PEZ. Pulse sequences for hyperpolarized MRS. *eMagRes*. 2016;5(2):1229-1246. doi:10.1002/9780470034590.emrstm1451
 45. Singerman R., Denison T., Wen H, Balaban R. Simulation of B1 Field Distribution and Intrinsic Signal-to-Noise in Cardiac MRI as a Function of Static Magnetic Field. *J Magn Reson*. 1997;125(1):72-83. doi:10.1006/jmre.1996.1073
 46. Rocha FG. Liver blood flow. In: Jarnagin W, Blumgart L, eds. *Blumgart's Surgery of the Liver, Pancreas and Biliary Tract*. Fifth Edit. Elsevier; 2012:74-86. doi:10.1016/B978-1-4377-1454-8.00004-7
 47. Bader T, Prokesch R, Grabenwöger F. Timing of the Hepatic Arterial Phase During Contrast-Enhanced Computed Tomography of the Liver. *Invest Radiol*. 2000;35(8):486-492. doi:10.1097/00004424-200008000-00005
 48. Walker CM, Gordon JW, Xu Z, et al. Slice profile effects on quantitative analysis of hyperpolarized pyruvate. *NMR Biomed*. 2020;33(10):1-13. doi:10.1002/nbm.4373

Publishing Agreement

It is the policy of the University to encourage open access and broad distribution of all theses, dissertations, and manuscripts. The Graduate Division will facilitate the distribution of UCSF theses, dissertations, and manuscripts to the UCSF Library for open access and distribution. UCSF will make such theses, dissertations, and manuscripts accessible to the public and will take reasonable steps to preserve these works in perpetuity.

I hereby grant the non-exclusive, perpetual right to The Regents of the University of California to reproduce, publicly display, distribute, preserve, and publish copies of my thesis, dissertation, or manuscript in any form or media, now existing or later derived, including access online for teaching, research, and public service purposes.

DocuSigned by:

Philip Lee

27AC9FDE2AD44B4...

Author Signature

5/26/2022

Date